

Volume 7, Issue 1, 2025

Print ISSN: 2663-1954

Online ISSN: 2663-1962

JOURNAL OF PHARMACEUTICAL AND MEDICAL RESEARCH



Copyright© Upubscience Publisher

Journal of Pharmaceutical and Medical Research

Volume 7, Issue 1, 2025



Published by Upubscience Publisher

Copyright© The Authors

Upubscience Publisher adheres to the principles of Creative Commons, meaning that we do not claim copyright of the work we publish. We only ask people using one of our publications to respect the integrity of the work and to refer to the original location, title and author(s).

Copyright on any article is retained by the author(s) under the Creative Commons Attribution license, which permits unrestricted use, distribution, and reproduction in any medium, provided the original work is properly cited.

Authors grant us a license to publish the article and identify us as the original publisher.

Authors also grant any third party the right to use, distribute and reproduce the article in any medium, provided the original work is properly cited.

Journal of Pharmaceutical and Medical Research

Print ISSN: 2663-1954 Online ISSN: 2663-1962

Email: info@upubscience.com

Website: <http://www.upubscience.com/>

Table of Content

CLINICAL STUDY ON THE TREATMENT OF CHRONIC OBSTRUCTIVE PULMONARY DISEASE WITH DAMP-TOXIN OBSTRUCTING LUNG SYNDROME USING XUANFEI BAIDU GRANULES COMBINED WITH WESTERN MEDICINE	1-10
Qian Liu, FeiXiong Yan, XiaFan Qu, Qiao Zhu, Ping He, BinBin Chen*	
APPLICATION AND PROGRESS OF CT ANGIOGRAPHY – X-RAY IMAGE FUSION TECHNOLOGY IN ENDOVASCULAR SURGERY: A LITERATURE REVIEW	11-16
YiRen Lai	
THE RELATIONSHIP BETWEEN GENE MUTATIONS AND PROGNOSIS IN PATIENTS WITH STAGE I NON-SMALL CELL LUNG CANCER AFTER SURGERY	17-21
Rui Ouyang, Ming Du*	
THE PATHOLOGICAL PATHWAY FOR THE PERSISTENCE OF AD SYMPTOMS AFTER THE REMOVAL OF AMYLOID PLAQUES	22-27
JingHao Wang	
ACUPUNCTURE TREATMENT FOR SPINAL CORD INJURY: A RESEARCH BASED ON BIBLIOMETRICS AND DATA MINING	28-42
EnYan Xue, JiQing Wang, JingDong Gu, ShangJun Xia, Shuai Luo, Zheng Huang*	
TRANSMISSION MODEL OF INFLUENZA A WITH ASYMPTOMATIC INFECTION AND ENVIRONMENTAL TRANSMISSION	43-50
WenXuan Li	
ANALYSIS OF THE EFFICACY OF TRANSUMBILICAL SINGLE-SITE LAPAROSCOPIC TOTAL EXTRAPERITONEAL TESTICULAR DESCENT FIXATION IN THE TREATMENT OF INGUINAL CRYPTORCHIDISM IN CHILDREN	51-56
ZhiFeng Mo, Fei Yu, BaiYu Zhu, MaoLin Liu, HanZhong He*	
CIGARETTE SMOKE EXTRACT PROMOTES APOPTOSIS OF HUMAN PULMONARY ARTERIAL ENDOTHELIAL CELLS VIA THE ER STRESS CHOP SIGNALING PATHWAY	57-64
Mo Liang, LiLe Wang, Mo Xiao, Bo Chen, Jie Li, RuiCheng Hu*	
COMMON SOIL-BORNE PATHOGENIC DISEASES IN AMERICAN GINSENG (PANAX QUINQUEFOLIUS) CULTIVATION AND INTEGRATED CONTROL APPROACHES	65-70
Dan Luo, XianEn Li*	
ANALYSIS OF THE EFFECT OF ARTIFICIAL INTELLIGENCE-ASSISTED MINIMALLY INVASIVE TREATMENT FOR URINARY CALCULI	71-77
LinFeng Li	

CLINICAL STUDY ON THE TREATMENT OF CHRONIC OBSTRUCTIVE PULMONARY DISEASE WITH DAMP-TOXIN OBSTRUCTING LUNG SYNDROME USING XUANFEI BAIDU GRANULES COMBINED WITH WESTERN MEDICINE

Qian Liu¹, FeiXiong Yan¹, XiaFan Qu¹, Qiao Zhu¹, Ping He¹, BinBin Chen^{2*}

¹Hunan Institute of Schistosomiasis, The Third People's Hospital of Hunan Province, Yueyang, Hunan, China.

²Hunan Provincial People's Hospital/The first affiliated hospital of Hunan Normal University, Changsha, Hunan, China.

Qian Liu and Feixiong Yan contributed equally to this work, they are both first authors.

Corresponding author: BinBin Chen, E-mail: 11135009@qq.com

Abstract: Objective: To study the clinical efficacy of Xuanfei Baidu Granules combined with Western medicine in the treatment of Damp-Toxin Obstructing Lung Chronic Obstructive Pulmonary Disease (COPD).

Methods: A retrospective analysis was conducted on the data of 124 COPD patients treated at our hospital's respiratory department between July 2021 and March 2024. All patients were diagnosed with Damp-Toxin Obstructing Lung Syndrome. Of these, 64 patients treated with Western medicine alone were designated as the control group, while 60 patients treated with Xuanfei Baidu Granules combined with Western medicine were designated as the study group. The study compared Traditional Chinese Medicine (TCM) syndrome scores, lung function [Forced Expiratory Volume in 1 second (FEV1), Forced Vital Capacity (FVC), FEV1/FVC ratio, Airway Resistance (Raw), Peak Expiratory Flow Rate (PEFR)], 6-minute walk test (6MWT) results, COPD Assessment Test (CAT) scores, inflammation-related indicators [White Blood Cell count (WBC), Neutrophil percentage (NEUT%), Lymphocyte percentage (LYMPH%), Platelet count (PLT), Interleukin-6 (IL-6), Interleukin-17 (IL-17), C-reactive protein (CRP), Procalcitonin (PCT), Connective Tissue Growth Factor (CTGF), Transforming Growth Factor- β 1 (TGF- β 1)], blood gas analysis indicators [Arterial Oxygen Partial Pressure (PaO₂), Carbon Dioxide Partial Pressure (PaCO₂), Oxygen Saturation (SaO₂), Oxygenation Index (PaO₂/FiO₂)], clinical efficacy, and adverse reactions between the two groups.

Results: After 5 days of treatment, the control group exhibited significantly higher scores for fever, cough with sputum, dyspnea, wheezing, abdominal distension, constipation, difficulty falling asleep, fatigue, poor appetite, and total TCM syndrome scores compared to the study group, with differences being statistically significant ($P < 0.05$). Lung function parameters, including FEV1, FVC, FEV1/FVC ratio, PEFR, and 6MWT results, were significantly lower in the control group compared to the study group, while Raw and COPD CAT scores were significantly higher in the control group. These differences were statistically significant ($P < 0.01$). There was no statistically significant difference in WBC counts between the two groups after 5 days of treatment ($P > 0.05$). However, NEUT%, LYMPH%, IL-6, IL-17, CRP, PCT, CTGF, and TGF- β 1 levels were significantly higher in the control group, while PLT was significantly lower compared to the study group, with differences being statistically significant ($P < 0.001$). PaO₂, PaCO₂, SaO₂, and PaO₂/FiO₂ were all significantly lower in the control group compared to the study group ($P < 0.001$). The total effective rate in the control group was 81.25% (52/64), significantly lower than 95.00% (57/60) in the study group, with the difference being statistically significant ($P < 0.05$). The adverse reaction rate was 10.94% (7/64) in the control group compared to 6.67% (4/60) in the study group, with no statistically significant difference ($P > 0.05$).

Conclusion: The combination of Xuanfei Baidu Granules with Western medicine significantly improves heart and lung function, reduces TCM syndrome scores and inflammation levels, and enhances blood oxygen content and clinical efficacy in patients with damp-heat obstructing the lung type of COPD.

Keywords: Xuanfei Baidu Granules; Damp-heat obstructing the lung syndrome; COPD; Cardio-pulmonary function; Traditional Chinese medicine syndrome scores

1 INTRODUCTION

Chronic obstructive pulmonary disease (COPD) is a group of chronic respiratory diseases characterized by persistent airflow limitation, inflammatory responses, and airway hyperreactivity, often accompanied by cough, dyspnea, wheezing, and fever [1]. The primary pathophysiological changes in COPD are ventilation limitation and airway obstruction. Over time, this can lead to complications such as rupture of pulmonary bullae into the pleural cavity, causing spontaneous pneumothorax, or respiratory failure, sleep apnea, and cor pulmonale [2]. Clinical treatment of COPD mainly involves anticholinergic bronchodilators, corticosteroid combination formulations, and long-acting or short-acting β 2-agonists. These treatments aim to inhibit airway smooth muscle contraction and bronchospasm, improving pulmonary ventilation and gas exchange [3]. However, numerous studies [4-5] have pointed out that such medications, including salbutamol, dexamethasone, and prednisone, may increase the risk of respiratory infections, immune system complications, and even lead to heart failure, myocardial infarction, and arrhythmias over prolonged

use. Additionally, the progression of COPD is influenced by environmental, genetic, and age factors. Thus, reducing the safety risks associated with long-term and regular medication while improving clinical symptoms and preventing acute exacerbations of COPD (AECOPD) remains a key focus in enhancing clinical efficacy. In traditional Chinese medicine (TCM), COPD is categorized under "lung obstruction" and "asthma syndrome," with patients often having a congenital deficiency or chronic lung deficiency. Lung deficiency leads to Qi deficiency, which impairs blood circulation and fluid distribution, causing phlegm accumulation and damp-heat stagnation. This results in blocked blood vessels and stagnant Qi, coupled with a lack of Qi to consolidate the exterior, allowing pathogens to invade and damage fluids, leading to upper respiratory infections and recurrent cough, wheezing, and chest tightness [6]. Therefore, TCM treatment for COPD should focus on "dispersing the lung," "eliminating dampness and heat," and "detoxifying the lung." This study analyzes the efficacy of Xuanfei Baidu Granules combined with Western medicine in treating damp-heat obstructing lung COPD, providing scientific evidence for optimizing combined TCM and Western treatment approaches for this condition.

2 MATERIALS AND METHODS

2.1 Clinical Data

A retrospective review was conducted on 124 COPD patients admitted to the Respiratory Medicine Department of our hospital from June 2023 to June 2024. All patients were diagnosed with the TCM pattern of damp-heat obstructing the lung. Among them, 64 patients receiving only Western medicine were designated as the control group, while 60 patients receiving Xuanfei Baidu Granules combined with Western medicine were designated as the study group. In the control group, there were 37 males and 27 females, aged 41 to 76 years, with an average age of 54.67 ± 7.11 years. The Body Mass Index (BMI) ranged from 19.5 to 32 kg/m², with an average BMI of 24.57 ± 2.32 kg/m². In the study group, there were 34 males and 26 females, aged 43 to 78 years, with an average age of 55.23 ± 6.82 years. The BMI ranged from 19.8 to 31.5 kg/m², with an average BMI of 24.31 ± 2.18 kg/m². There were no statistically significant differences in baseline characteristics between the two groups ($P > 0.05$), indicating comparability.

2.1.1 Western medicine diagnostic criteria[7]

The presence of various symptoms such as wheezing, shortness of breath, cough, sputum production, and chest tightness to varying degrees. Imaging studies, such as lung function tests, chest CT, or X-ray, show findings including increased anteroposterior diameter of the thoracic cavity, sparse peripheral vascular markings in the lung fields, formation of bullae, changes in small airways, and emphysema. Laboratory tests reveal increased white blood cell count (WBC), elevated levels of inflammatory markers or cytokines such as C-reactive protein (CRP) and Interleukin-6 (IL-6). Lung function tests and the COPD self-assessment test (CAT) demonstrate varying degrees of lung function deterioration.

2.1.2 Traditional Chinese medicine diagnostic criteria[8-9]

Diagnosis of "Damp-Heat Obstructing the Lung Syndrome" is based on the presence of 2 primary symptoms and 1 secondary symptom or 1 primary symptom and 2 secondary symptoms, along with specific tongue and pulse signs. Primary Symptoms: Fever, cough with sputum, chest tightness and shortness of breath, wheezing, etc. Secondary Symptoms: Abdominal bloating, constipation, difficulty falling asleep, fatigue, poor appetite, etc. Tongue Signs: Dark red tongue body, yellow and greasy coating, or dry tongue; pulse signs include slippery or rapid pulse or wiry and slippery pulse.

2.1.3 Inclusion criteria

Patients aged 18-80 years old, non-lactating, and non-pregnant women, all of whom signed informed consent forms and received approval from the hospital's ethics committee. No history of nasal, oral, throat, or lung surgery, nor any space-occupying lesions. Patients who meet both the Western medical diagnostic criteria for COPD and the Traditional Chinese Medicine criteria for Damp-Heat Obstructing the Lung Syndrome. No history of systemic glucocorticoid use or antibiotic overuse.

2.1.4 Exclusion criteria

Patients unable to expectorate or those with a large amount of airway secretions requiring intubation. Presence of severe hepatic or renal dysfunction, congenital immune diseases, cardiovascular or cerebrovascular diseases not caused by COPD, active pulmonary tuberculosis, or malignancies. Coexisting with other Traditional Chinese Medicine (TCM) syndromes, laryngeal edema, tracheal polyps, or other conditions affecting ventilation function. Active bleeding tendencies, severe mental disorders, infectious diseases, or consciousness/communication impairments. Patients allergic to the study drugs or their excipients, or those with incomplete clinical and follow-up data.

2.2 Methods

Control Group Treatment: Patients were advised to reduce exposure to risk factors by quitting smoking and alcohol, avoiding dust, irritant gases, and harmful substances, and engaging in moderate exercise. They received back percussion to promote expectoration or nebulized hypertonic saline for sputum clearance. In cases of dyspnea and chest tightness, a semi-recumbent position was recommended. During stable COPD periods, patients received low-flow oxygen therapy at 1-2 L/min. During acute exacerbations of COPD (AECOPD), high-flow humidified oxygen therapy at 6-8 L/min was provided, and non-invasive mechanical ventilation was administered for AECOPD with respiratory failure. For anti-inflammatory and anti-allergic treatment, patients were given budesonide suspension (AstraZeneca Pty Ltd,

approval number H20040624, 2 mg/vial), with a dose of 2 mg per session, twice a day. For severe wheezing and dyspnea, fluticasone propionate nasal spray (Glaxo Wellcome, S.A., approval number H20070265, 50 mcg per spray) was used once daily, with 2 sprays per nostril; if symptoms persisted, the dose was increased to twice daily, with no more than 4 sprays per nostril. Cefoperazone sodium and sulbactam (manufactured by Shanxi Zhendong Taisheng Pharmaceutical Co., Ltd., approval number H20044344, 4 g/tablet) was administered to control respiratory infections, with a dose of 4 g per session, once daily.

Research Group Treatment: In addition to the treatments provided to the control group, the research group received Xuanfei Baidu Granules (manufactured by Shandong Buchang Pharmaceuticals Co., Ltd., approval number C20210003, 10g*2 bags/box), with a dosage of 1 bag per session, twice a day. Both groups were treated continuously for 5 days, with the medication regimen adjusted based on individual conditions. Other bronchodilators or expectorants such as ipratropium bromide, salbutamol, or ambroxol hydrochloride were combined as needed. Adverse reactions in both groups were carefully documented.

2.3 Observational Indicators

2.3.1 TCM syndrome score

A self-made questionnaire was used to evaluate patients' Traditional Chinese Medicine (TCM) syndrome scores before and after 5 days of treatment. The four main symptoms—fever, cough with phlegm, chest tightness with shortness of breath, and wheezing—were scored on a scale of 0 to 6. The five secondary symptoms—abdominal distension, constipation, difficulty sleeping, fatigue, and poor appetite—were scored on a scale of 0 to 3. The higher the total score, the more severe the "damp toxin obstructing the lung" syndrome.

2.3.2 Lung function

Lung function was assessed using several parameters, including Forced Expiratory Volume in 1 Second (FEV₁), Forced Vital Capacity (FVC), Airway Resistance (Raw), and Peak Expiratory Flow Rate (PEFR). These measurements were taken using the BK-LFT-I lung function detector (manufactured by Shandong Keboboyue Technology Co., Ltd., registration number Lu Yao Jian Xie Zhun 20180058). The FEV₁/FVC ratio was also calculated.

2.3.3 6-Minute Walk Test (6MWT)

The 6MWT was conducted by having patients walk back and forth along a 30-meter corridor at their fastest possible pace. The distance covered in six minutes was used to evaluate cardiopulmonary function. If the patient experienced severe symptoms such as dizziness, chest tightness, or shortness of breath during the test, it was immediately terminated. A shorter walking distance within the six-minute period indicates more severe cardiopulmonary function impairment.

2.3.4 COPD CAT score

Patients were asked to complete the COPD Assessment Test (CAT) after fully understanding the items and their meanings. The assessment covered eight aspects: cough, sputum production, chest tightness, exercise tolerance, daily life activities, outdoor activities, sleep, and energy levels. Each aspect was rated on a scale from 0 to 5, with 0 indicating no impact and 5 indicating a severe impact. The total score ranges as follows:

0–10 points: Indicates that the patient's life is largely normal, but shortness of breath and discomfort may occur during intense activities.

11–20 points: Suggests that COPD has become one of the patient's health issues, with frequent symptoms like coughing, sputum production, and shortness of breath.

21–30 points: Indicates that COPD significantly impacts the patient's life, limiting most activities and causing fear and panic.

30 points: Suggests that COPD has a very severe impact on the patient's life, preventing any activity and making self-care difficult.

2.3.5 Inflammation-related indicators

Inflammation-related indicators were measured using the HwCyte-1026M flow cytometer (Zhejiang Pantide Biotechnology Co., Ltd., Registration No. ZJX20212220112), including white blood cell count (WBC), neutrophil percentage (NEUT%), lymphocyte percentage (LYMPH%), and platelet count (PLT). Additionally, 10ml of venous blood was drawn from patients and centrifuged at 3000r/min for 10 minutes (centrifugal radius of 10cm) to obtain the supernatant. Interleukin-6 (IL-6) and Interleukin-17 (IL-17) levels were detected using the enzyme-linked immunosorbent assay (ELISA) method, while C-reactive protein (CRP) levels were also measured using ELISA. Procalcitonin (PCT), Connective tissue growth factor (CTGF), and Transforming growth factor- β 1 (TGF- β 1) were detected using immunochromatography. The results were standardized using the URIT-5160 automatic blood cell analyzer (Shanghai Qisheng Medical Instrument Co., Ltd., Registration No. GXZ20162220087).

2.3.6 Arterial blood gas analysis

Arterial blood gas analysis was performed by drawing 5ml of fasting arterial blood from patients and analyzing it with the Kangli blood gas and electrolyte analyzer BG-800A (Wuhan Yijie Xun'an Trading Co., Ltd., Registration No. YX20162220822). The analysis included measurements of arterial partial pressure of oxygen (PaO₂), arterial partial pressure of carbon dioxide (PaCO₂), and blood oxygen saturation (SaO₂). The oxygenation index (PaO₂/FiO₂) was also calculated, where FiO₂ represents the fraction of inspired oxygen.

2.3.7 Clinical efficacy

Clinical Control: Symptoms such as cough and expectoration have mostly disappeared, with a reduction of $\geq 95\%$ in TCM syndrome scores. **Significantly Effective:** Symptoms and signs have significantly improved, with a reduction of

70% to 94% in TCM syndrome scores. Effective: Symptoms and signs have shown some improvement, with a reduction of 30% to 69% in TCM syndrome scores. Ineffective: There is no improvement, or the symptoms and signs have worsened.

2.3.8 Adverse reactions

Such as dizziness, rash, gastrointestinal reactions, etc.

2.4 Statistical Analysis

Data were processed using SPSS version 27.0 statistical software. Categorical data were recorded as "n (%)" and analyzed using the chi-square test; ordinal data were analyzed using the rank-sum test. Continuous data were recorded as "mean \pm standard deviation" and analyzed using the t-test. A p-value of <0.05 was considered statistically significant.

3 RESULTS

3.1 Comparison of Traditional Chinese Medicine Syndrome Scores Between the Two Groups

After 5 days of treatment, the control group had significantly higher scores for fever, cough and sputum, breathlessness, wheezing, abdominal distension, constipation, difficulty falling asleep, fatigue, poor appetite, and overall Traditional Chinese Medicine (TCM) syndrome score compared to the study group. The differences were statistically significant ($P < 0.05$), as shown in Table 1.

Table 1 Comparison of TCM Syndrome Scores between the Two Groups ($\bar{x} \pm s$, points)

Item		Control group (n=64)	Research group (n=60)	t	P
Fever	pre-treatment	3.45 \pm 0.78	3.50 \pm 0.72	0.370	0.712
	5days-treatment	2.50 \pm 0.62*	1.87 \pm 0.50*	6.203	<0.001
Cough and sputum	pre-treatment	4.20 \pm 0.84	4.23 \pm 0.81	0.202	0.840
	5days-treatment	2.17 \pm 0.52*	1.57 \pm 0.59*	6.017	<0.001
Suffocated and breathless	pre-treatment	4.13 \pm 0.72	4.10 \pm 0.71	0.233	0.816
	5days-treatment	2.06 \pm 0.56*	1.62 \pm 0.64*	4.081	<0.001
gasp	pre-treatment	3.86 \pm 0.83	3.90 \pm 0.84	0.267	0.790
	5days-treatment	2.05 \pm 0.45*	1.63 \pm 0.64*	4.248	<0.001
Abdominal bloating	pre-treatment	1.72 \pm 0.74	1.73 \pm 0.63	0.107	0.915
	5days-treatment	0.81 \pm 0.56*	0.55 \pm 0.59*	2.508	0.014
constipation	pre-treatment	1.64 \pm 0.60	1.62 \pm 0.49	0.203	0.840
	5days-treatment	0.83 \pm 0.55*	0.47 \pm 0.50*	3.830	<0.001
Difficulty falling asleep	pre-treatment	1.84 \pm 0.51	1.85 \pm 0.58	0.102	0.919
	5days-treatment	0.78 \pm 0.42*	0.38 \pm 0.49*	4.890	<0.001
Lassitude and fatigue	pre-treatment	1.59 \pm 0.61	1.57 \pm 0.63	0.180	0.858
	5days-treatment	0.70 \pm 0.52*	0.28 \pm 0.45*	4.795	<0.001
Poor appetite	pre-treatment	1.73 \pm 0.60	1.77 \pm 0.50	0.402	0.689
	5days-treatment	0.78 \pm 0.52*	0.32 \pm 0.47*	5.156	<0.001
Total points	pre-treatment	24.17 \pm 2.13	24.27 \pm 1.64	0.292	0.771
	5days-treatment	12.69 \pm 1.42*	8.68 \pm 1.42*	15.701	<0.001

Note: Compared with before treatment, * $P < 0.05$.

3.2 Comparison of Pulmonary Function, 6-Minute Walk Test (6MWT), and COPD Assessment Test (CAT) Between the Two Groups

After 5 days of treatment, the control group had significantly lower levels of FEV1, FVC, FEV1/FVC, PEFR, and 6MWT compared to the study group, while Raw and COPD CAT scores were significantly higher in the control group compared to the study group, with all differences being statistically significant ($P < 0.01$), as shown in Table 2.

Table 2 Comparison of Pulmonary Function, 6-Minute Walk Test (6MWT), and COPD Assessment Test (CAT) Between the Two Groups ($\bar{x} \pm s$)

Item		Control group (n=64)	Research group (n=60)	<i>t</i>	<i>P</i>
FEV1 (L)	pre-treatment	1.09±0.29	1.13±0.31	0.742	0.459
	5days-treatment	1.56±0.28*	2.11±0.35*	9.692	<0.001
FVC (L)	pre-treatment	1.72±0.44	1.69±0.48	0.363	0.717
	5days-treatment	2.13±0.37*	2.62±0.40*	7.086	<0.001
FEV1/FVC(%)	pre-treatment	64.41±13.39	63.85±13.58	0.231	0.818
	5days-treatment	74.33±12.48*	80.92±9.57*	3.284	0.001
Raw (%)	pre-treatment	75.38±7.87	74.60±7.12	0.578	0.565
	5days-treatment	57.49±5.72*	52.16±4.58*	5.704	<0.001
PEFR (L/min)	pre-treatment	3.42±0.78	3.39±0.75	0.218	0.828
	5days-treatment	4.97±1.02*	5.68±1.34*	3.333	0.001
6MWT (m)	pre-treatment	178.45±21.71	176.83±22.05	0.412	0.681
	5days-treatment	267.56±35.83*	314.52±42.16*	6.697	<0.001
COPD CAT (score)	pre-treatment	18.27±4.25	17.68±4.57	0.745	0.458
	5days-treatment	12.14±2.74*	9.32±1.85*	6.672	<0.001

Note: Compared with before treatment, * $P < 0.05$.

3.3 Comparison of Inflammation-Related Indicators Between the Two Groups

There was no statistically significant difference in WBC levels between the two groups ($P > 0.05$); however, after 5 days of treatment, the control group had significantly higher levels of NEUT%, LYMPH%, IL-6, IL-17, CRP, PCT, CTGF, and TGF- β 1 compared to the study group, while PLT was significantly lower in the control group than in the study group, with all differences being statistically significant ($P < 0.001$), as shown in Table 3.

Table 3 Comparison of Inflammation-Related Indicators Between the Two Groups ($\bar{x} \pm s$)

Item		Control group(n=64)	Research group (n=60)	<i>t</i>	<i>P</i>
WBC ($\times 10^9/L$)	pre-treatment	10.35±1.26	10.29±1.24	0.267	0.790
	5days-treatment	8.20±1.05	8.13±1.02	0.376	0.708
NEUT%	pre-treatment	84.39±7.53	85.06±7.10	0.509	0.612

	5days-treatment	70.24±6.15*	64.50±4.72*	5.802	<0.001
LYMPH%	pre-treatment	47.21±5.57	46.89±5.29	0.328	0.744
	5days-treatment	38.30±4.29*	32.15±3.40*	8.809	<0.001
PLT (×10 ⁹ /L)	pre-treatment	74.22±9.85	73.36±10.27	0.476	0.635
	5days-treatment	130.54±15.46*	158.69±17.45*	9.521	<0.001
IL-6 (ng/L)	pre-treatment	45.36±7.48	46.57±7.16	0.919	0.360
	5days-treatment	27.21±5.43*	19.45±4.29*	8.792	<0.001
IL-17 (ng/L)	pre-treatment	36.29±6.12	37.05±5.43	0.730	0.467
	5days-treatment	18.35±4.40*	13.46±2.72*	7.386	<0.001
CRP (mg/L)	pre-treatment	30.28±6.30	29.75±5.89	0.483	0.630
	5days-treatment	16.43±4.22*	10.69±2.17*	9.430	<0.001
PCT (pg/mL)	pre-treatment	89.36±8.15	90.24±7.49	0.625	0.533
	5days-treatment	30.27±6.56*	22.19±4.35*	8.028	<0.001
CTGF (μg/L)	pre-treatment	214.46±27.28	215.73±26.91	0.261	0.795
	5days-treatment	122.85±19.60*	94.28±17.53*	8.535	<0.001
TGF-β1 (pg/L)	pre-treatment	76.28±9.52	75.71±10.14	0.323	0.747
	5days-treatment	47.31±7.12*	39.28±5.57*	6.963	<0.001

Note: Compared with before treatment, * $P < 0.05$.

3.4 Comparison of Arterial Blood Gas Analysis Indicators Between the Two Groups

After 5 days of treatment, the control group had significantly lower levels of PaO₂, PaCO₂, SaO₂, and PaO₂/FiO₂ compared to the study group, with all differences being statistically significant ($P < 0.001$), as shown in Table 4.

Table 4 Comparison of Arterial Blood Gas Analysis Indicators Between the Two Groups ($\bar{x} \pm s$)

Item	Control group (n=64)	Research group (n=60)	<i>t</i>	<i>P</i>	
PaO ₂ (mmHg)	pre-treatment	50.83±6.27	51.37±6.05	0.488	0.627
	5days-treatment	85.12±5.19*	89.46±7.10*	3.903	<0.001
PaCO ₂ (mmHg)	pre-treatment	73.25±5.67	73.75±6.21	0.469	0.640
	5days-treatment	85.56±4.43*	93.57±5.26*	9.192	<0.001
SaO ₂ (%)	pre-treatment	82.59±2.67	83.14±2.49	1.184	0.239
	5days-treatment	90.36±2.68*	96.57±1.54*	15.682	<0.001
PaO ₂ /FiO ₂ (mmHg)	pre-treatment	254.78±21.57	253.67±22.16	0.283	0.778
	5days-treatment	322.19±26.45*	365.34±30.58*	8.419	<0.001

Note: Compared with before treatment, * $P < 0.05$.

3.5 Comparison of Clinical Efficacy Between the Two Groups

The overall efficacy rate in the control group was 81.25%, which was significantly lower than the 95.00% efficacy rate in the study group, with a statistically significant difference ($P < 0.05$), as shown in Table 5.

Table 5 Comparison of Clinical Efficacy Between the Two Groups [Case(n%)]

Group	Clinical control	remarkable	effective	In vain	Total effective rate (%)
Control group (n=64)	24	20	8	12	52 (81.25)
Research group (n=60)	36	15	6	3	57 (95.00)
χ^2/z		8.680			5.506
P		0.034			0.019

3.6 Comparison of Adverse Reactions Between the Two Groups

In the control group, there were 2 cases of dizziness, 1 case of rash with itching, 2 cases of nausea and vomiting, 1 case of hoarseness, and 1 case of diarrhea, resulting in an adverse reaction rate of 10.94%. In the study group, there was 1 case of dizziness, 2 cases of nausea and vomiting, and 1 case of palpitations, with an adverse reaction rate of 6.67%. The difference between the two groups was not statistically significant ($\chi^2=0.699$, $P=0.403$).

4 DISCUSSION

4.1 Current Status of Combined Traditional Chinese and Western Medicine in the Treatment of COPD

Traditional Chinese medicine (TCM) considers that lung distension often occurs as a secondary condition following chronic pulmonary diseases such as chronic cough and asthma. This condition arises when lung Qi stagnates internally for an extended period, failing to disseminate and descend, which leads to the chest becoming distended and full. This results in symptoms such as palpitations, chest tightness, breathlessness, and even dizziness, blurred vision, and cyanosis of the lips and nails[10]. This understanding is consistent with Western medical theories of COPD. Prolonged progression of COPD can also lead to various complications such as cardiovascular diseases, osteoporosis, and lung cancer[11]. The persistent obstruction of the airways creates a vicious cycle, where Qi deficiency impairs the transformation and transportation of fluids and nutrients, affecting the kidneys, spleen, and stomach. Consequently, the protective Qi and blood are compromised, making the condition prone to relapse. COPD commonly affects the elderly and is often chronic and difficult to cure, so the main clinical approach is to control symptoms and improve ventilation and gas exchange function[12]. However, current research indicates that while Western medicines can improve patients' exercise tolerance and alleviate dyspnea, they frequently cause adverse reactions in the nervous and digestive systems and can lead to drug resistance, especially in patients using opioids or those requiring long-term treatment, which increases the risk of addiction[13-14]. Huang P and colleagues conducted a meta-analysis of 490 COPD patients and found that combined Chinese and Western medicine treatments significantly improved lung function and overall efficacy compared to Western medicine alone, with higher safety, especially in patients with COPD complicated by respiratory failure[15]. The results of this study show that after 5 days of treatment, both the main symptoms, secondary symptoms, and total TCM syndrome scores in the two groups significantly improved. This is attributed to the fact that oxygen therapy can increase blood oxygen saturation and effectively alleviate lung hypoxia, while Western medicines such as budesonide suspension and fluticasone inhalation aerosol stabilize the internal cellular environment, enhance immune function, relieve airway hyperreactivity and inflammation, and relax bronchial smooth muscle, reducing airflow limitation[16-17]. However, the improvement in TCM syndrome scores was more significant in the study group, indicating that the combination of Xuanfei Baidu Granules with Western medicine for treating damp-heat obstructed lung-type COPD can more rapidly control symptoms and enhance patient comfort.

4.2 Clinical Effects of Xuanfei Baidu Granules

Xuanfei Baidu Granules are a traditional Chinese medicine formulation developed based on the classic prescriptions of Ma Xing Shi Gan Decoction, Ma Xing Yi Gan Decoction, Qianjin Weijing Decoction, and Ting Li Da Zao Xie Fei Decoction, as well as clinical experience, specifically targeting lung diseases caused by damp-heat obstructing the lung. This formulation not only transforms dampness and strengthens the Yang, but also disseminates the lung, resolves exterior conditions, clears heat and detoxifies, and expels wind[18]. Therefore, after 5 days of treatment, the study group showed significantly higher levels of FEV1, FVC, FEV1/FVC, PEF, and 6MWT compared to the control group, and had lower Raw and COPD CAT scores. This indicates that Xuanfei Baidu Granules can markedly improve exercise

endurance and cardiopulmonary function in COPD patients, reduce airway resistance, and enhance the lung tissue's self-ventilation and gas exchange function. However, a bibliometric analysis[19] has shown that while there are certain achievements in the clinical and bioinformatics research of Chinese medicine formulations, the molecular mechanisms remain unclear. Moreover, even for the same damp-heat obstructed lung-type COPD, there is considerable individual variability. Directly using Chinese medicine granules may lose the advantage of adjusting prescriptions based on symptoms, which limits the effectiveness of traditional medicine. Therefore, for patients with multiple pulmonary diseases or acute symptoms, it is essential to adjust the treatment plan based on the drug response and control of clinical symptoms and signs to optimize individualized treatment as much as possible.

Xuanfei Baidu Granules are composed of over ten traditional Chinese medicinal herbs. Among them, Ephedra primarily alleviates the five zang organs (pathogenic factors) and regulates the protective qi, expels cold and heat, and when combined with Gypsum, it can disseminate the lung, relieve asthma, and promote diuresis to reduce swelling[20]. The dried *Atractylodes rhizome* (processed with bran) dries dampness, strengthens the spleen, and resolves cold, and when used with *Agastache* and *Artemisia annua*, it is effective for symptoms caused by damp-heat obstructing the lung, such as fever, fatigue, reduced appetite, and disturbed lung qi or reversed qi flow[21]. According to the "Compendium of Materia Medica," Japanese knotweed and *Verbena* help to drain dampness, resolve jaundice, invigorate blood, and dispel stasis. When used with Coix seed and Reed root, they not only promote the smooth flow of qi and blood but also strengthen the spleen and stomach, clear heat, and transform phlegm. Additionally, Perilla seed, bitter Apricot kernel, and *Citrus reticulata* peel are effective in stopping cough, relieving asthma, and generating fluids. Together, the formulation performs the functions of disseminating the lung, transforming dampness, and detoxifying, which helps to clear obstructed lung qi and drain internal damp-heat[22-23]. Moreover, network pharmacology has demonstrated that bitter Apricot kernel, Licorice, and Japanese knotweed possess anti-inflammatory, antibacterial, and antiviral properties, effectively inhibiting pathogen proliferation. Reed root contains vitamins A, C, B2, various minerals, and organic acids, which reduce harmful substances and toxins' irritation to the respiratory mucosa, alleviate airway hyperreactivity, and decrease the frequency of asthma, cough, and sputum production[24-25]. Therefore, Xuanfei Baidu Granules significantly enhance the patient's immunity, suppress inflammation-related factor secretion, and reduce respiratory and pulmonary infections.

4.3 Mechanism of Xuanfei Baidu Granules Combined with Western Medicine in the Treatment of Damp-Heat Obstructing the Lung in COPD

Clinical research indicates that the progression and control of damp-heat obstructing the lung type of COPD are related to multiple inflammatory mechanisms. Neutrophils can release arachidonic acid, which, under the action of enzymes, generates thromboxanes, prostaglandins, eosinophil chemotactic factors, fibrinolysin, and coagulation factors. These substances significantly affect vascular caliber and permeability, leading to inflammation and pain, and impacting the coagulation function of tissues and organs[26]. Additionally, leukotrienes secreted by neutrophils play a stronger role than histamine in allergen-mediated nasal allergic reactions and can exacerbate respiratory symptoms during COPD progression[27]. LYMPH% is usually associated with the severity of viral and bacterial infections and is an important indicator of the patient's immune status[28]. IL-6 is a multifunctional cytokine that can induce the liver to produce acute-phase proteins such as CRP, complement C3, fibrinogen, and serum amyloid A (SAA), and stimulate endothelial cells to produce IL-8 and intercellular adhesion molecule-1 (ICAM-1). This mediates various inflammatory and immune pathways, increases vascular permeability and inflammatory exudate, and promotes disease development[29]. Niu WH et al.[30] established a molecular docking model and analyzed the chemical components of Xuanfei Baidu Granules and other traditional Chinese medicine formulas for damp-heat obstruction. They found that the active compounds in these herbs can interact directly with IL-6, thereby reducing inflammation and promoting patient recovery through a negative feedback mechanism.

IL-17 not only induces the synthesis and secretion of various inflammatory mediators such as IL-6, IL-1 β , and TNF- α by epithelial cells, endothelial cells, and fibroblasts, but it also adapts the immune response by regulating cytokine production[31]. For example, IL-17 enhances local and systemic Th2 cell responses through its IL17RA and IL17RB receptors, activating the JAK2-STAT5A pathway, leading to immune dysregulation and exacerbation of local inflammation[32]. CTGF is closely related to tissue fibrosis, and TGF- β 1 is involved in the dynamic balance of cell growth, differentiation, apoptosis, and immune function[33]. After 5 days of treatment, NEUT%, LYMPH%, IL-6, IL-17, and CRP were significantly lower in the study group compared to the control group. This can be attributed to the following mechanisms[34-35]: (1) Cefoperazone-sulbactam is primarily used to treat respiratory, skin, and tissue infections caused by sensitive bacteria, and it has a strong inhibitory effect on β -lactamases produced by most Gram-negative bacteria. Combined with other bronchodilators and Xuanfei Baidu Granules, it can significantly downregulate the expression of inflammatory factors and restore immune and inflammatory balance; (2) Western medicine treatment not only rapidly controls symptoms but also effectively inhibits the release of inflammatory mediators by neutrophils, enhances ciliary movement in the airways, and promotes the expulsion of irritants; (3) The core pathogenesis of damp-heat obstructing the lungs involves pathogenic factors entering the body, generating phlegm and dampness that obstructs the lungs. By expelling damp-heat from the lungs with Xuanfei Baidu Granules, the balance of Qi and blood is restored, enhancing the metabolism of nutrients and promoting the nourishment of organs and consolidation of the defensive Qi, thereby reducing the risk of lung fibrosis or substantial damage. Consequently, after 5 days of treatment, PCT, CTGF, and TGF- β 1 were significantly lower in the study group. Moreover, the

improvement in blood gas indicators in the study group was also superior to that in the control group. This suggests that the combination of Xuanfei Baidu Granules and Western medicine significantly reduces the incidence of hypoxemia and the hypoxic damage to vital organs such as the heart, brain, and lungs.

5 SUMMARY

In summary, the combination of Xuanfei Baidu Granules and Western medicine for treating damp-heat obstructing the lungs type of COPD significantly improves patients' cardiopulmonary function and increases blood oxygen levels, thereby alleviating airflow limitation and symptoms such as cough. This treatment also reduces Traditional Chinese Medicine (TCM) syndrome scores and inflammation levels, enhancing clinical efficacy. However, this study has limitations, including a short treatment duration, and the long-term safety, feasibility, and recurrence of symptoms after treatment remain unknown. Additionally, given the complex etiology and diverse syndromes of COPD, the clinical application of Xuanfei Baidu Granules still has certain limitations. Future clinical studies need to incorporate extensive data to further explore its value.

FUNDING

This study was supported by the Hunan Provincial People's Hospital Medical Union Special Research Fund Project(2023YLT006).

CONFLICT OF INTEREST

The authors have no relevant financial or non-financial interests to disclose.

REFERENCES

- [1] Ferrera MC, Labaki WW, Han MK. Advances in Chronic Obstructive Pulmonary Disease. *Annu Rev Med*, 2021, 27(72): 119-134.
- [2] Yang IA, Jenkins CR, Salvi SS. Chronic obstructive pulmonary disease in never-smokers: risk factors, pathogenesis, and implications for prevention and treatment. *Lancet Respir Med*, 2022, 10(5): 497-511.
- [3] Lange P, Çolak Y, Ingebrigtsen TS, et al. Long-term prognosis of asthma, chronic obstructive pulmonary disease, and asthma-chronic obstructive pulmonary disease overlap in the Copenhagen City Heart study: a prospective population-based analysis. *Lancet Respir Med*, 2016, 4(6): 454-462.
- [4] Emeryk A, Emeryk-Maksymiuk J. Short-acting inhaled β 2-agonists: why, whom, what, how? *Adv Respir Med*, 2020, 88(5): 443-449.
- [5] Amegadzie JE, Gamble JM, Farrell J, et al. Association between Inhaled β 2-agonists Initiation and Risk of Major Adverse Cardiovascular Events: A Population-based Nested Case-Control Study. *Int J Chron Obstruct Pulmon Dis*, 2022, 20(17): 1205-1217.
- [6] Wei YP, Wang JM, Dong XY. Wang Youkui's treatment of chronic obstructive pulmonary disease from the Five viscera and five Elements based on "Lung-gui theory" . *Journal of Zhejiang Chinese Medicine University*, 2023, 47(8): 869-873.
- [7] Kahnert K, Jörres RA, Behr J, Welte T. The Diagnosis and Treatment of COPD and Its Comorbidities. *Dtsch Arztebl Int*, 2023, 120(25): 434-444.
- [8] Chen LC, Chen XS, WU XH, et al. Systematic evaluation of distribution of traditional Chinese medicine syndromes of novel coronavirus pneumonia. *Pharmacology and Clinic of Traditional Chinese medicine*, 2020, 36(2): 46-50.
- [9] Dai GC, Zhang XG, Gao WW, et al. Yinqiao Powder combined with Sanren Decoction in the treatment of 20 cases of common dampness-toxin pneumonitis syndrome of novel coronavirus pneumonia. *Journal of Anhui College of Traditional Chinese Medicine*, 2020, 39(5): 1-4.
- [10] Huang JH, Bai SL, Liu R. Discussion on TCM treatment of lung diseases based on the theory of "Qi and blood" . *Shaanxi Journal of Traditional Chinese Medicine*, 2023, 44(4): 483-486.
- [11] Zhou C, Qin Y, Zhao W, et al. International expert consensus on diagnosis and treatment of lung cancer complicated by chronic obstructive pulmonary disease. *Transl Lung Cancer Res*, 2023, 12(8): 1661-1701.
- [12] Mao X, Hu F, Peng J, et al. Writing Expert Group of Expert Consensus on Expert Consensus on the whole process management of lung rehabilitation in lung cancer patients undergoing surgery complicated with chronic obstructive pulmonary disease, the Lung Cancer Professional Committee of China Medical Education Association; Writing Expert Group of Expert Consensus on Expert Consensus on the whole process management of lung rehabilitation in lung cancer patients undergoing surgery complicated with chronic obstructive pulmonary disease, the Lung Cancer Professional Committee of China Medical Education Association. Expert consensus on multi-disciplinary treatment, whole-course pulmonary rehabilitation management in patients with lung cancer and chronic obstructive lung disease. *Ann Palliat Med*, 2022, 11(5): 1605-1623.
- [13] Gao Z, Liu Y, Zhang J, et al. Effect of Jianpi therapy in treatment of chronic obstructive pulmonary disease: a systematic review. *J Tradit Chin Med*, 2013, 33(1): 1-8.
- [14] Liu M, Xiao W, Du L, et al. Effectiveness and safety of opioids on breathlessness and exercise endurance in

- patients with chronic obstructive pulmonary disease: A systematic review and meta-analysis of randomised controlled trials. *Palliat Med*, 2023, 37(9): 1365-1378.
- [15] Huang P, Lin X, Liu Y, et al. The efficacy and safety of combined traditional Chinese and western medicine in the treatment of chronic obstructive pulmonary disease complicated with respiratory failure: a systematic review and meta-analysis study. *Ann Palliat Med*, 2022, 11(3): 1102-1111.
- [16] Dobrowolska K, Emeryk A, Janeczek K, et al. Influence of Physicochemical Properties of Budesonide Micro-Suspensions on Their Expected Lung Delivery Using a Vibrating Mesh Nebulizer. *Pharmaceutics*, 2023, 15(3): 752.
- [17] N V, Lokavarapu B R. Enhanced Optimal Parameter-Based Nebulizer Design for Flow Analysis of Fluticasone Propionate. *AAPS PharmSciTech*, 2023, 24(4): 85.
- [18] Pang WT, Yang FW, Zheng WK, et al. Study on clinical efficacy of Xuanfeixuedu granules in the treatment of novel coronavirus pneumonia infected by Omicron strain. *Tianjin Traditional Chinese Medicine*, 2022, 39(9): 1093-1098.
- [19] Dayuan Z, Lan L, Luhua X, et al. A bibliometric analysis of research related Chinese Medicine in the prevention and treatment of corona virus disease 2019. *Heliyon*, 2022, 8(11): e11120.
- [20] Feng LM, Liu XY, Zhang L. Clinical efficacy of Xuanfeixuedu granules in the treatment of novel coronavirus pneumonia (Omicrone). *Tianjin traditional Chinese medicine*, 2022, 39(5): 545-550.
- [21] Li CM, Zhang Z, Zhang YF, et al. Effects of YiQxuanfei Decoction on pulmonary function and serological indexes in patients with chronic obstructive pulmonary disease in stable stage of lung Qi deficiency. *World Journal of Integrated Chinese and Western Medicine*, 2020, 15(11): 2067-2071.
- [22] Deng YH, Liu Y. Effect of self-prepared Qingre Xuanfei Decoction on the treatment of acute exacerbation of chronic obstructive pulmonary disease, lung function and changes of serum inflammatory factors. *Thrombosis and hemostasis*, 2020, 26(6): 929-931.
- [23] Dai GM, Wang H. Effect of inhalation drug therapy on inflammatory factors and quality of life on stable chronic obstructive pulmonary disease. *Pak J Med Sci*, 2024, 40(7): 1403-1409.
- [24] Chen Y, Wang Y, Li Z, et al. Exploration of the Mechanism of Shengxian Decoction Against Chronic Obstructive Pulmonary Disease Based on Network Pharmacology and Experimental Verification. *Assay Drug Dev Technol*, 2023, 21(6): 258-272.
- [25] Deng L, Zhang X, Dong Y, et al. Erchen decoction combined with Sanziyangqin decoction for chronic obstructive pulmonary disease: A protocol for systematic review and meta-analysis. *Medicine (Baltimore)*, 2020, 99(40): e22315.
- [26] Toller-Kawahisa JE, Hiroki CH, Silva CMS, et al. The metabolic function of pyruvate kinase M2 regulates reactive oxygen species production and microbial killing by neutrophils. *Nat Commun*, 2023, 14(1): 4280.
- [27] Guo P, Li R, Piao TH, et al. Pathological Mechanism and Targeted Drugs of COPD. *Int J Chron Obstruct Pulmon Dis*, 2022, 12(17): 1565-1575.
- [28] Han M, Kang R, Zhang C. Lymph Node Mapping for Tumor Micrometastasis. *ACS Biomater Sci Eng*, 2022, 8(6): 2307-2320.
- [29] Liu T, Zhang Z, Shen W, Wu Y, Bian T. MicroRNA Let-7 Induces M2 Macrophage Polarization in COPD Emphysema Through the IL-6/STAT3 Pathway. *Int J Chron Obstruct Pulmon Dis*, 2023, 13(18): 575-591.
- [30] Niu WH, Wu F, Cao WY, et al. Network pharmacology for the identification of phytochemicals in traditional Chinese medicine for COVID-19 that may regulate interleukin-6. *Biosci Rep*, 2021, 41(1): BSR20202583.
- [31] Henen C, Johnson EA, Wiesel S. Unleashing the Power of IL-17: A Promising Frontier in Chronic Obstructive Pulmonary Disease (COPD) Treatment. *Cureus*, 2023, 15(7): e41977.
- [32] Ding F, Han L, Fu Q, et al. IL-17 Aggravates *Pseudomonas aeruginosa* Airway Infection in Acute Exacerbations of Chronic Obstructive Pulmonary Disease. *Front Immunol*, 2022, 13(12): 811803.
- [33] Shen YW, Zhou YD, Chen HZ, et al. Targeting CTGF in Cancer: An Emerging Therapeutic Opportunity. *Trends Cancer*, 2021, 7(6): 511-524.
- [34] Deng Q, Song C, Liu Q. Effect of Xuanfei Xiedu Granule combined with non-invasive positive pressure ventilation on patients with acute exacerbation of chronic obstructive pulmonary disease with type II respiratory failure. *Chinese Minkang Medicine*, 2023, 35(24): 92-95.
- [35] Ritchie AI, Wedzicha JA. Definition, Causes, Pathogenesis, and Consequences of Chronic Obstructive Pulmonary Disease Exacerbations. *Clin Chest Med*, 2020, 41(3): 421-438.

APPLICATION AND PROGRESS OF CT ANGIOGRAPHY–X-RAY IMAGE FUSION TECHNOLOGY IN ENDOVASCULAR SURGERY: A LITERATURE REVIEW

YiRen Lai

School of Health Science and Engineering, University of Shanghai for Science and Technology, Shanghai 200093, China.

Corresponding Email: 942568132@qq.com

Abstract: CT Angiography (CTA)-X-ray image fusion technology has seen significant advancements in recent years, offering a more precise and efficient imaging solution for endovascular interventions in vascular diseases. By integrating preoperative CTA images with intraoperative X-ray fluoroscopy, this technology enables dynamic visualization of vascular structures and interventional devices, allowing clinicians to perform complex procedures with greater accuracy. Compared with conventional imaging techniques, CTA-X-ray image fusion reduces reliance on contrast agents, minimizes radiation exposure, and shortens operative duration. This paper systematically introduces the definition, principles, and procedural workflow of this technology, outlining its key technical developments and clinical applications. The ability to provide real-time guidance for interventional procedures enhances the accuracy of device deployment, particularly in complex vascular anatomies. Furthermore, its application has expanded across various vascular interventions, demonstrating significant potential in improving surgical outcomes. As the technology continues to evolve, its role in endovascular therapy is expected to become increasingly prominent, contributing to more precise and safer interventional strategies.

Keywords: Image fusion; Endovascular intervention; Multimodal imaging; CT angiography; X-ray

1 INTRODUCTION

The rapid advancement of endovascular therapeutic techniques has enabled interventions for increasingly complex vascular diseases. The management of such conditions relies heavily on radiologic imaging, with preoperative and postoperative computed tomography angiography (CTA) and intraoperative fluoroscopic imaging serving as fundamental modalities in vascular assessment. CTA provides high-resolution imaging of vascular anatomy across the entire body, allowing for comprehensive evaluation of vascular lesions and their spatial relationship with surrounding structures. This detailed visualization facilitates meticulous preoperative planning and long-term monitoring. Intraoperative fluoroscopy, in contrast, offers real-time tracking of interventional device progression, providing essential procedural guidance for endovascular interventions.

Despite their advantages, both imaging techniques have inherent limitations. CTA generates static images that, while crucial for surgical planning, lack real-time procedural guidance. Conversely, X-ray fluoroscopy delivers real-time imaging but is inadequate for visualizing soft tissue characteristics such as vessel morphology, tortuosity, calcifications, and lesion dimensions, making it challenging for clinicians to precisely determine vascular spatial positioning. Additionally, alternative imaging modalities, including magnetic resonance imaging (MRI), magnetic resonance angiography (MRA), and three-dimensional digital subtraction angiography (3D-DSA), also suffer from constraints in real-time vascular visualization and accurate localization of interventional devices, limiting their utility in guiding endovascular procedures [1-4].

To address these challenges, CTA-X-ray image fusion technology has been proposed. This technique integrates the high-resolution preoperative imaging of CTA with the real-time intraoperative capabilities of X-ray fluoroscopy, enabling continuous visualization of vascular structures and interventional devices throughout the procedure. By enhancing procedural precision, this technology facilitates accurate stent deployment, reduces contrast agent usage, shortens operative time, and optimizes surgical accuracy. The integration of static and dynamic imaging offers a significant advancement in procedural safety and efficiency for complex endovascular interventions. The following sections provide a comprehensive review of the clinical applications and recent developments of CTA real-time X-ray image fusion in vascular disease diagnosis and treatment.

2 DEFINITION AND PRINCIPLES OF CTA-X-RAY IMAGE FUSION

CTA-X-ray image fusion is a technique that integrates three-dimensional (3D) reconstructions of computed tomography angiography (CTA) data with intraoperative X-ray fluoroscopic imaging during endovascular interventions. This process involves image registration, alignment, and fusion to generate a composite image that dynamically synchronizes reconstructed vascular structures with real-time fluoroscopic views. By superimposing the 3D vascular reconstruction from CTA onto live X-ray fluoroscopy, clinicians can more accurately determine the spatial relationships between interventional instruments and vascular anatomy throughout the procedure [1,5-7].

The core principle of image fusion is based on the alignment of features that are simultaneously visible in both the CTA 3D reconstruction and the X-ray fluoroscopic image. These reference points may include anatomical structures, such as bones, or artificially introduced markers, such as radiopaque fiducials. By registering these features, the fused image preserves critical spatial information, including vascular position, geometry, and its relationship with surrounding tissues. This enhanced visualization facilitates more precise interventional guidance, improving procedural accuracy while reducing contrast medium usage and operative duration [8-11].

3 IMPLEMENTATION STEPS OF CTA-X-RAY IMAGE FUSION

The process of CTA-X-ray image fusion can be broadly categorized into two critical steps: image segmentation and image alignment and fusion. Among these, the accuracy of image alignment is pivotal to the success of the fusion process, as it directly determines the effectiveness and reliability of the fused image.

3.1 Image Segmentation

Image segmentation is a fundamental problem in image processing and analysis, aimed at partitioning an image into distinct regions that are mutually exclusive and internally homogeneous. Each segmented region represents a meaningful component of the image, adhering to specific criteria for consistency. Segmentation forms the basis for subsequent 3D reconstruction, with its accuracy directly influencing the precision of the final reconstructed model [5]. In the realm of medical imaging, segmentation techniques are primarily categorized into traditional methods relying on digital image processing and modern approaches based on deep learning algorithms [12]. Software tools such as Mimics, 3D Slicer, Simpleware, and Amira facilitate rapid segmentation and 3D reconstruction of medical images, aiding clinicians in extracting regions of interest (e.g., diseased tissues, vascular structures) [13]. By providing a clearer understanding of the anatomical features, segmentation plays a critical role in enhancing surgical precision, offering valuable guidance for interventional procedures.

3.2 Image Alignment and Fusion

Image alignment refers to the process of identifying a spatial configuration in which corresponding points from two distinct images coincide precisely, ensuring agreement in both anatomical structure and spatial location. The objective is to achieve congruence across all anatomical points of interest, or at least those relevant to diagnostic and surgical considerations, in both images [14,15].

In recent years, numerous methods for image alignment have been proposed, including the alignment of geometric moments, polynomial transformations such as correlation coefficients and spline interpolation, as well as mutual-information-based techniques aimed at enhancing the accuracy of three-dimensional alignment and fusion. Although the refinement of alignment accuracy remains a central challenge, the pursuit of fully automated, human-independent methods may not always be practical, as it often complicates the algorithmic process and increases computational time. A more feasible approach is to combine human-computer interaction to expedite alignment processes. Current image fusion technologies typically rely on image correlation coefficients, supplemented by manual calibration, to achieve accurate alignment [5].

Medical imaging provides crucial structural data, which, when combined through image fusion, enables comprehensive spatial analysis. Fusion of multimodal images, such as CTA 3D reconstructions and X-ray fluoroscopic images, offers precise localization, size, and geometry of anatomical structures (e.g., blood vessels), as well as their spatial relationships with surrounding tissues, thereby facilitating more efficient surgical planning and execution [16-18].

4 CLINICAL APPLICATIONS OF CTA-X-RAY IMAGE FUSION

CTA-X-ray image fusion technology offers substantial advantages in endovascular interventions, particularly for complex and anatomically challenging procedures. By enhancing visualization and spatial localization, image fusion significantly reduces surgical complexity and procedural difficulty. The following sections will explore the diverse clinical applications of CTA-X-ray image fusion across various interventional scenarios [7].

4.1 CTA-X-ray Image Fusion in Aortic Diseases

CTA-X-ray image fusion technology plays a critical role in endovascular repair of aortic diseases, offering significant advantages in reducing contrast agent usage, shortening procedure time, and enhancing surgical precision. In the treatment of abdominal aortic lesions involving visceral branches, conventional approaches require repeated imaging to confirm whether the placement of a stent or balloon affects key branches such as the renal artery, celiac trunk, or superior mesenteric artery. By contrast, CTA-X-ray image fusion enables clinicians to preoperatively mark branch openings that may be impacted by the stent, allowing for intuitive visualization of vascular morphology and branch locations. This reduces the need for repeated imaging, improves the accuracy of stent deployment, and ultimately enhances procedural efficiency while minimizing contrast exposure [6,19-30].

In endovascular repair of aortic arch lesions, a primary concern is the potential impact of interventional devices on the three major branches of the aortic arch—the brachiocephalic trunk, left common carotid artery, and left subclavian

artery—where inadvertent coverage could lead to severe complications. To mitigate these risks, techniques such as windowing and chimney stenting have been introduced; however, they still necessitate multiple imaging confirmations. CTA-X-ray image fusion technology provides real-time intraoperative visualization of the spatial relationship between interventional devices and the three major aortic arch branches, facilitating more precise device placement while reducing contrast agent use and procedure duration [31-35].

Overall, CTA-X-ray image fusion technology holds significant clinical value in the endovascular repair of complex aortic lesions. By integrating preoperative vascular mapping with intraoperative image overlay, this technique enables more accurate device placement, reduces reliance on traditional contrast-based confirmation, and enhances both the safety and efficiency of the procedure.

4.2 CTA-X-ray Image Fusion in Cardiac Diseases

In vascular endoluminal interventions involving valve replacement, precise anatomical localization is critical. For example, in transcatheter aortic valve replacement (TAVR), clinicians must accurately identify the axial positions of the left coronary sinus, right coronary sinus, and non-coronary sinus, as well as measure the diameter of the sinus orifice/annulus, the width of the aortic root, and the distance from the sinus floor to the left and right coronary arteries. Additionally, precise localization of the aortic valve is essential to ensure that the prosthetic valve displaces the diseased native valve while maintaining unobstructed flow through the coronary arteries. Beyond preoperative measurement accuracy, real-time intraoperative visualization of valve positioning and deployment is crucial for procedural success [36].

Currently, X-ray fluoroscopy remains the primary imaging modality used intraoperatively; however, its ability to provide detailed anatomical assessment is limited. CTA-X-ray image fusion technology enhances intraoperative guidance by integrating preoperative measurements into the live imaging environment. Clinicians can annotate preoperative assessments directly onto the image in the form of circular markers, allowing for intuitive real-time verification of prosthetic valve positioning. This approach reduces procedural complexity, shortens operative duration, and improves overall surgical success rates by facilitating more precise deployment of the prosthetic valve.

4.3 CTA-X-ray Image Fusion in Tumors

CTA-X-ray image fusion technology also holds significant clinical value in tumor interventional procedures. In the case of liver cancer, this technology enables precise preoperative localization and selection of tumor-feeding vessels, facilitating optimal interventional path planning. During the procedure, real-time fusion imaging provides accurate intraoperative guidance, allowing clinicians to efficiently identify and navigate to the target vessels for embolization. This approach enhances the precision of tumor interventions while significantly reducing procedural duration, improving both treatment efficacy and surgical efficiency [37,38].

5 DEVELOPMENT OF CTA-X-RAY IMAGE FUSION

CTA-X-ray image fusion technology has been widely adopted in vascular endoluminal interventions, offering enhanced visualization and procedural precision. Originally developed for geological analysis, image fusion techniques have been progressively integrated into vascular interventions with advancements in medical imaging [39]. While conventional angiographic contrast agents provide essential intraoperative imaging, their use is associated with potential risks to both patients and clinicians. To mitigate these challenges, CTA-X-ray image fusion has emerged as a viable alternative, aiming to minimize contrast agent usage while improving procedural accuracy and efficiency.

With the rapid evolution of image fusion technology, two primary system types have been developed. Hybrid operating room (OR)-based fusion systems, such as Siemens ARTIS icono, Philips VesselNavigator, and GE Allia IGS 7, are designed for seamless integration into specialized surgical environments. In contrast, flexible, OR-compatible systems, such as Cydar Imaging Guidance and THERENVA's Endonaut, offer deployment versatility across various clinical settings [1,40].

The Siemens ARTIS icono system enhances intraoperative guidance by processing and aligning CTA datasets in real time, enabling precise localization of the aortic vessel wall and branch vessels, thereby optimizing stent placement and reducing contrast media dependency. The Philips VesselNavigator system incorporates automated vessel segmentation and 3D modeling, overlaying real-time intraoperative X-ray fluoroscopy to streamline procedures and minimize contrast agent use. GE's Allia IGS 7 system features personalized user interfaces and real-time dose optimization, simplifying workflows while reducing radiation exposure. Meanwhile, Cydar Imaging Guidance and the Endonaut system leverage deep learning algorithms to generate and dynamically update 3D vascular pathways, offering real-time navigation that further improves surgical accuracy while reducing reliance on contrast agents [41,42].

Overall, image fusion technology represents a major advancement in vascular endoluminal interventions, significantly reducing contrast agent use, lowering radiation exposure, and enhancing procedural planning and execution. As these innovations continue to refine interventional techniques, image fusion is poised to transform traditional surgical approaches, improving both the safety and efficiency of endovascular procedures.

6 LIMITATIONS OF CTA-X-RAY IMAGE FUSION

Despite its clinical advantages, current CTA- X-ray image fusion technology has several limitations. Firstly, existing systems do not achieve fully dynamic real-time fusion, where the X-ray fluoroscopic image can automatically integrate with the corresponding CTA 3D reconstruction model at any angle and orientation. Instead, current techniques rely on preoperative planning, selecting optimal imaging angles for endovascular interventions. The fusion process is performed in advance using positional parameters obtained from imaging equipment, ensuring that clinicians have pre-prepared fused images for various procedural angles. Consequently, these systems do not offer true real-time fusion but rather rely on precomputed image overlays.

Secondly, most image fusion software requires access to positional parameters from imaging hardware, which are often proprietary and restricted by device manufacturers. As a result, many existing fusion technologies are dependent on specific company hardware and cannot function universally across different imaging platforms. This lack of interoperability limits their broader adoption in clinical practice.

Finally, the accuracy of CTA-X-ray image fusion remains a challenge, influenced by three primary factors. The first is vascular displacement due to respiratory motion. CTA data are typically acquired during breath-hold inspiration, which does not reflect the continuous low-tidal volume ventilation commonly used in general anesthesia. Studies have reported respiration-induced vascular misalignment, particularly at the level of the aortic arch and distal visceral branches. The second factor is vessel deformation caused by interventional devices. The introduction of stiff or rigid instruments into tortuous vessels, such as the iliac arteries or the distal horizontal segment of the descending aorta, can result in vessel straightening and anatomical distortion. As diagnostic CTA captures vessels in their natural state, such alterations introduce alignment discrepancies. The third factor is patient movement, which can further displace vascular structures. Manual calibration is necessary to correct misalignments when clinicians detect such discrepancies intraoperatively [34].

A study assessing the accuracy of fusion imaging during endovascular aortic repair (EVAR) reported an average misalignment error of 2 ± 2.5 mm (range: 0–7 mm) at the renal artery origin and 0.80 ± 1.66 mm (range: 0–5 mm) at the iliac bifurcation, highlighting the need for further refinement in fusion accuracy [43].

7 FUTURE TRENDS IN CTA-X-RAY IMAGE FUSION

The future development of CTA-X-ray image fusion should aim for a more real-time, widely applicable, and highly accurate system. Achieving this goal requires the integration of artificial intelligence (AI) with medical imaging technologies, particularly through deep learning approaches. AI-driven algorithms can enable automatic recognition of vascular and bony structures in CTA 3D reconstructions and X-ray fluoroscopic images, allowing for automated alignment and fusion without the need for preoperative manual adjustments. This advancement would enable true real-time image fusion, eliminating the dependence on precomputed overlays. Furthermore, deep learning-based AI can enhance alignment accuracy while reducing reliance on proprietary image localization parameters from different imaging devices. The ultimate objective of machine learning in this context is to allow systems to autonomously identify anatomical structures based on large-scale datasets, thereby facilitating broader adoption of image fusion technologies. Notably, companies such as CYDAR Medical (Cambridge, UK) and Endonaut (Rennes, France) have already made significant strides in developing hardware-independent image fusion systems, though further improvements are necessary to enhance their clinical utility [40,44-46].

Additionally, improving the accuracy of CTA-X-ray image fusion remains a critical challenge. Current misalignment errors primarily arise from respiratory motion and vascular deformation induced by rigid interventional devices. Respiration-related vascular discrepancies are most pronounced at the distal segments of the aortic arch and visceral branches, whereas rigid devices can cause significant vessel straightening, particularly in tortuous iliac arteries and the distal horizontal segment of the descending aorta. However, as long as the origin of the target vessel remains stable, these factors do not fundamentally limit the use of CTA-X-ray image fusion for procedural navigation. Future research on fusion accuracy should, therefore, prioritize optimizing alignment precision at the vessel origin to further enhance the reliability and applicability of this technology [2-3,34].

COMPETING INTERESTS

The authors have no relevant financial or non-financial interests to disclose.

REFERENCES

- [1] De Beaufort L M, Nasr B, Corvec T L, et al. Automated Image Fusion Guidance during Endovascular Aorto-Iliac Procedures: A Randomized Controlled Pilot Study. *Annals of Vascular Surgery*, 2021, 75: 86–93.
- [2] Chehab M, Kouri BE, Miller MJ, et al. Image Fusion Technology in Interventional Radiology. *Techniques in Vascular and Interventional Radiology*, 2023, 26(3): 100915. DOI: 10.1016/j.tvir.2023.100915. Epub 2023 Oct 21. PMID: 38071026.
- [3] Lu Qingsheng. Characteristics and Future Development Directions of Vascular Interventional Robotic Surgery. *Journal of Robotic Surgery*, 2020, 1(04): 231-235.
- [4] Brock KK, Chen SR, Sheth RA, et al. Imaging in Interventional Radiology: 2043 and Beyond. *Radiology*, 2023, 308(1): e230146. DOI: 10.1148/radiol.230146. PMID: 37462500; PMCID: PMC10374939.

- [5] Dong Yuning, Liu Tianliang, Dai Xiubin, et al. Theories and Applications of Medical Image Processing. Nanjing Southeast University Press: 202006.251, 2020.
- [6] Jones D W, Stangenberg L, Swerdlow N J, et al. Image Fusion and 3-Dimensional Roadmapping in Endovascular Surgery. *Annals of Vascular Surgery*, 2018, 52: 302–311.
- [7] Goudekettig S R, Heinen S G H, Ünlü Ç, et al. Pros and Cons of 3D Image Fusion in Endovascular Aortic Repair: A Systematic Review and Meta-analysis. *Journal of Endovascular Therapy*, 2017, 24(4): 595–603.
- [8] Zhou T, Cheng Q, Lu H, et al. Deep learning methods for medical image fusion: A review. *Computers in Biology and Medicine*, 2023, 160: 106959. DOI: 10.1016/j.compbimed.2023.106959. Epub 2023 Apr 20. PMID: 37141652.
- [9] Li Y, El Habib Daho M, Conze PH, et al. A review of deep learning-based information fusion techniques for multimodal medical image classification. *Computers in Biology and Medicine*, 2024, 177: 108635. DOI: 10.1016/j.compbimed.2024.108635. Epub 2024 May 22. PMID: 38796881.
- [10] Hertault A, Maurel B, Sobocinski J, et al. Impact of hybrid rooms with image fusion on radiation exposure during endovascular aortic repair. *European Journal of Vascular and Endovascular Surgery*, 2014, 48(4): 382–90.
- [11] Maurel B, Hertault A, Sobocinski J, et al. Techniques to reduce radiation and contrast volume during EVAR. *J Cardiovasc Surg (Torino)*, 2014, 55(2 Suppl 1): 123–31.
- [12] Wei Bowen. Effective Strategies for Medical Image Segmentation and 3D Reconstruction. East China Normal University, 2022. DOI: 10.27149/d.cnki.ghdsu.2022.001400.
- [13] Fang Weiyang, Lin Dongxin, Kou Wanfu, et al. Research Progress of Medical Image 3D Reconstruction Systems. *Chinese Journal of Medical Physics*, 2022, 39(07): 823-827.
- [14] Azam MA, Khan KB, Salahuddin S, et al. A review on multimodal medical image fusion: Compendious analysis of medical modalities, multimodal databases, fusion techniques and quality metrics. *Computers in Biology and Medicine*, 2022, 144: 105253. DOI: 10.1016/j.compbimed.2022.105253. Epub 2022 Feb 3. PMID: 35245696.
- [15] Yadav SP, Yadav S. Image fusion using hybrid methods in multimodality medical images. *Medical & Biological Engineering & Computing*, 2020, 58(4): 669-687. DOI: 10.1007/s11517-020-02136-6. Epub 2020 Jan 28. PMID: 31993885.
- [16] Azam M A, Khan K B, Salahuddin S, et al. A review on multimodal medical image fusion: Compendious analysis of medical modalities, multimodal databases, fusion techniques and quality metrics. *Computers in Biology and Medicine*, 2022, 144: 105253.
- [17] Kaur H, Koundal D, Kadyan V. Image Fusion Techniques: A Survey. *Archives of Computational Methods in Engineering: State of the Art Reviews*, 2021, 28(7): 4425–4447.
- [18] Dogra A, Ahuja C K, Kumar S. Image Integration Procedures in Multisensory Medical Images: A Comprehensive Survey of the State-of-the-art Paradigms. *Current Medical Imaging*, 2022, 18(5): 476–495.
- [19] Haga M, Fujimura K, Shindo S, et al. Efficacy of Fusion Imaging in Endovascular Revascularization of the Superficial Femoral Artery. *Annals of Vascular Surgery*, 2022, 80: 206–12.
- [20] Swerdlow NJ, Jones DW, Pothof AB, et al. Three-dimensional image fusion is associated with lower radiation exposure and shorter time to carotid cannulation during carotid artery stenting. *Journal of Vascular Surgery*. 2019, 69(4): 1111–20.
- [21] Tenorio ER, Oderich GS, Sandri GA, et al. Impact of onlay fusion and cone beam computed tomography on radiation exposure and technical assessment of fenestrated-branched endovascular aortic repair. *Journal of Vascular Surgery*, 2019, 69(4): 1045-1058.e3.
- [22] Stahlberg E, Sieren M, Anton S, et al. Fusion Imaging Reduces Radiation and Contrast Medium Exposure During Endovascular Revascularization of Iliac Steno-Occlusive Disease. *Cardiovasc Intervent Radiol*, 2019, 42(11): 1635–43.
- [23] Rolls AE, Rosen S, Constantinou J, et al. Introduction of a Team Based Approach to Radiation Dose Reduction in the Enhancement of the Overall Radiation Safety Profile of FEVAR. *European Journal of Vascular and Endovascular Surgery*, 2016, 52(4): 451–7.
- [24] Pruvot L, Lopez B, Patterson BO, et al. Hybrid Room: Does it Offer Better Accuracy in the Proximal Deployment of Infrarenal Aortic Endograft? *Annals of Vascular Surgery*, 2022, 82: 228–39.
- [25] Kaladji A, Villena A, Pascot R, et al. Fusion Imaging for EVAR with Mobile C-arm. *Annals of Vascular Surgery*, 2019, 55: 166–74.
- [26] Hayakawa N, Kodera S, Ohki N, et al. Efficacy of three-dimensional road mapping by fusion of computed tomography angiography and fluoroscopy in endovascular treatment of aorto-iliac chronic total occlusion. *Heart Vessels*, 2021, 36(3): 359–65.
- [27] Dias NV, Billberg H, Sonesson B, et al. The effects of combining fusion imaging, low-frequency pulsed fluoroscopy, and low-concentration contrast agent during endovascular aneurysm repair. *Journal of Vascular Surgery*, 2016, 63(5): 1147–55.
- [28] Dijkstra ML, Eagleton MJ, Greenberg RK, et al. Intraoperative C-arm cone-beam computed tomography in fenestrated/branched aortic endografting. *Journal of Vascular Surgery*, 2011, 53(3): 583–90.
- [29] Ahmad W, Obeidi Y, Majd P, et al. The 2D-3D Registration Method in Image Fusion Is Accurate and Helps to Reduce the Used Contrast Medium, Radiation, and Procedural Time in Standard EVAR Procedures. *Annals of Vascular Surgery*, 2018, 51: 177–86.

- [30] Ahmad W, Hasselmann HC, Galas N, et al. Image fusion using the two-dimensional-three-dimensional registration method helps reduce contrast medium volume, fluoroscopy time, and procedure time in hybrid thoracic endovascular aortic repairs. *Journal of Vascular Surgery*, 2019, 69(4): 1003–10.
- [31] Wanhainen A, Verzini F, Van Herzele I, et al. Editor's Choice – European Society for Vascular Surgery (ESVS) 2019 Clinical Practice Guidelines on the Management of Abdominal Aorto-iliac Artery Aneurysms. *European Journal of Vascular and Endovascular Surgery*, 2019, 57(1): 8–93.
- [32] Al Tannir Abdul Hafiz, Chahrour Mohamad A, Chamseddine Hassan, et al. Outcomes and cost-analysis of open vs endovascular abdominal aortic aneurysm repair in a developing country: a 15-year experience at a tertiary medical center. *Annals of vascular surgery*, 2022.
- [33] Bakewell Robert, Krokidis Miltiadis, Winterbottom Andrew. Endovascular Abdominal Aortic Aneurysm Repair: Overview of Current Guidance, Strategies, and New Technologies, Perspectives from the United Kingdom. *Journal of Clinical Medicine*, 2022, 18(11).
- [34] Sailer A M, de Haan M W, Peppelenbosch A G, et al. CTA with Fluoroscopy Image Fusion Guidance in Endovascular Complex Aortic Aneurysm Repair. *European Journal of Vascular and Endovascular Surgery*, 2014, 47(4): 349–356.
- [35] Cai Fuyuan. Efficacy Analysis and Evaluation of In Situ Fenestration and Chimney Techniques in Reconstructing the Left Subclavian Artery in Stanford Type B Aortic Dissection. Fujian Medical University, 2021. DOI: 10.27020/d.cnki.gfjyu.2021.000856.
- [36] Nobre C, Oliveira-Santos M, Paiva L, et al. Fusion imaging in interventional cardiology. *Revista Portuguesa de Cardiologia*, 2020, 39(8): 463–473.
- [37] Wu C, Chen Q, Wang H, et al. A review of deep learning approaches for multimodal image segmentation of liver cancer. *Journal of Applied Clinical Medical Physics*, 2024, 25(12): e14540. DOI: 10.1002/acm2.14540. Epub 2024 Oct 7. PMID: 39374312; PMCID: PMC11633801.
- [38] Minami Y, Kudo M. Image Guidance in Ablation for Hepatocellular Carcinoma: Contrast-Enhanced Ultrasound and Fusion Imaging. *Frontiers in Oncology*, 2021, 11: 593636. DOI: 10.3389/fonc.2021.593636. PMID: 33747913; PMCID: PMC7973273.
- [39] Zhang Shuhan. Multimodal Medical Image Fusion Algorithm Based on Adaptive Iterative Least Squares Filtering and Multi-scale Decomposition. Jilin University, 2022. DOI: 10.27162/d.cnki.gjlin.2022.006181.
- [40] Eagleton M J. Updates in Endovascular Procedural Navigation. *Canadian Journal of Cardiology*, 2022, 38(5): 662–671.
- [41] Minelli F, Sica S, Salman F, et al. "Redo" 2D-3D Fusion Technique during Endovascular Redo Aortic Repair. *Diagnostics (Basel, Switzerland)*, 2023, 13(4): 635.
- [42] McNally M M, Scali S T, Feezor R J, et al. Three-dimensional fusion computed tomography decreases radiation exposure, procedure time, and contrast use during fenestrated endovascular aortic repair. *Journal of Vascular Surgery*, 2015, 61(2): 309–316.
- [43] Haga M, Shimizu T, Nishiyama A, et al. Three cases of fusion imaging in endovascular treatment of occlusive peripheral artery disease. *Journal of Vascular Surgery Cases and Innovative Techniques*, 2019, 5(4): 427–430.
- [44] D'Amore B, Smolinski-Zhao S, Daye D, et al. Role of Machine Learning and Artificial Intelligence in Interventional Oncology. *Current Oncology Reports*, 2021, 23(6): 1–8.
- [45] Maresch A C, Chacon M M, Markin N W. Left Atrial Appendage Occlusion Device Placement and the Integration of Echocardiography-Fluoroscopy Fusion Imaging. *Journal of Cardiothoracic and Vascular Anesthesia*, 2022, 36(1): 8–11.
- [46] Kang S-L, Armstrong A, Krings G, et al. Three-dimensional rotational angiography in congenital heart disease: Present status and evolving future. *Congenital Heart Disease*, 2019, 14(6): 1046–1057.

THE RELATIONSHIP BETWEEN GENE MUTATIONS AND PROGNOSIS IN PATIENTS WITH STAGE I NON-SMALL CELL LUNG CANCER AFTER SURGERY

Rui Ouyang, Ming Du*

Department of Cardiothoracic Surgery, The First Affiliated Hospital of Chongqing Medical University, Chongqing 400010, China.

Corresponding author: Ming Du, Email: ljdyt1103@sina.com

Abstract: This article discusses the relationship between gene mutations and prognosis in patients with stage I non-small cell lung cancer (NSCLC) after radical surgery. The study highlights that EGFR and ALK mutations are common in Stage I NSCLC patients and significantly affect both disease-free survival (DFS) and overall survival (OS). Patients with EGFR mutations respond well to EGFR-TKI treatment, significantly prolonging DFS; similarly, ALK mutation patients show improved prognosis with ALK inhibitor treatment. In contrast, patients with KRAS mutations have poorer outcomes, with common treatments including chemotherapy and immunotherapy. The importance of genetic testing in comprehensive postoperative treatment for early-stage NSCLC is highlighted, suggesting that individualized adjuvant therapy may play a role in improving long-term prognosis.

Keywords: Non-small cell lung cancer; Gene mutation; EGFR; ALK; KRAS; Prognosis; Targeted therapy

1 INTRODUCTION

Non-small cell lung cancer (NSCLC) accounts for approximately 85% of all lung cancer cases [1], with stage I NSCLC representing the earliest and most localized disease stage. The primary treatment for stage I NSCLC is surgical resection, followed by regular postoperative surveillance, which is the current standard approach. However, postoperative prognoses vary significantly, and some patients may experience recurrence or metastasis despite undergoing surgery. EGFR gene mutations and ALK gene fusions are common and clinically significant genetic alterations in NSCLC [2]. These mutations not only influence the biological behavior of tumors but also play a crucial role in determining patient prognosis. For patients with stage I NSCLC harboring specific genetic mutations, such as EGFR-positive mutations, the use of EGFR inhibitors (e.g., gefitinib or osimertinib) is recommended to reduce the risk of recurrence. Similarly, for ALK fusion-positive patients, ALK inhibitors (e.g., crizotinib or alectinib) are suggested as postoperative adjuvant therapy. The identification of these genetic mutations is critical for precision medicine. Genetic testing assists physicians in selecting the most appropriate treatment strategies, and targeted therapies can significantly improve survival outcomes, ultimately enhancing the treatment efficacy and survival rates of patients with stage I NSCLC.

2 COMMON GENE MUTATIONS IN STAGE I NSCLC

2.1 EGFR Mutations

Epidermal growth factor receptor (EGFR) gene mutations are the most common driver mutations in non-small cell lung cancer (NSCLC), particularly prevalent among Asian NSCLC patients, with an even higher incidence in non-smoking individuals, reaching 40% to 50%. The EGFR structure consists of an extracellular ligand-binding domain, a transmembrane domain, and a cytoplasmic domain, which contains a tyrosine kinase domain and sites for tyrosine autophosphorylation [3]. Upon binding with extracellular ligands, EGFR forms functionally active homodimers or heterodimers. The most common EGFR mutations include exon 19 deletions (exon-19del) and the L858R substitution mutation in exon 21 [4]. The exon-19del mutation shortens the β 3- α C helical structure, while the exon 21 L858R substitution locks the kinase domain into a constitutively active conformation [5], disrupting the inactive structure of EGFR and leading to dimerization and increased activity.

The presence of EGFR mutations is closely associated with tumor growth drivers, as these mutations result in abnormal activation of EGFR kinase activity, promoting tumor cell proliferation and survival. A study [6] analyzing genetic testing data from 254 NSCLC patients identified EGFR mutations in 132 cases, including 56 cases with exon 19 deletions and 76 cases with the exon 21 L858R substitution. Notably, the lymph node metastasis rate of patients with EGFR 19del and EGFR L858R mutations showed statistical significance. Targeted therapy with EGFR tyrosine kinase inhibitors (TKIs) has become the standard treatment for advanced EGFR-mutant NSCLC in recent years. The third-generation EGFR-TKI osimertinib has been validated in the ADAURA trial for use as postoperative adjuvant therapy in stage IB–IIIA NSCLC patients [7]. Other EGFR-TKIs, including first-generation inhibitors such as gefitinib and erlotinib, second-generation inhibitors such as afatinib and dacomitinib, and third-generation inhibitors such as almonertinib and furmonertinib, are currently undergoing various clinical trials.

2.2 KRAS Mutations

KRAS mutations are among the most common oncogenic alterations in non-small cell lung cancer (NSCLC), affecting approximately 20%–30% of patients [8]. These mutations are more frequently observed in smokers and lead to abnormal activation of cellular signaling pathways, promoting tumor growth and metastasis. KRAS-mutant patients typically do not respond well to targeted therapies and are associated with a poorer prognosis. A study [9] analyzing 69 NSCLC patients identified KRAS mutations in 13 cases, with the majority occurring in exon 2 and only one case in exon 3. The incidence of KRAS mutations was significantly correlated with gender, with male patients exhibiting a higher mutation rate than female patients. However, no significant associations were found between KRAS mutations and other factors such as patient age, histological subtype, smoking history, clinical TNM staging, tumor differentiation, or lymph node metastasis.

KRAS mutations exhibit high heterogeneity, and different KRAS mutation subtypes vary in their sensitivity to treatment, posing challenges for clinical management. Studies indicate that, compared to non-KRAS-mutant patients, those with KRAS mutations demonstrate better response rates and survival benefits when receiving monotherapy with immune checkpoint inhibitors. This may be due to alterations in the tumor immune microenvironment caused by KRAS mutations, making tumors more recognizable to the immune system. Combining immunotherapy with chemotherapy or other targeted therapies has been shown to significantly improve overall survival (OS) and progression-free survival (PFS) in NSCLC patients with KRAS mutations [10,11].

2.3 ALK Fusion

ALK gene rearrangement is a common genetic alteration in stage I non-small cell lung cancer (NSCLC), particularly prevalent among younger patients and non-smokers. The ALK gene is located on the short arm of human chromosome 2 (p23) and encodes the ALK receptor tyrosine kinase. Lung cancer with ALK fusion represents a distinct clinical subtype of NSCLC, with an incidence of approximately 2%–10% [12,13]. ALK fusion is associated with increased tumor aggressiveness and a higher risk of recurrence. A study [13] analyzed 735 early-stage NSCLC patients who underwent curative surgery and detected ALK fusion genes using fluorescence in situ hybridization (FISH). The results showed an overall ALK positivity rate of 3.8% (28/735), with rates of 6.8% in adenocarcinoma patients, 7.6% in female patients, and 8.9% in non-smokers. The median age of ALK-positive patients was 55 years, significantly lower than that of ALK-negative patients. Based on a median follow-up of 41.6 months, the overall survival (OS) of ALK-positive and ALK-negative patients was 97.7 months and 78.9 months, respectively, while the disease-free survival (DFS) was 76.4 months and 71.3 months, respectively, with no statistically significant difference. Additionally, ALK-positive patients tended to have a lower T-stage, predominantly classified as T1. Among adenocarcinoma patients, ALK-positive individuals had a higher level of lymph node metastasis, suggesting that despite their smaller tumor size, they exhibit a biological tendency for early lymph node spread.

Targeted therapies for ALK fusion, such as crizotinib, have been demonstrated to significantly reduce recurrence rates and improve survival outcomes [14]. ALK fusion can also coexist with other mutations, such as EGFR or KRAS, which may complicate the prognosis and therapeutic strategies for affected patients.

2.4 Other Mutations

In addition to common EGFR, KRAS, and ALK gene mutations, other genetic alterations such as ROS1, BRAF, and PIK3CA mutations are also present, though their incidence rates are relatively low. ROS1 fusion genes are predominantly found in younger non-smoking patients, whereas BRAF mutations are more commonly observed in smokers. Moreover, the specific type of BRAF mutation influences the choice of treatment strategy. PIK3CA mutations often coexist with other genetic alterations, and the presence of such co-mutations may affect patients' responses to targeted therapy as well as patterns of disease recurrence.

3 IMPACT OF GENE MUTATIONS ON THE PROGNOSIS OF POSTOPERATIVE STAGE I NSCLC

3.1 Survival Rate and Disease-Free Survival (DFS)

Research by Goldstraw et al. indicates that the 2-year and 5-year postoperative survival rates for stage I NSCLC (IA1, IA2, IA3, and IB) are 97%, 94%, 92%, and 89%, respectively, for 2 years, and 90%, 85%, 80%, and 73%, respectively, for 5 years [15] (Figure 1). Both EGFR and ALK mutations significantly impact the overall survival (OS) and disease-free survival (DFS) of stage I NSCLC patients. Studies have shown [17] that the application of EGFR-TKIs, such as osimertinib and erlotinib, in EGFR-mutant patients significantly reduces the risk of postoperative recurrence and prolongs DFS. Similarly, for patients with ALK fusion, ALK inhibitors such as crizotinib and alectinib have demonstrated remarkable efficacy as postoperative adjuvant therapies, leading to improved OS and DFS outcomes.

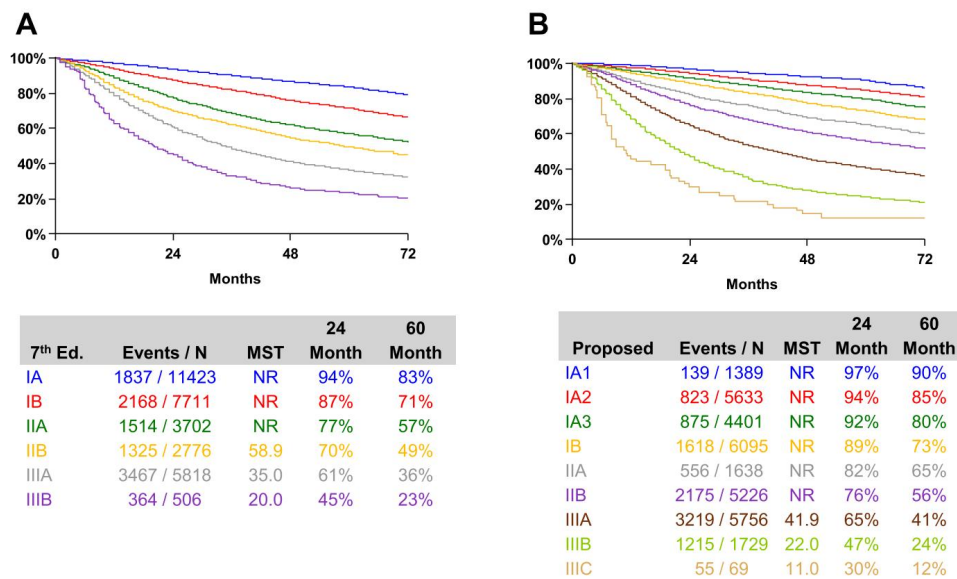


Figure 1 TNM Staging Classification Based on the 7th Edition (A) and Proposed 8th Edition (B). MST: Median Survival Time [15]

In contrast, patients with KRAS mutations tend to have a poorer prognosis [17], characterized by higher recurrence rates and shorter overall survival (OS). Unlike EGFR and ALK mutations, targeted therapies have shown limited effectiveness for KRAS-mutant patients, and the efficacy of chemotherapy is generally lower compared to patients with other genetic mutations[16]. The survival of KRAS-mutant NSCLC patients largely depends on the effectiveness of immunotherapy. While some patients experience significant survival benefits from immunotherapy, its overall efficacy remains limited.

3.2 Recurrence Risk and Patterns

Surgery is the most important treatment for stage I NSCLC; however, postoperative recurrence remains common. Existing literature reports that the recurrence rate after surgery for stage I NSCLC ranges from 14% to 36% [18,19]. Gene mutations also influence the recurrence patterns in stage I NSCLC patients. The primary recurrence and metastasis patterns for stage I NSCLC include local recurrence, regional recurrence, and distant metastasis. Studies show that the highest recurrence risk for 338 stage IA patients with postoperative recurrence of NSCLC occurs within 12 months after surgery [20]. This may be related to the immune homeostasis disruption caused by invasive surgery, with early metastasis patterns showing a distant metastasis rate of 14%–31%. Common metastatic sites include bone, the central nervous system, liver, and adrenal glands [21,22]. For EGFR-mutant NSCLC patients, adjuvant treatment with osimertinib for 3 years post-surgery has been shown to reduce the risk of recurrence or death by 83%–88%, significantly lowering the risk of both local and distant recurrence, including brain metastasis [7]. Additionally, patients with ALK fusion tend to experience distant metastasis, with common metastatic sites being the brain, liver, and bone. Early use of ALK inhibitors can significantly reduce the recurrence risk in these patients and effectively control tumor progression.

KRAS-mutant patients, however, often present with a pattern of both local recurrence and widespread systemic metastasis [23]. These patients typically experience local recurrence shortly after surgery, which gradually progresses into multi-system metastasis. Due to KRAS mutations' resistance to targeted therapies, treatment for these patients requires a multidisciplinary approach, combining chemotherapy, radiotherapy, and immunotherapy to prolong survival.

4 GENE MUTATIONS AND PERSONALIZED TREATMENT

4.1 Postoperative Treatment for EGFR and KRAS Mutant Patients

For stage I NSCLC patients with EGFR mutations, postoperative adjuvant EGFR-TKI treatment can significantly extend disease-free survival (DFS) [24]. The ADAURA study showed that osimertinib significantly reduced the risk of recurrence in patients with EGFR mutations in stages IB to IIIA of NSCLC. The use of postoperative adjuvant targeted therapy has made long-term disease-free survival after surgery a possibility for this group of patients. It is important to note that the use of EGFR-TKIs requires attention to the development of resistance, especially to secondary mutations like T790M that may emerge during long-term treatment.

For KRAS mutant patients, there is currently no effective targeted therapy, but immunotherapy is being gradually explored and may offer new options for these patients. KRAS G12C inhibitors, an emerging treatment approach, have

shown good results in some patients, though the overall efficacy still requires further clinical validation. For patients who are not suitable for immunotherapy, chemotherapy remains the primary postoperative treatment option.

4.2 Treatment Strategies for ALK and Other Mutations

For patients with ALK fusion, postoperative treatment with ALK inhibitors such as crizotinib or alectinib can significantly extend survival [13]. Especially in the early stages of postoperative adjuvant treatment, ALK inhibitors can effectively prevent tumor recurrence and reduce the risk of distant metastasis.

For other mutations, such as ROS1 fusion and BRAF mutations, targeted therapies are gradually becoming standard treatment options, improving patient prognosis. ROS1-positive patients typically respond well to crizotinib, while BRAF V600E mutation patients show favorable efficacy with BRAF inhibitors such as dabrafenib combined with trametinib. For these rare genetic mutations, the selection of targeted therapy should be based on specific genetic testing results and tailored to individualized treatment plans.

5 CONCLUSION

Gene mutations play a crucial role in the development and prognosis of stage I NSCLC. By detecting genes such as EGFR and ALK, it is possible to better predict patient prognosis and develop personalized treatment plans. Genetic testing is an important foundation for creating individualized treatment strategies, particularly in early detection and assessment of recurrence risk. In the future, personalized treatments based on genetic testing are expected to further improve survival rates and quality of life for stage I NSCLC patients. Moreover, with the continuous development of novel targeted therapies and immunotherapies, more patients will be able to benefit, thereby enhancing long-term disease-free survival.

CONFLICT OF INTEREST

The authors have no relevant financial or non-financial interests to disclose.

REFERENCES

- [1] Zhi X Y, Shi J G, Tian Y T, et al. Key points interpretation of the "2022 China Lung Cancer Patient Quality of Life White Paper". *Chinese Journal of Thoracic and Cardiovascular Surgery*, 2023, 30(08): 1083-1088.
- [2] Wang X M. Advances in research on VEGFR-targeted tumor drugs. *Biochemical Engineering*, 2019, 5(03): 121-124.
- [3] Herbst R S. Review of epidermal growth factor receptor biology. *Int J Radiat Oncol Biol Phys*, 2004, 59(2 Suppl): 21-26.
- [4] Lee C K, Wu Y L, Ding P N, et al. Impact of specific epidermal growth factor receptor (EGFR) mutations and clinical characteristics on outcomes after treatment with EGFR tyrosine kinase inhibitors versus chemotherapy in EGFR-mutant lung cancer: a meta-analysis. *J Clin Oncol*, 2015, 33(17): 1958-1965.
- [5] Reita D, Pabst L, Pencreach E, et al. Molecular mechanism of EGFR-TKI resistance in EGFR-mutated non-small cell lung cancer: application to biological diagnostics and monitoring. *Cancers*, 2021, 13(19): 4926.
- [6] Feng J X, Liu N, Qin X T, et al. Clinical pathological characteristics and lymph node metastasis risk factors of stage I-III non-small cell lung cancer. *Chinese Journal of Cancer Prevention and Treatment*, 2021, 28(16): 1226-1230. DOI: 10.16073/j.cnki.cjcp.2021.16.
- [7] Wu Y L, Tsuboi M, He J, et al. Osimertinib in resected EGFR-mutated non-small cell lung cancer. *N Engl J Med*, 2020, 383(18): 1711-1723.
- [8] Karachaliou N, Mayo C, Costa C, et al. KRAS mutations in lung cancer. *Clinical Lung Cancer*, 2013, 14(3): 205-214.
- [9] Ren B R, Zhu Y J, Wang G H, et al. Study on the correlation between KRAS gene mutation and the expression levels of ERCC1 and TYMS mRNA in stage I-III non-small cell lung cancer. *Modern Biomedical Progress*, 2016, 16(10): 1833-1837.
- [10] Gadgeel S, Rodriguez-Abreu D, Felip E, et al. LBA5-KRAS mutational status and efficacy in KEYNOTE-189: Pembrolizumab (pembro) plus chemotherapy (chemo) vs placebo plus chemo as first-line therapy for metastatic non-squamous NSCLC. *Ann Oncol*, 2019, 30, xi64-xi65.
- [11] West H J, McClelland M., Cappuzzo F, et al. Clinical efficacy of atezolizumab plus bevacizumab and chemotherapy in KRAS-mutated non-small cell lung cancer with STK11, KEAP1, or TP53 comutations: subgroup results from the phase III IMpower150 trial. *J Immunother Cancer*, 2022, 10(2).
- [12] Kong J, Yang X, Kong H, et al. EGFR and ALK driver gene analysis in 2394 patients with lung adenocarcinoma. *Journal of Nanjing Medical University (Natural Science Edition)*, 2020, 40(05): 675-680, 719.
- [13] Paik J H, Choi C M, Kim H, et al. Clinicopathologic implications of ALK rearrangement in surgically resected lung cancer: a proposal of diagnostic algorithm for ALK-rearranged adenocarcinoma. *Lung Cancer*, 2012, 76(3): 403-409.

- [14] National Health Commission of the People's Republic of China. Clinical application of respiratory system tumor drugs—2022 version of the new antitumor drug clinical application guidelines (Part 1). *Exploration of Rational Drug Use in China*, 2023, 20(4): 16-36.
- [15] Jonna S, Subramaniam D S. Molecular diagnostics and targeted therapies in non-small cell lung cancer (NSCLC): an update. *Discov Med*, 2019, 27(148): 167-170.
- [16] Pan Z C, Lin Y Z, Guo W C, et al. Meta-analysis comparing postoperative molecular targeted therapy and traditional chemotherapy in resectable non-small cell lung cancer patients. *Chinese Journal of Cancer Surgery*, 2020, 12(06): 560-563.
- [17] Yuan Y Q, Wei L, Fang N N. Gene mutation analysis in non-small cell lung cancer in the Aksu region. *Agricultural Reclamation Medicine*, 2022, 44(06): 503-507.
- [18] Goldstraw P, Chansky K, Crowley J, et al. The IASLC lung cancer staging project: proposals for revision of the TNM stage groupings in the forthcoming (eighth) edition of the TNM classification for lung cancer. *J Thorac Oncol*, 2016, 11(1): 39-51.
- [19] Wang C, Wu Y, Li J, et al. Distinct clinicopathologic factors and prognosis based on the presence of ground-glass opacity components in patients with resected stage I non-small cell lung cancer. *Ann Transl Med*, 2020, 8(18): 1133.
- [20] Mokhles S, Macbeth F, Treasure T, et al. Systematic lymphadenectomy versus sampling of ipsilateral mediastinal lymph-nodes during lobectomy for non-small-cell lung cancer: a systematic review of randomized trials and a meta-analysis. *Eur J Cardiothorac Surg*, 2017, 51(6): 1149-1156.
- [21] Palussière J, Chomy F, Savina M, et al. Radiofrequency ablation in stage IA non-small cell lung cancer in patients ineligible for surgery: results of a prospective multicenter phase II trial. *J Cardiothorac Surg*, 2018, 13(1): 91.
- [22] Klein C A. Cancer progression and the invisible phase of metastatic colonization I. *Nat Rev Cancer*, 2020, 20(11): 681-694.
- [23] Ziv E, Erinjeri J P, Yarmohammadi H, et al. The predictive value of KRAS gene mutation status in lung adenocarcinoma patients for local recurrence following image-guided ablation therapy. *International Journal of Medical Radiology*, 2017, 40(02): 213-214.
- [24] Kelly K, Altorki N K, Eberhardt W E E, et al. Adjuvant erlotinib versus placebo in patients with stage IB-III A non-small-cell lung cancer (RADIANT): a randomized, double-blind, phase III trial. *J Clin Oncol*, 2015, 33(34): 4007-4014.

THE PATHOLOGICAL PATHWAY FOR THE PERSISTENCE OF AD SYMPTOMS AFTER THE REMOVAL OF AMYLOID PLAQUES

JingHao Wang

University of Toronto Mississauga, ON L5L 1C6, Canada.

Corresponding Email: jinghaowang.utoronto@gmail.com

Abstract: Amyloid plaque has been an indicative hallmark for Alzheimer's diseases (AD), however the removal of which has shown to be inefficient in altering the progression of disease; thus, the study will focus on the mechanism behind the persistence of AD. The study examines the causal relationships among A β , neurofibrillary tangles (NFTs), cholinergic depletion, and excitotoxicity. Using secondary data from pre-existing studies, it is evidenced that A β causes cholinergic depletion, NFTs, and excitotoxicity through interacting with ChaT & nAChRs, IP3-K & GSK-3 β , and NR1 subunit on NMDAR respectively; NFTs causes cholinergic depletion and excitotoxicity through mitochondrial dysfunction, and interaction with vGLUT respectively; while excitotoxicity causes NFTs through interaction with cdk5 and PP2A. It is concluded that the persistence of AD after A β removal is due to a positive feedback loop mechanism between NFTs and excitotoxicity, which causes the persistence of NFTs, cholinergic depletion, and excitotoxicity. However, the principle causative agent of AD's progression remains undecidable.

Keywords: Cholinergic depletion; Excitotoxicity; NFTs; Amyloid plaque; Positive feedback mechanism

1 INTRODUCTION

1.1 Amyloid Plaque

AD is a type of dementia that is marked by high level of amyloid plaques in the brain. Amyloid precursor protein (APP) is a transmembrane protein, its functions in the central nervous system are not fully understood, but may be involved in facilitation of learning, neuron growth, cell adhesion, and various other neuronal activities [1]. APP undergoes proteolysis where it is cleaved into shorter fragments by protein secretases. In the amyloidogenic pathway, APP is initially cleaved by a β -secretase, to produce an intercellular APPs β fragment. The remaining protein in the membrane is further cleaved by γ secretase, producing intercellular amyloid β protein (A β Pa) and intracellular AICD [2]. In Alzheimer's disease, the concentration of A β in CNS is significantly higher than in healthy people. This excessive upregulation causes A β to aggregate and deposit in the brain, forming amyloid plaques, which has been the hallmark of Alzheimer's disease. Because of the prominent correlation between AD and plaques, a hypothesis was established in 1992, proposing that amyloid plaque is the causative agent of AD. However, 27 years later in 2019, a clinical trial reported on New England Journal of Medicine has made it clear that lowering the level of amyloid plaques does not ease AD, and in some patients the symptoms continued to get worse. This has raised a need for searching for another potential therapeutic target, as well as for a mechanism behind AD's persistence.

1.2 Pathological Processes in AD

Apart from amyloid plaques, there are various other processes associated with Alzheimer's disease, which are primarily neurofibrillary tangles (NFTs), neuroinflammation, excitotoxicity, and cholinergic depletion. NFTs are formed from tau proteins, which are proteins associated with microtubules in cytoskeleton of neuron, acting as a stabilizer maintaining the structure of microtubules. When tau proteins are hyperphosphorylated, they dissociate from microtubules and aggregate together, forming NFTs, which causes synapses loss, axonal transport impairment, and much more [3-4]. Neuroinflammation is the inflammation of nervous tissues, caused by abnormalities in astrocytes and glia cells, which secrete chemokines, cytokines, and other neuroinflammatory mediators in an irregular manner [5]. Excitotoxicity is neuronal degeneration caused by excessive stimulation of NMDA receptors [6]. Finally, cholinergic depletion is the loss of cholinergic activity, such as deficits in acetyltransferase [7]. These processes are all highly correlated with Alzheimer's disease, but the casual relationships among them remain little known.

1.3 Therapies for AD

Drugs have been developed for Alzheimer's disease until now, their intended therapeutic effect is one of two types; disease-controlling, meaning to suppress and stabilize the symptoms without being able to remove the root causative agent; and the other is disease-modifying, meaning to alter the progression and activity of the disease itself. However, most of them has failed to be effective, including those targeting A β , neuroinflammation, and tau protein. Out of all the drugs developed for AD until now, there are only four of them that are officially approved by FDA and can be prescribed to patients with mild and moderate AD. These drugs are donepezil, rivastigmine, galantamine, and

memantine, which all have a disease-controlling effect. Among these 4 drugs, donepezil, rivastigmine, and galantamine are all cholinesterase inhibitors, which lowers cholinergic depletion by inhibiting the breakdown of acetylcholine in the synaptic cleft. Memantine, on the other hand, is a NMDA receptor blocker, which lowers excitotoxicity. Furthermore, the efficacy of tau therapy has been uncertain. For example, lithium has an effect of inhibiting the protein kinase that phosphorylates tau protein, but short-term (10 weeks) lithium treatment on patients has shown no effect on improving the symptoms [8]. On the other hand, another drug called methylthioninium (MT), which is a tau aggregation inhibitor, has successfully demonstrated minor beneficial effects on AD over a period of 50 weeks [9]. Since there is variation in the effect of tau protein therapy, it is uncertain whether it is the causative agent of AD, thus it bears a high potential for successful disease-modifying effect.

1.4 Hypothesis

Since the inhibition of cholinergic depletion, excitotoxicity, and sometimes the tau proteins have a disease-controlling effect on patient, there is a certain level of dependence of AD symptoms on them. Therefore, the hypothesis states that cholinergic depletion, excitotoxicity, and tau protein are responsible for the persistence of AD after the removal of amyloid plaques through a particular pathological pathway, and the removal of which will terminate the persistence.

2 ASSUMPTIONS

2.1 Assumption 1

The initial accumulation of A β can begin years or even decades before the onset of dementia [10]; one study has shown that amyloid plaques can even be found in people in their early 20s [11]. On the other hand, it has been controversial regarding the time of occurrence of cholinergic depletion, some studies have suggested that it occurs before the symptomatic stage like amyloid plaques [12-14], and others suggest that it only occurs after the onset of dementia [15]. However, despite the controversy, there are only two possible scenarios; that cholinergic depletion either occurs after the onset of dementia or before the onset. In this paper, we assume that cholinergic depletion occurs before the onset of dementia. This is because if it occurred after the onset of symptoms, the interaction between amyloid plaques, NFTs, and cholinergic depletion would be extremely obscure because of the extensive time interval, which is 20 to 30 years [16], between the initiation of the two events, and the research of which would extend beyond the scope of this project.

2.2 Assumption 2

Since cholinergic depletion occurs before the onset of dementia, its severity is positively correlated with that of amyloid plaque one [12]. This gives rise to three possible scenarios regarding the interaction between amyloid plaques and cholinergic depletion; the first is that cholinergic depletion is the causative agent of amyloid plaque, the second is that amyloid plaque is the causative agent of cholinergic depletion, and the last one is that their relationship is not causal, but simply a correlation. In this paper, we assume that the second scenario is true, in which amyloid plaque is the causative agent of cholinergic depletion. This is because the first scenario, cholinergic depletion causes amyloid plaque, has already been a well-established hypothesis since 1980s [17], whereas the purpose of this paper is not to verify the cholinergic hypothesis. The third scenario implies that there is no interaction between amyloid plaques and cholinergic depletion, which is highly unlikely because it does not conform with the consensus in field of research. Therefore, the second scenario is adopted in this paper.

2.3 Assumption 3

The same assumption is made about NFTs, in which it occurs before the onset of dementia and is caused by amyloid plaques. This is because although it is almost certain that it occurs before dementia as indicated by numerous papers, it is somewhat controversial regarding the causal relationship between NFTs and amyloid plaques; that is, a tau hypothesis has been established, proposing that pathological tau is the causative agent of amyloid plaques [18]. On the other hand, no assumptions are made about excitotoxicity because it is almost certain that amyloid plaques cause excitotoxicity.

3 DATA ANALYSIS

To investigate the mechanism that sustains AD after the removal of amyloid plaques, the relationships among amyloid plaques, NFTs, cholinergic depletion and excitotoxicity will be analysed. This will be done in binary sets that contain two elements at the time, for example "A β and cholinergic depletion", "A β and NFTs", "A β and excitotoxicity", "NFTs and cholinergic depletion", and so on. The analysis will be accomplished by using secondary data from preexisting studies done by other researchers. At last, it should be noted that amyloid plaques is used interchangeably with A β , and NFTs is used interchangeably with tau. This is because they are mutually inclusive; one has to present if the other is present.

3.1 A β and Cholinergic Depletion

The mechanism by which A β causes cholinergic depletion is uncertain and has not reached a consensus. For example, a study using rat hippocampal slice has found that A β can reversibly inhibit the nicotinic acetylcholine receptor, blocking acetylcholine from opening the channel [19]. This suggests that high concentration of amyloid plaque in people with AD may cause chronic inhibition of nicotinic receptor. Another study using rat septal neuron culture has found that A β treatments reduce acetyltransferase activity, which is the enzyme responsible for the synthesis of acetylcholine [20]. Although the exact underlying mechanism is unknown, these studies provide two possibilities.

3.2 A β and NFTs

There are many proposed mechanisms regarding how A β causes NFTs, for example A β -IP3K-GSK-3 β pathway acts as a possibility. NFTs are formed from tau proteins that are abnormally hyperphosphorylated. There are various proteins that are responsible for the phosphorylation of tau, among them glycogen synthase kinase-3 β (GSK-3 β) is extensively studied, which could potentially act as a link between A β and NFTs. Another protein called phosphoinositide-3 kinase (PI-3K) acts as an inhibitory protein for GSK-3 β . This is concluded from a study using in vitro rat hippocampal neurons, where it is found that the inactivation of PI-3 by wortmannin treatments induces GSK-3 β activation [21]. The same study also showed that A β exposure inhibits PI-3 kinase activity just like wortmannin [21]. This suggests that abnormally high level of A β in AD patient can cause overactivation of GSK-3 β by chronically inhibiting IP3K kinase, which leads to hyperphosphorylation of tau proteins. Although this mechanism is proposed based on in vitro rat neurons, its validity in human is supported by another study that found significant increase in the level of GSK-3 β activity in AD patients [22]. Fundamentally, this serves as a possible mechanism underlying A β -NFTs relationship.

3.3 A β and Excitotoxicity

Excitotoxicity is defined as the overstimulation of NMDA receptors on the postsynaptic neuron, which causes damage to the neuron and is accompanied with excessive influx of calcium ions.

There are many studies shows that A β can bind directly to NMDA receptors to induce excitotoxicity. For example, a study using hippocampal neuron culture has found that amyloid oligomer can act as an agonist that binds NMDA receptors possibly at the extracellular Nterminal domain on the NR1 subunit and causes excessive influx of calcium ions [23]. The reason behind this idea is that in the experiment, an addition of 300 nM of amyloid oligomers to the cell culture induced a transient increase, about 3.5 folds, in the intracellular calcium level compared with the control. When an antibody that specifically blocks the N-terminal on NR1 is added to the culture in the presence of amyloid oligomer, the effect of amyloid oligomer is significantly reduced [23].

3.4 NFTs and Cholinergic Depletion

The action of tau oligomers has been demonstrated by numerous studies, and prominently, one of them is mitochondrial dysfunction. Mitochondria constantly undergo a cycle of fusion and fission in any given cell, where fission results fragments of mitochondria, and fusion results elongated mitochondria through the merging of fragments. These processes are collectively known as mitochondria dynamic, which is responsible for the size, morphology, function, and distribution of mitochondria [24]. DRP1 is a cytoplasmic protein that activates mitochondrial fission when it is translocated and incorporated to mitochondrial surface via mitochondrial receptors [24]; mitochondrial fission is inhibited when DRP1 activity is disrupted, resulting abnormally elongated mitochondria. Filamentous actin (F-actin) has a major role in mitochondrial dynamic. Although F-actin is commonly found in muscle cells, it also takes place in dendrites, where it acts as an important cytoskeletal component [25]. Study using fruit flies has found that increased F-actin stabilization (the increase in polymerization, bundling, and crosslinking of F-actin, resulting enlarged dendritic spine structure [26]) could cause mitochondrial elongation, where the DRP1 proteins failed to bind with mitochondrial surface [27-29]. Another study using fruit flies have shown that increasing the amount of tau could increase actin stabilization both in vitro and in vivo, and when tau are removed through immunodepletion, no actin stabilization was observed [30]. Combining the two experiments, since F-actin stabilization causes abnormal mitochondrial elongation, and tau proteins cause the stabilization of F-actin, therefore tau protein could indirectly cause abnormal mitochondrial elongation. To link mitochondrial elongation with cholinergic depletion, it should be noted that elongated mitochondria is a dysfunction [27]. Several studies have reported that mitochondrial dysfunction caused by tau could lead to reduction in mitochondria-dependent proteins, including pyruvate dehydrogenase [31]. Pyruvate dehydrogenase is an enzyme found inside the matrix of mitochondria; its primary function is to convert pyruvate into acetyl-coA. Acetyl-coA is needed in cytoplasm for the synthesis of acetylcholine, catalysed by acetyltransferase. In sum, it can be concluded that hyperphosphorylated tau proteins cause F-actin stabilization, which causes abnormally elongated mitochondria by disrupting the activity of DRP1, the dysfunctional mitochondria in turn produces less acetylcholine, causing cholinergic depletion. This pathway could act as a potential mechanism for the causal relationship between tau protein and cholinergic depletion.

3.5 NFTs and Excitotoxicity

Tau has been widely reported as the causative agent of excitotoxicity in AD, but the exact mechanism remains uncertain [32-35].

Several studies have been done demonstrating that pathological tau can cause excitotoxicity mediated by extrasynaptic NMDA receptors (NMDAR). One study using mice has shown that genetically induced pathological tau can cause overactivation of extrasynaptic NR2B-containing NMDAR. In the study, different receptor inhibitors were given to in vitro neuron cultures where NFTs are present, which are nifedipine (blocking L-type voltage-gated calcium channel), tetrodotoxin (blocking sodium channels), and so on. Out of all the drugs, only ifenprodil (blocking NR2B unit on NMDAR) has significantly reduced calcium influx. Since tau causes excess calcium influx, and only blocking extrasynaptic NR2B-containing NMDAR decreases the influx, it is concluded that the excitotoxicity by tau is mediated by extrasynaptic NR2B-containing NMDAR [32]; that the source of excess calcium influx is NR2B-containing NMDAR. The mechanism by which tau causes NR2B-containing NMDAR to be overactivated is through excessive glutamate. NR2B-containing NMDAR is activated by excess glutamate [36]. The same study has found that there is a significant increase in the level of extracellular glutamate (~45% relatively to control) when missorted tau is present in the slice culture [32]. In addition, another study using mouse model showed that missorted tau is correlated with a significant increase in vGLUT and a decrease in GLT-1 [37]. vGLUT is a transporter located on presynaptic neuron membrane that transports glutamate into neuron, while GLT-1 is located on nearby glia that removes glutamate from the extracellular space once glutamate is used [37]. In conclusion, pathological tau may cause excitotoxicity by increasing vGLUT and decreasing GLT-1, which increases extracellular glutamate level by decreasing its clearance; the excessive glutamate then overactivates extrasynaptic NR2B-containing NMDAR, causing excess influx of calcium.

3.6 Excitotoxicity and NFTs

The causal relationship between NFTs and excitotoxicity is likely to be bidirectional, where excitotoxicity can in turn cause the formation NFTs, forming a positive feedback loop. The study using kainic acid (KA) injection on mouse has demonstrated that glutamate-induced excitotoxicity can cause hyperphosphorylation of tau [38]. KA is an agonist that binds to kainite receptor, which is a glutamatergic receptor like NMDA and AMPA receptors. The KA injection in the experiment directly induces excitotoxicity [38]. The effect of KD injection on tau has two phases; the first phase (0-6 hours after KA injection) is marked with a short-term decrease in hyperphosphorylation of tau, and the second phase (6-10 hours after KA injection) involves rapid rephosphorylation of tau, where the phosphorylation level significantly exceeds the control [38]. The activities of protein kinase and phosphatase were monitored during the experiment, and it was concluded that the dephosphorylation of tau in the first phase is due to activation of PP2A (a phosphatase that dephosphorylates tau [39]), while the hyperphosphorylation in the second phase is due to activation of cdk5 (a kinase that phosphorylates tau [40]) and inhibition of PP2A [38]. On the other hand, the other kinases such as GSK-3 β , PKA, and CaMKII do not have much contribution to the two-phase changes of tau phosphorylation [38]. In summary, excitotoxicity mediated by glutamatergic receptor may cause the formation of NFTs by first activating PP2A to induce dephosphorylation of tau, and then activates cdk5 and inhibits PP2A to cause hyperphosphorylation of tau, which forms NFTs.

4. CONCLUSION AND DISCUSSION

4.1 Pathological Pathway

Summarizing the interaction between amyloid plaques, NFTs, cholinergic depletion, and excitotoxicity, a pathological pathway can be established (Figure 1); when amyloid is present, it acts as the upstream molecule whose primary role is to initiate all the downstream activities. In the downstream, it is likely that there is a positive feedback loop mechanism between the NFTs and excitotoxicity, where they amplify each other. If this was the case, even if amyloid plaques were removed from the brain, the activities of NFTs, excitotoxicity, and cholinergic depletion will still be maintained. However, it is still unknown which one of the activities is the principle causative agent; it could be any one of them or more than one.

4.2 Hypothesis Testing

To test the hypothesis, the amyloid plaques would have to be removed from the brain to isolate the downstream molecules. In other words, the procedure would have to be an extension of the clinical trial done in 2019 that falsified amyloid plaque cascade hypothesis. However, since human trials are time-consuming and costly, the removal of amyloid plaque can be done in animals. When amyloid plaques are removed, two conditions must be met in order for the pathological pathway to be true: 1. removing excitotoxicity causes subsequent elimination of both NFTs and cholinergic depletion, also accompanied by the termination of AD; 2. removing NFTs causes subsequent elimination of both excitotoxicity and cholinergic depletion, also accompanied by the termination of AD.

5. COUNTER-ARGUMENT

In the beginning, 3 assumptions were made. If either one of the assumptions is proved to be false, then the entire pathological pathway would be false. Even if the assumptions were true, the scope of this study is small, there are many other processes not taken into consideration, such as neuroinflammation, apolipoprotein gene, and so on. In addition, the molecules in the pathological pathways may have other actions which are not covered, for example there are studies

shown that GSK-3 β could interact with excitotoxicity, which would alter the pathological pathway if taken into consideration. Therefore, the possibility of hypothesis being true is extremely small, but it is never zero until experiment is carried out. The pathological pathway can be seen in Figure 1.

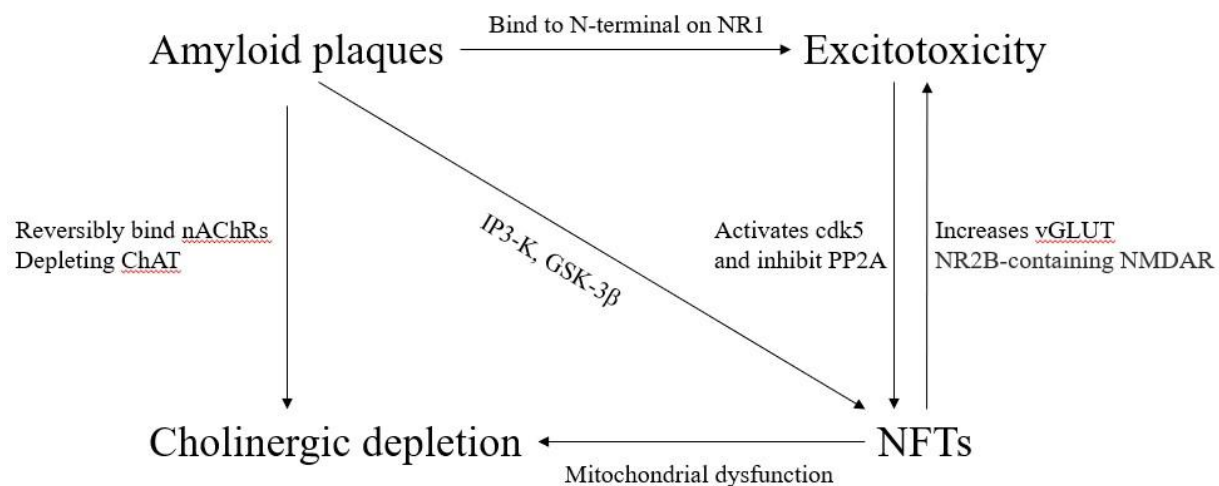


Figure 1 The Pathological Pathway

COMPETING INTERESTS

The authors have no relevant financial or non-financial interests to disclose.

REFERENCES

- [1] Puig K L, Combs C K. Expression and function of APP and its metabolites outside the central nervous system. *Experimental gerontology*, 2013, 48(7): 608-611.
- [2] O'Brien R J, Wong P C. Amyloid precursor protein processing and Alzheimer's disease. *Annual review of neuroscience*, 2011, 34: 185-204.
- [3] Frisoni G B. Biomarker trajectories across stages of Alzheimer disease. *Nature Reviews Neurology*, 2012, 8(6): 299-300.
- [4] Drubin D G, Kirschner M W. Tau protein function in living cells. *Journal of Cell Biology*, 1986, 103(6): 2739-2746.
- [5] Cong Y, Liang J, Gao Y, et al. Tau in Alzheimer's disease: Mechanisms and therapeutic strategies. *Current Alzheimer Research*, 2018, 15(3): 283-300.
- [6] Potter P E, Rauschkolb P K, Pandya Y, et al. Pre-and post-synaptic cortical cholinergic deficits are proportional to amyloid plaque presence and density at preclinical stages of Alzheimer's disease. *Acta neuropathologica*, 2011, 122(1): 49-60.
- [7] Bowen D M, Benton JS, Spillane JA, et al. Choline acetyltransferase activity and histopathology of frontal neocortex from biopsies of demented patients. *Journal of the neurological sciences*, 1982, 57(2-3): 191-202.
- [8] Heneka M T, O'Banion M K, Terwel D, et al. Neuroinflammatory processes in Alzheimer's disease. *Journal of neural transmission*, 2010, 117(8): 919-947.
- [9] Ong W-Y, Tanaka K, Dawe G S, et al. Slow excitotoxicity in Alzheimer's disease. *Journal of Alzheimer's Disease*, 2013, 35(4): 643-668.
- [10] Whitehouse P J. The cholinergic deficit in Alzheimer's disease. *The Journal of clinical psychiatry*, 1998.
- [11] Evin G, Kenche VB. BACE1 inhibitors: Current status and future directions in treating Alzheimer's disease. *Medicinal research reviews*, 2020, 40(1): 339-384.
- [12] Doody R S, Raman R, Farlow M, et al. A phase 3 trial of semagacestat for treatment of Alzheimer's disease. *New England Journal of Medicine*, 2013, 369(4): 341-350.
- [13] Egan M F, Kost J, Voss T, et al. Randomized trial of verubecestat for prodromal Alzheimer's disease. *New England Journal of Medicine*, 2019, 380(15): 1408-1420.
- [14] McGeer J, McGeer E, Rogers M A, et al. Nonsteroidal antiinflammatory drugs and the risk of Alzheimer's disease. *New England Journal of Medicine*, 2001, 345(21): 1515-1521.
- [15] Jordan F, Quinn T J, McGuinness B, et al. Aspirin, steroidal and nonsteroidal anti-inflammatory drugs for the treatment of Alzheimer's disease. *Cochrane Database of Systematic Reviews*, 2012, 2.
- [16] Stuve O, Weideman R A, McMahan DM, et al. Diclofenac reduces the risk of Alzheimer's disease: a pilot analysis of NSAIDs in two US veteran populations. *Therapeutic advances in neurological disorders*, 2020, 13: 1756286420935676.
- [17] Hampel H, Ewers M, Bürger K, et al. Lithium trial in Alzheimer's disease: a randomized, single-blind, placebo-controlled, multicenter 10-week study. *Journal of Clinical Psychiatry*, 2009, 70(6): 922.

- [18] Wischik C M, Seng C M, Seng S W, et al. Tau aggregation inhibitor therapy: an exploratory phase 2 study in mild or moderate Alzheimer's disease. *Journal of Alzheimer's Disease*, 2015, 44(2): 705-720.
- [19] Gonneaud J, Arenaza-Urquijo EM, Mezenge F, et al. Increased florbetapir binding in the temporal neocortex from age 20 to 60 years. *Neurology*, 2017, 89(24): 2438-2446.
- [20] Jansen W J, Gonneaud J, Kramer J, et al. Prevalence of cerebral amyloid pathology in persons without dementia: a metaanalysis. *Jama*, 2015, 313(19): 1924-1938.
- [21] Teipel S, Meindl S, Grinberg C. et al. Mild cognitive impairment in the elderly is associated with volume loss of the cholinergic basal forebrain region. *Biological psychiatry*, 2010, 67(6): 588-591.
- [22] Mazère J, Prunier C, Barret O, et al. In vivo SPECT imaging of vesicular acetylcholine transporter using [¹²³I]-IBVM in early Alzheimer's disease. *Neuroimage*, 2008, 40(1): 280-288.
- [23] Davis K L, Mohs R C, Marin D, et al. Cholinergic markers in elderly patients with early signs of Alzheimer disease. *Jama*, 1999, 281(15): 1401-1406.
- [24] Francis P T, Palmer A M, Snape M, et al. The cholinergic hypothesis of Alzheimer's disease: a review of progress. *Journal of Neurology, Neurosurgery & Psychiatry*, 1999, 66(2): 137-147.
- [25] Pettit D L, Shao Z, Yakel J L. β -Amyloid₁₋₄₂ peptide directly modulates nicotinic receptors in the rat hippocampal slice. *Journal of Neuroscience*, 2001, 21(1): RC120-RC120.
- [26] Pike C J, Burdick D, Walencewicz A J, et al. Neurodegeneration induced by beta-amyloid peptides in vitro: the role of peptide assembly state. *Journal of Neuroscience*, 1993, 13(4): 1676-1687.
- [27] Zheng W-H, Quirion R. Amyloid β peptide induces tau phosphorylation and loss of cholinergic neurons in rat primary septal cultures. *Neuroscience*, 2002, 115(1): 201-211.
- [28] Baudier J, Cole R D. Phosphorylation of tau proteins to a state like that in Alzheimer's brain is catalyzed by a calcium/calmodulin-dependent kinase and modulated by phospholipids. *Journal of Biological Chemistry*, 1987, 262(36): 17577-17583.
- [29] Takashima A, Noguchi K, Sato K, et al. Exposure of rat hippocampal neurons to amyloid β peptide (25-35) induces the inactivation of phosphatidylinositol-3 kinase and the activation of tau protein kinase I/glycogen synthase kinase-3 β . *Neuroscience letters*, 1996, 203(1): 33-36.
- [30] Leroy K, Yilmaz Z, Brion J-P. Increased level of active GSK-3 β in Alzheimer's disease and accumulation in argyrophilic grains and in neurons at different stages of neurofibrillary degeneration. *Neuropathology and applied neurobiology*, 2007, 33(1): 43-55.
- [31] Mattson M P, Cheng B, Davis D, et al. beta-Amyloid peptides destabilize calcium homeostasis and render human cortical neurons vulnerable to excitotoxicity. *Journal of Neuroscience*, 1992, 12(2): 376-389.
- [32] Arispe N, Diaz J C, Simakova O. A β ion channels. Prospects for treating Alzheimer's disease with A β channel blockers. *Biochimica et Biophysica Acta (BBA) Biomembranes*, 2007, 1768(8): 1952-1965.
- [33] De Felice F G, Velasco P T, Lambert M P, et al. A β oligomers induce neuronal oxidative stress through an N-methyl-D-aspartate receptor-dependent mechanism that is blocked by the Alzheimer drug memantine. *Journal of Biological Chemistry*, 2007, 282(15): 11590-11601.
- [34] Gerson J E, Castillo-Carranza D L, Kaye R. Advances in therapeutics for neurodegenerative tauopathies: moving toward the specific targeting of the most toxic tau species. *ACS chemical neuroscience*, 2014, 5(9): 752-769.
- [35] Shafiei S S, Guerrero-Muñoz M J, Castillo-Carranza D L. Tau oligomers: cytotoxicity, propagation, and mitochondrial damage. *Frontiers in aging neuroscience*, 2017, 9: 83.
- [36] Kametani F, Hasegawa M. Reconsideration of amyloid hypothesis and tau hypothesis in Alzheimer's disease. *Frontiers in neuroscience*, 2018, 12: 25.
- [37] Zhao J, Zhang J, Wang X. Regulation of mammalian mitochondrial dynamics: Opportunities and challenges. *Frontiers in Endocrinology*, 2020, 11.
- [38] Kim E. Postsynaptic Development: Neuronal Molecular Scaffolds. 2009: 817-824.
- [39] DuBoff B, Götz J, Feany M B. Tau promotes neurodegeneration via DRP1 mislocalization in vivo. *Neuron*, 2012, 75(4): 618-632.
- [40] Fulga T A, Rube D T, Yildirim F, et al. Abnormal bundling and accumulation of F-actin mediates tau-induced neuronal degeneration in vivo. *Nature cell biology*, 2007, 9(2): 139-148.

ACUPUNCTURE TREATMENT FOR SPINAL CORD INJURY: A RESEARCH BASED ON BIBLIOMETRICS AND DATA MINING

EnYan Xue^{1,2#}, JiQing Wang^{2,3#}, JingDong Gu^{1,2}, ShangJun Xia^{1,2}, Shuai Luo^{1,2}, Zheng Huang^{1*}

¹Guanghua Hospital Affiliated to Shanghai University of Traditional Chinese Medicine, Shanghai 20000, China.

²Shanghai University of Traditional Chinese Medicine, Shanghai 20000, China.

³Shanghai Municipal Hospital of Traditional Chinese Medicine, Shanghai 20000, China.

[#]These authors made equal contributed equally to this work and should be considered co-first authors.

Corresponding Author: Zheng Huang, Email: 13501772762@126.com

Abstract: Introduction: Acupuncture, as one of the alternative medical therapies for Spinal Cord Injury (SCI), offers various advantages. However, there is a significant diversity in research directions and acupoint selection for acupuncture treatment of SCI. This study aims to analyze the research directions and acupoint selection in acupuncture treatment for SCI through bibliometric methods and data mining techniques, exploring their characteristics and principles. Methods: This research commenced with a retrieval of literature on acupuncture treatment for SCI from the WOS database. Analysis was conducted using Citespace on authors, institutions, keywords, clustering, and timeline visuals. Moreover, association rule analysis, network analysis, and hierarchical cluster analysis were utilized to determine the correlations between different acupoints. Results: The results reveal a year-on-year increase in publications on acupuncture treatment for SCI, with research teams centered around Ding Ying and Guo Yi; leading research institutions include Kyung Hee University and Beijing University of Chinese Medicine. High-frequency keywords include "spinal cord injury" and "neuropathic pain," with a trend toward basic research. The most frequently used acupoints are ST36, EX-B2, SP6, GV14, and GV4; GV, ST, BL, GB are the four meridians with the most treatments; specific acupoints account for 51.72% of the total number of acupoints used, with the Five Shu Points being the most common; the back and lumbar regions are the most frequent acupoint areas used, followed by the upper limbs; ST36 and SP6, GV4 and GV14 are the most commonly used acupoint combinations, forming four clusters. Conclusion: This study analyzes and visualizes the current state and trends in acupuncture treatment for SCI, including the frequency of acupoint use, characteristics of acupoints, and combinations thereof. However, further expansion of data volume and clinical research is needed to validate the reliability and importance of these conclusions.

Keywords: Acupuncture treatment; Spinal cord injury; Data mining; Citespace

1 INTRODUCTION

Spinal Cord Injury (SCI) is a leading cause of death and disability globally, associated with severe neurological dysfunction and complications, including neuropathic pain, pressure ulcers, and urinary tract infections, affecting 930,000 patients worldwide each year, leading to irreversible sequelae and even permanent disability [1-4]. Over the past 30 years, the incidence of SCI has increased, with higher rates in men than in women, and in the elderly than in the young [5]. Current main clinical treatment strategies for SCI include surgery, pharmacotherapy, as well as behavioral, physical, and supportive therapies [6]. However, there are issues such as postoperative complications, drug side effects, and rehabilitation obstacles [7-9]. Due to potential complications [10], an increasing number of patients are choosing alternative medical therapies, such as acupuncture [11]. Evidence shows that acupuncture therapy offers advantages of being non-toxic, easy to operate, and low-cost, and is widely applied in clinical treatment of SCI [2, 12-14].

Citespace is a Java-based application that analyzes hotspots and research frontiers in a given knowledge domain over a certain period [15]. In this study, we aim to analyze the hotspots and research frontiers in acupuncture treatment for SCI using Citespace, which can aid our understanding of acupuncture's therapeutic effect on SCI.

The selection and combination of acupoints in acupuncture therapy play a crucial role in developing standardized clinical diagnosis and treatment plans. While many studies have evaluated the efficacy of acupuncture in treating SCI, it is challenging to ascertain the optimal selection and combination of acupoints due to the significant variation in prescriptions among these studies [12, 16]. The emergence of data mining technology offers a new effective method for analyzing acupuncture information. Data mining is the process of extracting potentially useful information and knowledge from large volumes of messy, imprecise random data in real applications [17]. Thus, this study aims to mine acupuncture prescriptions for treating SCI using data analysis and visualization software, to identify the characteristics and patterns of acupuncture treatment for SCI, which is important for future research and clinical practice.

2 METHODS

2.1 Search Strategy

From October 1983 to October 2023, four members searched the following five electronic databases: PubMed, Excerpta Medica Database (Embase), Web of Science Core Collection (WOS), Cochrane Library, Springer. The search strategy

combined keywords (a) “acupuncture” or “acupuncture therapy” and (b) “SCI” or “spinal cord injury”.

2.2 Study Selection Criteria

The inclusion criteria were as follows: (1) Types of literature included Randomized Controlled Trials (RCTs), Clinical Controlled Trials (CCTs), and animal studies; (2) Subjects of the literature were patients or animals diagnosed with Spinal Cord Injury (SCI); (3) Studies that used acupuncture therapy as the primary intervention, with complete prescriptions and detailed acupoint selections; (4) Acupuncture treatment addressing a series of complications arising from SCI.

Exclusion criteria included: (1) Reviews, systematic reviews, meta-analyses, commentaries, clinical guidelines; (2) Post-operative rehabilitation of SCI with acupuncture; (3) Treatments involving acupoints other than acupuncture; (4) Studies with incomplete or unspecified acupoint prescriptions; (5) Trials involving microsystem acupuncture, ear acupuncture, head acupuncture, wrist and ankle acupuncture, and other non-traditional body acupuncture practices, as they do not apply to conventional acupuncture theory; (6) SCI caused by acupuncture treatment.

Data collected were entered into Note Express 3.7, with titles, abstracts, and full texts of retrieved papers screened according to the inclusion and exclusion criteria to determine the suitable data. A predefined data extraction form was used to collate comprehensive data. Characteristics of the included studies covered acupoints, meridians, acupuncture methods, and acupoint combinations.

2.3 Data Processing

Initially, data retrieved from the Web of Science were filtered, standardized, and imported into Note Express 3.7 in "plain text" format for statistical analysis and elimination of duplicate documents. The standardized literature results were then exported in "Refworks-Citespace" format, named "download_WOS.txt," for subsequent analysis in CiteSpace6.1.R6. Furthermore, using pivot tables in Excel, the frequency of acupoints and meridians in SCI acupuncture prescriptions was summarized, and further analysis was conducted on the distribution of these acupoints across different body parts and the details of specific acupoints. To identify the most commonly used acupoint combinations, IBM SPSS Modeler 18.0 was utilized to discern correlations between different acupoints. Finally, as much data as possible was extracted from the qualifying studies, including results and acupuncture methods, and reanalyzed to obtain more information about acupuncture for SCI.

2.4 Data Analysis

The processed "download_WOS.txt" file was imported into Citespace, with settings adjusted for analysis: the time span was set from January 1995 to October 2023, with Time Slicing set to 1 year, the g-index option set to a k value of 25, Top N option set to 50, Pruning options set to Pathfinder and Pruning sliced networks, and Node Types set to Keyword, with all other settings default. This setup facilitated the creation of a keyword co-occurrence visualization, with node types set for authors and institutions, followed by K-means clustering analysis to generate keyword clusters and a timeline visual.

Data was then analyzed and visualized using IBM SPSS Modeler 18.0, assessing each acupoint's association strength, confidence, and lift. Support and confidence measures were used to gauge the strength of the acupoint association rules. Support is a metric indicating the probability of events A and B occurring together under certain conditions, reflecting the statistical significance of association rules within the entire dataset. Confidence signifies the likelihood of a subsequent event occurring given a premise, indicating the credibility of the association rule. In essence, support ($A \rightarrow B$) represents the percentage of prescriptions containing both acupoints A and B out of the total number of prescriptions; confidence ($A \rightarrow B$) shows the percentage of prescriptions containing both acupoints A and B out of the prescriptions that contain acupoint A. Lift indicates the relationship between the rule's confidence and the prior probability of the outcome occurring. Rules with a lift different from 1 are usually more interesting than those with a lift close to 1 [18]. Additionally, IBM SPSS Modeler was used to create a complex network display of the acupoint association rule matrix and the frequency of acupoint combinations in prescriptions.

Data processing and analysis, including visualization, were performed using RStudio. Data reading utilized the "read.transactions" function, with the "apriori" function for association rule analysis, "arules" for analyzing association rules, and the "arulesViz" package for visualization of association rules. The "NbClust," "parameters," and "factextra" functions were used to determine the number of clusters, with "ward.D" for distance calculation, and the "heatmap" and "pheatmap" functions for dendrogram and heatmap analysis [19, 20].

3 RESULTS

3.1 Analysis of Web of Science Data

3.1.1 Annual publication volume

Analysis of 308 documents collected from the Web of Science and imported into Citespace showed an overall upward

trend in publication volume (Figure 1). From 1995 to 2003, there was a steady increase in publications, followed by a decline between 2003 and 2005 before rising again until 2009. Years 2010-2011, 2013-2014, and 2019-2020 showed declining trends, while other years experienced growth. A downward trend in 2023 was observed, attributed to incomplete data inclusion for the year.

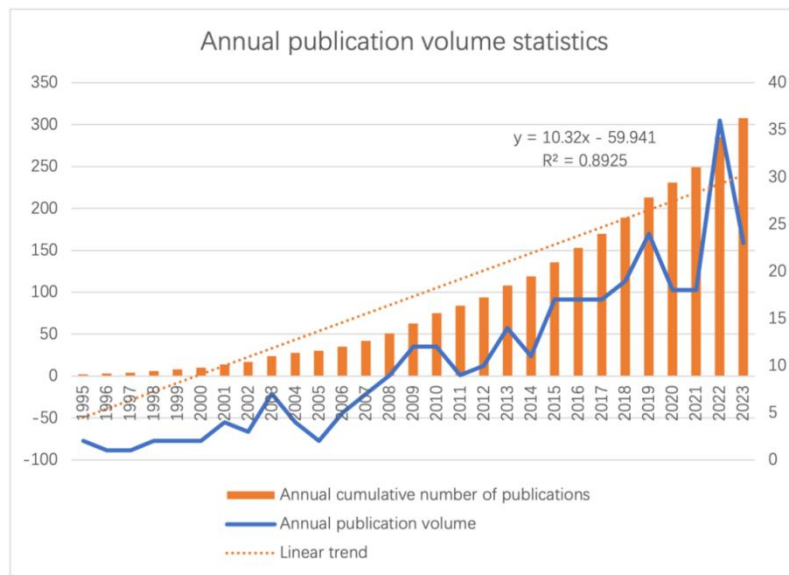


Figure 1 Line Chart of Annual Publication Volume for Acupuncture Treatment of Spinal Cord Injury

3.1.2 Author statistics

The analysis of authors included in the literature revealed collaboration networks as seen in Figure 2, with 589 nodes and 1058 links, and a network density of 0.0061. This formed multiple research teams centered around core individuals like Ding Ying and Guo Yi, showing close intra-team collaboration. Ding Ying was the most prolific author with 9 publications. There were 23 authors with more than 3 publications, totaling 86 publications, accounting for 27.92% of the total, indicating the need to expand the core group of authors and improve publication output. The top 10 authors are listed in Table 1.



Figure 2 Author Collaboration Network Map in Acupuncture Treatment of Spinal Cord Injury Research Literature (Nodes represent authors, with larger nodes indicating more publications; lines between nodes indicate collaborative relationships between authors, with more lines indicating closer collaboration.)

Table 1 Top 10 Authors by Publication Volume on Acupuncture Treatment for Spinal Cord Injury

Number	Author	Number of publications	Starting publication time
1	Ding, Ying	9	2009
2	Guo, Yi	6	2013
3	Wang, Ting-Hua	6	2007
4	Chen, Bo	4	2019
5	Jiang, Song-He	4	2014
6	Fan, Wen	4	2020
7	Gong, Yinan	4	2020
8	Wu, Yaochi	4	2017
9	Li, Ningcen	3	2021

3.1.3 Institution statistics

Analysis of institutions involved in the included literature, depicted in the institutional collaboration network seen in Figure 3, showed 344 nodes and 469 links, with a network density of 0.0079. This indicates that 344 institutions are researching acupuncture treatment for spinal cord injuries, with low network density suggesting limited collaboration between them. The top five publishing institutions were Kyung Hee Univ (14 publications), Beijing Univ Chinese Med (12 publications), Sun Yat Sen Univ (10 publications), Shanghai Jiao Tong Univ (10 publications), and China Acad Chinese Med Sci (10 publications).



Figure 3 Institutional Collaboration Network Map in Acupuncture Treatment of Spinal Cord Injury Research (Nodes represent institutions, with node size indicating the volume of publications; lines represent collaborative relationships between institutions.)

3.1.4 Keyword statistics

(1) Keyword Co-occurrence Analysis

The analysis included 503 keywords, with 503 nodes and 2645 links, showing a network density of 0.0209 (Figure 4). "Neuropathic pain" and "expression" were among the high-frequency keywords related to SCI symptoms. The top ten high-frequency keywords are listed in Table 2.

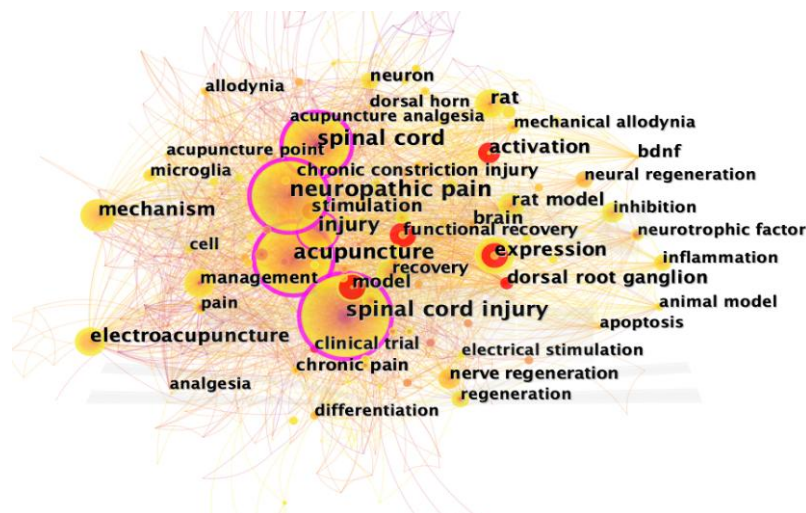


Figure 4 Keyword Co-occurrence Analysis Map in Acupuncture Treatment of Spinal Cord Injury Research Literature (Nodes represent keywords, with larger nodes indicating higher frequency of occurrence; lines represent co-occurrence relationships, with the closeness of relationships indicated by the number of lines, and colors transitioning from red to yellow indicating from more recent to older.)

Table 2 High-Frequency Keywords in Acupuncture Treatment for Spinal Cord Injury Research Literature (Top 10)

Number	Keywords	Centrality	Frequency
1	spinal cord injury	0.34	110
2	acupuncture	0.23	90

3	neuropathic pain	0.34	69
4	spinal cord	0.23	53
5	expression	0.07	40
6	injury	0.16	31
7	mechanism	0.09	29
8	activation	0.08	27
9	electroacupuncture	0.09	26
10	model	0.03	21

(2) Keyword Clustering

Keywords within the same cluster have strong relevancy, forming 11 clusters representing different research domains in acupuncture treatment for SCI (Figure 5). The clustering quality metrics, with a modularity Q value of 0.4805 and a silhouette S value of 0.7776, indicate a reasonable clustering structure [21]. The clusters are categorized into 1) SCI mechanisms, 2) literature types, 3) SCI-related symptoms, and 4) acupuncture prescriptions.

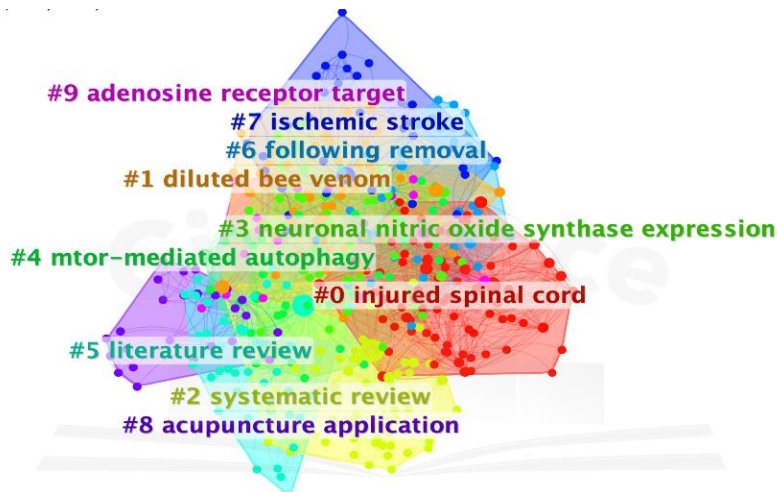


Figure 5 Keyword Clustering Analysis Map in Acupuncture Treatment of Spinal Cord Injury Research Literature (Different color blocks represent different clusters, with nodes within a block representing keywords in that cluster; smaller cluster numbers indicate larger cluster sizes.)

(3) Keyword Timeline Visualization

This visualizes the research focus over time, with high-frequency keywords before 2000 including "neuropathic pain," "spinal cord injury," and "acupuncture," shifting towards "electroacupuncture," "expression," and "model" after 2000, indicating a research focus on specific therapies and mechanisms (Figure 6).

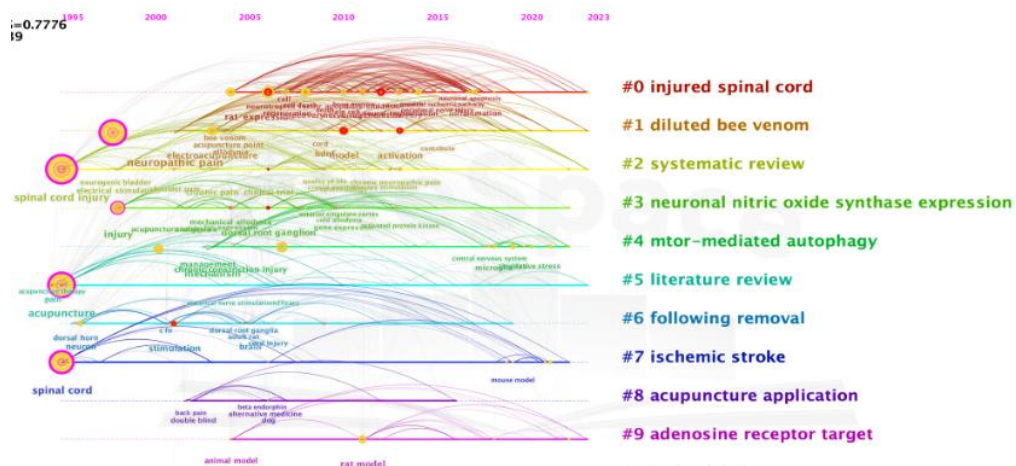


Figure 6 Timeline Map of Acupuncture Treatment for Spinal Cord Injury Research Literature (Y-axis nodes represent the year keywords first appeared, with node size indicating frequency of occurrence; smaller cluster numbers indicate larger cluster sizes.)

3.2 Acupuncture Prescription Findings and Overview

In five databases, 949 articles were found and imported into Note Express 3.7 for selection. After exclusion criteria were applied, 373 documents were included for further analysis (Figure 7).

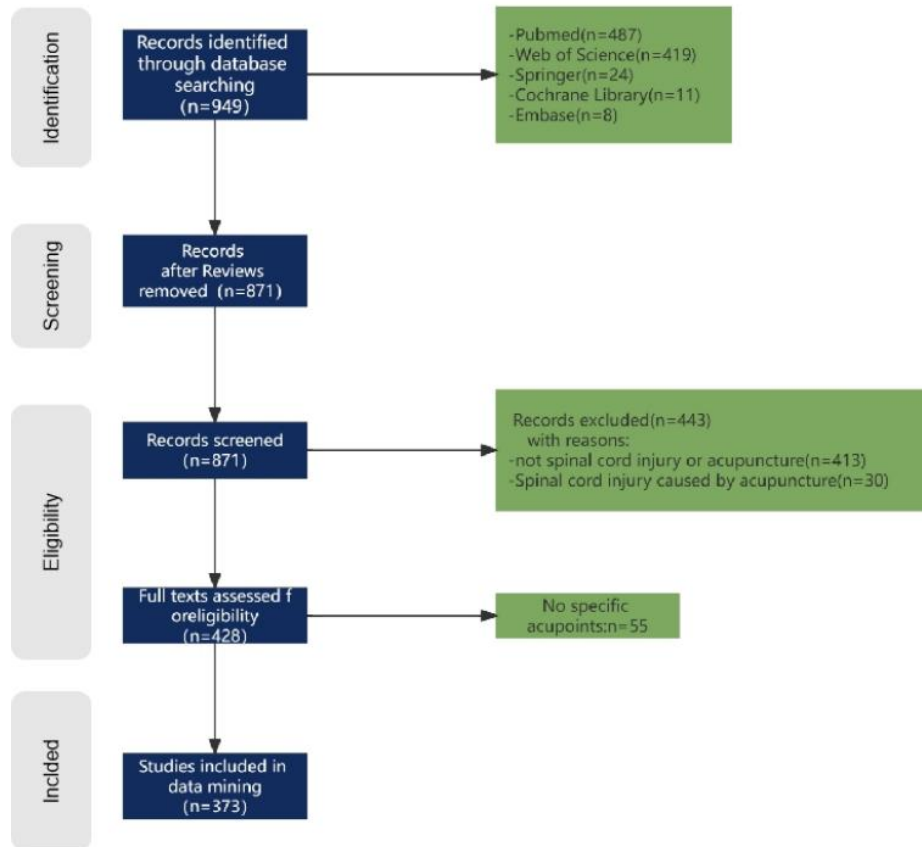


Figure 7 Literature Screening Process for Acupuncture Treatment of SCI

3.2.1 Application of acupoints

Among 368 prescriptions, 84 meridian acupoints and 3 extra-meridian points were recorded 959 times. Table 3 lists the 20 most commonly used acupoints, with ST36, EX-B2, SP6, GV14, and GV4 being the top five (Figure 8).

Table 3 The Top Twenty Acupoints for SCI Treatment

Number	Acupoints	Frequency	Proportion(%)
1	ST36	132	13.75
2	EX-B2	65	6.77
3	SP6	61	6.35
4	GV14	61	6.35
5	GV4	52	5.42
6	GB30	40	4.17
7	GB34	39	4.06
8	GV6	39	4.06
9	BL32	36	3.75
10	GV9	35	3.65
11	BL40	20	2.08
12	GB39	20	2.08
13	BL54	19	1.98
14	ST32	19	1.98
15	CV3	18	1.88
16	GV2	17	1.77
17	CV4	16	1.67
18	ST28	16	1.67
19	BL33	16	1.67
20	GV3	15	1.56

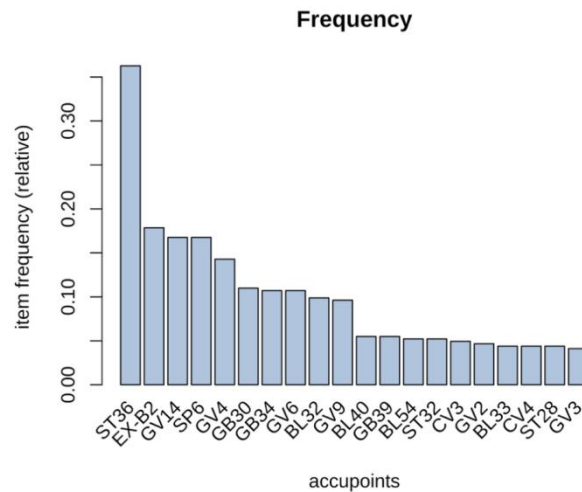


Figure 8 Frequency Chart of High-Frequency Acupoints for SCI

3.2.2 Application of meridians and acupoints

Analysis revealed 87 acupoints used for treating SCI, distributed among the 14 meridians (12 main meridians, GV, CV) and 3 extras. Table 4 shows the frequency and proportion of each meridian used, with GV, ST, BL, GB being the most frequently used meridians. In terms of yin-yang balance, yang meridian acupoints accounted for 72.61%, and yin meridian acupoints for 27.38%.

Table 4 Association Analysis of Meridians and Acupoints Used in SCI Treatment

Number	Meridian	Frequency	Proportion (%)*	Acupoints in Each Meridian		
				Number	Proportion (%)#	Acupoints (Frequency)
1	GV	262	27.29	12	13.79	GV14(61),GV4(52),GV6(39),GV9(35),GV2(17),GV3(15),GV1(14),GV20(12),GV26(9),GV16(5),GV12(2),GV29(1)
2	ST	176	18.33	6	6.90	ST36(132),ST32(19),ST28(16),ST25(7),ST41(1),ST40(1)
3	BL	146	15.21	19	21.84	BL32(36),BL40(20),BL54(19),BL33(16),BL23(13),BL34(9),BL31(8),BL60(5),BL20(4),BL62(3),BL28(3),BL35(2),BL13(2),BL15(1),BL21(1),BL24(1),BL59(1),BL11(1),BL57(1)
4	GB	101	10.52	5	5.75	GB30(40),GB34(39),GB39(20),GB21(1),GB20(1)
5	EX	69	7.19	3	3.45	EX-B2(65),EX-UE9(2),EX-LE10(2)
6	SP	65	6.77	2	2.30	SP6(61),SP9(4)
7	CV	54	5.63	7	8.05	CV3(18),CV4(16),CV6(11),CV12(4),CV8(2),CV2(2),CV17(1)
8	LI	25	2.60	5	5.75	LI4(14),LI11(7),LI10(2),LI16(1),LI14(1)
9	SI	14	1.46	9	10.34	SI3(6),SI4(1),SI11(1),SI13(1),SI10(1),SI15(1),SI9(1),SI14(1),SI12(1)
10	SJ	11	1.15	5	5.75	SJ2(4),SJ14(3),SJ5(2),SJ6(1),SJ15(1)
11	KI	10	1.04	1	1.15	KI3(10)
12	PC	10	1.04	4	4.60	PC6(6),PC5(2),PC2(1),PC7(1)
13	LR	6	0.63	1	1.15	LR3(6)
14	HT	6	0.63	4	4.60	HT7(2),HT3(2),HT8(1),HT1(1)
15	LU	5	0.52	4	4.60	LU7(2),LU1(1),LU2(1),LU10(1)

3.2.3 Application of specific acupoints

Of the 87 acupoints used, 45 were specific, constituting 51.72% of the total. The most commonly used specific acupoints were the Five-shu points (31.1%), followed by Lower he-sea points, EX, and Front-mu points for treating SCI (Table 5).

Table 5 Association Analysis of Specific Acupoints Used in SCI Treatment

Number	Specific Acupoints	Frequency	Proportion (%)*	Acupoints in Each Specific Acupoints		
				Amount of Acupoints	Proportion (%)#	Acupoints (Frequency)
1	Five-shu points	225	38.66	14	31.1	ST36(132),GB34(39),BL40(20),LI11(7),SI3(6),BL60(5),SP9(4),SJ2(4),HT7(2),HT3(2),PC(2),LU10(1),HT8(1),ST41(1)
2	Lower he-sea points	152	26.12	2	4.44	ST36(132),BL40(20)
3	EX	69	11.86	3	6.67	EX-B2(65),EX-UE9(2),EX-LE10(2)
4	Front-mu points	35	6.01	3	6.67	CV3(18),CV4(16),LU1(1)
5	Yuan-primary points	32	5.50	5	11.11	LI4(14),KI3(10),LR3(6),SI4(1),PC7(1)
6	Eight-influent points	25	4.30	3	6.67	GB39(20),CV12(4),BL11(1)
7	Back-shu points	24	4.12	6	13.33	BL23(13),BL20(4),BL28(3),BL13(2),BL15(1),BL21(1)
8	Eight-confluent points	14	2.41	5	11.11	SI3(6),BL62(3),SJ5(2),LU7(2),SI10(1)
8	Luo-connecting points	5	0.86	3	6.67	SJ5(2),LU7(2),ST40(1)
9	Xi-cleft points	1	0.17	1	2.22	BL59(1)

3.2.4 Application of acupoints on different body parts

We analyzed the distribution of acupoints in acupuncture prescriptions. Table 6 displays the frequency and percentage of acupoint distribution, along with the names and frequencies of the acupoints. The back and lumbar area had the highest frequency of acupoint usage (43.65%), with 26 acupoints used 419 times. The upper limbs were the body part with the most acupoints used (7.08%), with 27 acupoints used 68 times.

Table 6 Association Analysis of Body Parts and Acupoints Used in SCI Treatment

Body Part	Frequency	Proportion (%)*	Acupoints in Each Body Part		
			Amount of Acupoints	Proportion (%)#	Acupoints (Frequency)
Back and lumbar	419	43.65	26	29.89	EX-B2(65),GV14(61),GV4(52),GV6(39),GV9(35),BL32(36),BL54(19),GV2(17),BL33(16),GV3(15),GV1(14),BL23(13),BL34(9),BL31(8),BL20(4),BL28(3),GV12(2),BL35(2),BL13(2),BL15(1),BL21(1),SI11(1),BL24(1),SI15(1),SI14(1),BL11(1),ST36(132),SP6(61),GB30(40),GB34(39),GB39(20),BL40(20),ST32(19),KI3(10),LR3(6),BL60(5),SP9(4),BL62(3),EX-LE10(2),ST41(1),BL59(1),ST40(1),BL57(1)
Lower limbs	365	38.02	17	19.54	ST36(132),SP6(61),GB30(40),GB34(39),GB39(20),BL40(20),ST32(19),KI3(10),LR3(6),BL60(5),SP9(4),BL62(3),EX-LE10(2),ST41(1),BL59(1),ST40(1),BL57(1)
Chest and abdomen	80	8.33	12	13.79	CV3(18),ST28(16),CV4(16),CV6(11),ST25(7),CV12(4),CV8(2),CV2(2),LU1(1),LU2(1),PC2(1),CV17(1)
Upper limbs	68	7.08	27	31.03	LI4(14),LI11(7),PC6(6),SI3(6),SJ2(4),SJ14(3),SJ5(2),LI10(2),HT7(2),HT3(2),LU7(2),PC5(2),EX-UE9(2),SJ6(1),LU10(1),SI4(1),SJ15(1),HT8(1),SI13(1),SI10(1),LI16(1),SI9(1),GB21(1),HT1(1),PC7(1),SI12(1),LI14(1)
Head, face, and neck	28	2.92	5	5.75	GV20(12),GV26(9),GV16(5),GV29(1),GB20(1)

3.2.5 SCI high-frequency acupoints-specific points-body parts chord diagram

We selected the top ten acupoints by frequency, along with related specific acupoint attributes and body part distributions, to create an SCI high-frequency acupoints-specific points-body parts chord diagram (Figure 9) using the Microbio platform.

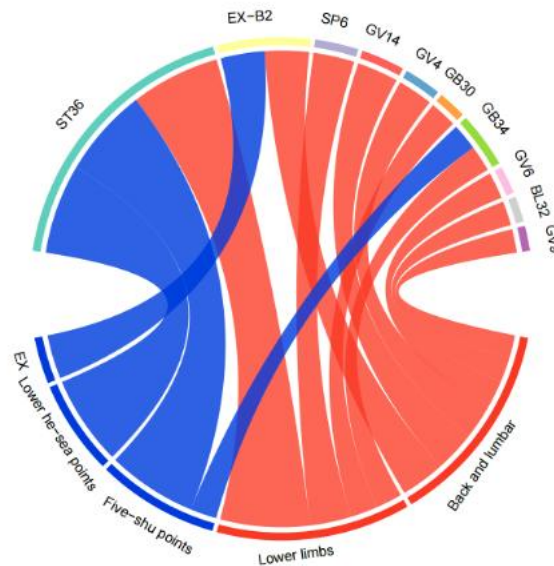


Figure 9 Chord Diagram of High-Frequency Acupoints with Specific Points and Body Parts

3.2.6 SCI acupoint combination rules

Table 7 summarizes the top 10 acupoint combinations in SCI acupuncture prescriptions by support. The top three combinations by support were ST36 with SP6, GV4 with GV14, and GV14 with GV4, consistent with the association rules matrix visualization. The primary combination was ST36 with SP6, which had the highest support of 17.64% and a confidence of 73.40%. We then generated association rule scatter plots and network diagrams using the "plot" function in R and created complex network diagrams of acupoint combinations using IBM SPSS Modeler18.0 (Figure 10-12).

Table 7 The Top Ten Acupoint Combinations in SCI Treatment

Number	Combination of Acupoints	Support (%)	Confidence (%)	Lift
1	ST36 → SP6	17.64	73.40	2.12
2	GV4 → GV14	15.76	69.05	5.18
3	GV14 → GV4	13.32	81.69	5.18
4	ST36 → GB34	10.88	68.97	1.99
5	GV9 → GV6	9.76	88.46	9.82
6	GV6 → GV9	9.01	95.83	16.32
7	ST28 → BL54	5.25	64.29	16.92
8	ST32 → GB39, ST36	5.25	85.71	5.47
9	SP6 → GB39, ST36	5.25	96.43	2.88
10	GB30 → BL40	5.07	70.37	16.92

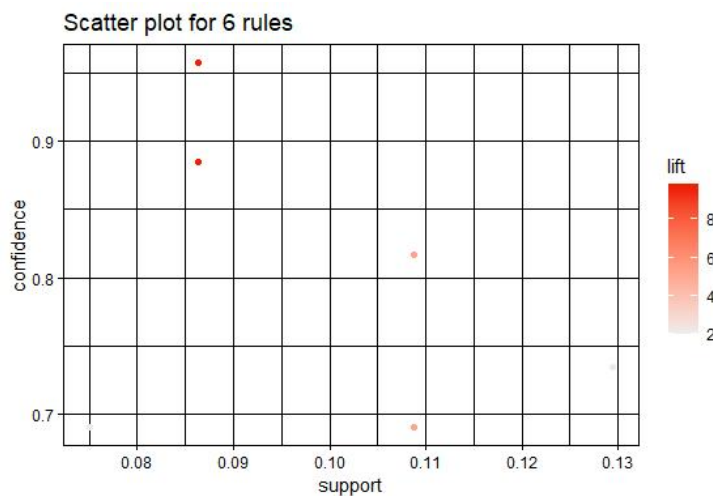


Figure 10 Scatter Plot of Association Rules

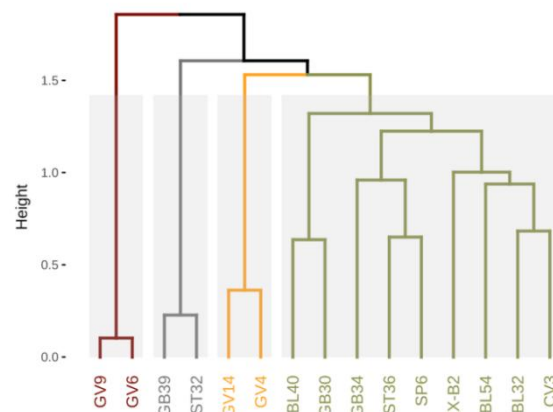


Figure 13 Dendrogram of Acupoint Clustering in Acupuncture Treatment for SCI

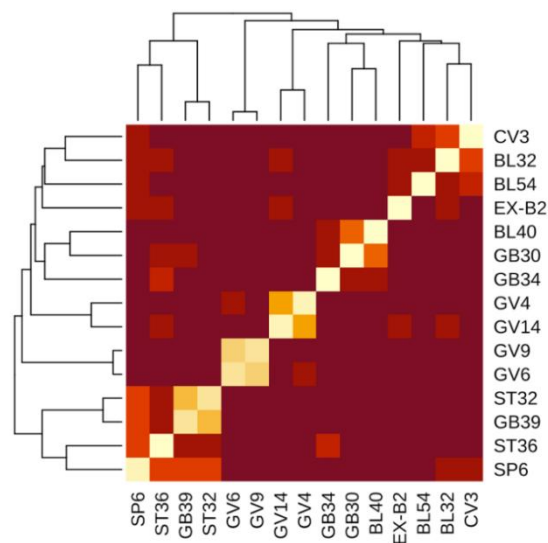


Figure 14 Heatmap of Acupoint Clustering in Acupuncture Treatment for SCI

4 DISCUSSION

Spinal cord injury causes neurological dysfunction in patients, with severe cases leading to paralysis of the lower limbs [22]. The remodeling and integrity of neural circuits are crucial for the functional recovery of the spinal cord [23]. Dysfunction in neural circuits following SCI is primarily due to axonal breakage and neuronal death. Therefore, the plasticity of neural circuits is the basis for neurological function recovery. Current treatments mainly focus on promoting the regeneration and extension of the corticospinal tract (CST) to re-establish connections with distal neurons [24]. Additionally, reducing adverse factors in the microenvironment that affect neural regeneration, such as glial scarring [25] and neuroinflammation [26], is critically important.

Acupuncture, as an essential part of Traditional Chinese Medicine, has been widely applied in neurological diseases and serves as a significant non-surgical alternative and adjunct therapy for SCI [27]. The efficacy of acupuncture in the treatment of SCI has been confirmed in numerous studies [28]. Research indicates that acupuncture can promote the survival and synaptic plasticity of hippocampal neurons [29]. Electroacupuncture has been shown to induce the synthesis and secretion of endogenous neurotrophic factors in spinal cord cells in SCI, creating a favorable microenvironment for neuronal survival and axonal regeneration [30]. Furthermore, acupuncture inhibits the activation of astrocytes and microglia following SCI [31-32], preventing the formation of glial scars and the occurrence of neuroinflammation, thus removing adverse factors for neural regeneration.

This study first utilized Citespace software to visually analyze literature related to acupuncture treatment for SCI in the Web of Science. The results indicate a stable upward trend in overall publication trends, with significant contributions from teams led by Ding Ying and Guo Yi. There is close cooperation within research teams but less between teams. Before 2000, the focus was on general research on SCI, shifting towards basic research and specific mechanisms from 2000 onwards. From the collaboration network diagram of research institutions, China dominates, but there is insufficient cooperation among institutions. Research institutions should establish connections, enhance result exchange, and further deepen the field of acupuncture treatment for SCI. High-frequency keywords and clusters in the field of acupuncture treatment for SCI involve adenosine receptor targets, mtor-mediated autophagy, neuropathic pain, etc.

Respiratory complications common in SCI patients negatively impact quality of life. Adenosine receptor antagonists can induce the recovery of diaphragm function after rat SCI [33]. Research by Zhou et al [34], suggests that autophagy flux impairment induced by SCI leads to neuronal death. Neuropathic pain following SCI is a complex condition, with its definition, manifestations, and related treatments under extensive study [35, 36].

In terms of acupoint frequency, acupuncture treatment for Spinal Cord Injury most commonly utilizes ST36, EX-B2, SP6, GV14, and GV4. ST36 is associated with the stomach meridian, serving as a crucial point for harmonizing the stomach and as a lower he-sea point. EX-B2, an extra-meridian point adjacent to GV, is known for its efficacy in activating blood circulation, removing stasis, and relieving pain [37]. SP6, often used in conjunction with ST36, is instrumental in nourishing qi and blood, playing a vital role in improving the local microenvironment for SCI treatment [38]. Acupuncture at GV14 and GV4 directly benefits by warming yang, invigorating the governing vessel, strengthening the kidneys, and nourishing qi and blood [39].

From the perspective of meridian distribution, GV, ST, and BL are predominantly chosen for treating SCI. GV acts as the sea of yang meridians, governing the body's yang qi, distributed to the trunk and limbs. In SCI, when GV is compromised, it leads to qi and blood stagnation, yang qi obstruction, and malnourishment of muscles and tendons. Thus, dredging GV and facilitating the flow of yang qi are key to treating SCI [40]. The "Huang Di Nei Jing Su Wen" mentions that treating flaccidity involves primarily selecting yangming, with the stomach meridian being the sea of the five zang and six fu organs. Its harmonization ensures the smooth flow of qi and blood, nourishment of organs, and relaxation of tendons and ligaments [41]. The thoracic and lumbar spine, warmed by the qi of the foot taiyang bladder meridian, shows signs of neurogenic bladder and urinary incontinence when the bladder meridian is impaired [2].

In acupuncture treatment for SCI, specific acupoints such as Five-shu points, Lower he-sea points, and EX play a dominant role. "Ling Shu: The Nine Needles and Twelve Source Points" states that the transformation and regulation of bladder qi depend on the harmony of the Five-shu points [42]. Among the Lower he-sea points, ST36, as the lower he-sea point of the stomach, is a key point for treating paralysis of the lower limbs, facilitating the flow of meridian qi [43]. EX points are selected for their proximal effects in improving SCI [44].

Acupuncture treatment for SCI primarily selects acupoints on the back and lumbar area and the lower limbs, with GV points mainly chosen for the back and lumbar area, and the foot yangming meridians for the lower limbs. The yang qi, distributed through yang meridians, can be regulated and nourished by selecting yang meridians, which helps improve the musculoskeletal system [45].

Association rules indicate that ST36-SP6 and GV14-GV4 are the combinations with the highest support. ST36 and SP6, commonly used together for SCI treatment, have been shown in modern research to effectively reduce inflammation and oxidative stress at the injury site and inhibit the proliferation of astrocytes, thereby improving SCI [46]. Both GV14 and GV4, as key points on the GV meridian, warm yang and facilitate qi flow. Modern research has validated that their combined use can promote autophagy to improve neural functions in SCI [39].

Cluster analysis yielded four effective clusters, with the first cluster including GV6 and GV9, key choices for acupuncture treatment of SCI, shown to benefit the regeneration of axonal neurons post-SCI [47]. The second cluster, combining GB39 and ST32, complements each other to nourish the liver and kidney, unblock meridians, and warm kidney yang [48]. The third cluster, GV14-GV4, vital points on the GV meridian, can restore yang and facilitate the flow of qi. Research by Guan et al. proved that electroacupuncture at GV14 and GV4 improves the microenvironment in SCI rats, restoring peripheral and central nervous system functions [27]. The fourth cluster includes ST36, SP6, GB34, and others, working together to nourish qi and blood, strengthen muscles and bones [49], with EX-B2 and GV points also promoting blood circulation and nourishing essence, collectively treating SCI from various aspects.

Treating SCI poses challenges and significantly impacts patients' lives. Clinical acupuncture treatment for SCI has shown effectiveness, yet a unified standard for selecting acupoints is still under development. Data mining enables the integration and analysis of content from large samples, making it feasible to explore acupoint selection patterns in acupuncture treatment for SCI. This study aimed to analyze acupoint selection in SCI treatment from relevant literature to summarize patterns and provide clinical experience. However, limitations include uneven acupoint distribution in the collected data, affecting pattern analysis, and the study's focus on literature reporting effective treatment without considering negative impacts or acupoints for complications. Further research is needed to standardize acupuncture treatment protocols for SCI.

5 CONCLUSION

This study utilized Citespace to analyze the research hotspots and frontiers in acupuncture treatment for Spinal Cord Injury (SCI). The findings indicate that targeting adenosine receptors, mTOR-mediated autophagy, and neuropathic pain are the focal points of acupuncture research in SCI treatment, with significant contributions made by researchers such as Ding Ying and Guo Yi. Through data mining, we have identified the frequency and characteristics of acupoint selection in the treatment of SCI. The most frequently used acupoints are ST36, EX-B2, SP6, GV14, and GV4, with the GV, ST, and BL meridians being the most commonly applied. The Five-shu points, Lower he-sea points, and EX points are the specific acupoints most used, with a preference for selecting acupoints on the back and lumbar area as well as the lower limbs. The combinations of ST36-SP6 and GV14-GV4 are among the most common. However, further expansion of data and clinical research is needed to substantiate the significance of these findings.

ABBREVIATIONS

Full name	Abbreviations
Spinal Cord Injury	SCI
Excerpta Medica Database	Embase
Web of Science Core Collection	WOS
Randomized Controlled Trials	RCTs
Clinical Controlled Trials	CCTs
Hand Tai Yin Lung Meridian	LU
The Large Intestine Meridian of Hand-yangming	LI
Foot Yangming Stomach Meridian	ST
Spleen Meridian of Foot Taiyin	SP
The heart channel of Hand-Shaoyin	HT
Hand Sun Small Intestine Meridian	SI
The urinary bladder channel of Foot-Taiyang	BL
The Kidney Channel of foot-Shaoyin	KI
Hand Jueyin Pericardium Meridian	PC
Hand Shaoyang Triple Jiao Meridian	SJ
Gallbladder meridian of foot shaoyang	GB
Foot Jueyin Liver Meridian	LR
Governor's pulse	GV
Ren channel	CV
Extra nerve points	EX
Ortospinal tract	CST

COMPETING INTERESTS

The authors have no relevant financial or non-financial interests to disclose.

FUNDING

This work was supported by Shanghai Municipal Commission of Science and Technology (grant number 20Y21903200) and Excellent Doctor Cultivation Project in Key Fields of Shanghai University of Traditional Chinese Medicine (GJ2023029).

AUTHOR CONTRIBUTIONS

All authors made a significant contribution to the work reported, whether that is in the conception, study design, execution, acquisition of data, analysis and interpretation, or in all these areas.

ACKNOWLEDGMENTS

We are grateful to Dr. Huang Zheng of Guanghua Hospital Affiliated to Shanghai University of Traditional Chinese Medicine.

REFERENCES

- [1] Shinozaki M, Nagoshi N, Nakamura M, et al. Mechanisms of Stem Cell Therapy in Spinal Cord Injuries. *Cells*, 2021, 10(10).
- [2] Fan Q, Cavus O, Xiong L, et al. Spinal Cord Injury: How Could Acupuncture Help? *J Acupunct Meridian Stud*, 2018, 11(4): 124-32.
- [3] Gedde M H, Lilleberg H S, Assmu J, et al. Traumatic vs non-traumatic spinal cord injury: A comparison of primary rehabilitation outcomes and complications during hospitalization. *J Spinal Cord Med*, 2019, 42(6): 695-701.
- [4] Moshi H I, Sundelin G G, Sahlen K G, et al. A one-year prospective study on the occurrence of traumatic spinal cord injury and clinical complications during hospitalisation in North-East Tanzania. *Afr Health Sci*, 2021, 21(2): 788-94.
- [5] Ding W, Hu S, Wang P, et al. Spinal Cord Injury: The Global Incidence, Prevalence, and Disability From the Global Burden of Disease Study 2019. *Spine (Phila Pa 1976)*, 2022, 47(21): 1532-40.
- [6] Jiang K, Sun Y, Chen X. Mechanism Underlying Acupuncture Therapy in Spinal Cord Injury: A Narrative Overview of Preclinical Studies. *Front Pharmacol*, 2022, 13: 875103.
- [7] Rouanet C, Reges D, Rocha E, et al. Traumatic spinal cord injury: current concepts and treatment update. *Arq Neuropsiquiatr*, 2017, 75(6): 387-93.
- [8] Gómara-Toldrà N, Sliwinski M, Dijkers M P. Physical therapy after spinal cord injury: a systematic review of treatments focused on participation. *J Spinal Cord Med*, 2014, 37(4): 371-9.
- [9] Cristante A F, Barros Filho T E, Marcon R M, et al. Therapeutic approaches for spinal cord injury. *Clinics (Sao Paulo)*, 2012, 67(10): 1219-24.

- [10] Mehta S, McIntyre A, Janzen S, et al. Systematic Review of Pharmacologic Treatments of Pain After Spinal Cord Injury: An Update. *Arch Phys Med Rehabil*, 2016, 97(8): 1381-91.e1.
- [11] Robinson N, Lorenc A, Ding W, et al. Exploring practice characteristics and research priorities of practitioners of traditional acupuncture in China and the EU-A survey. *J Ethnopharmacol*, 2012, 140(3): 604-13.
- [12] Regnier T C, Most H. Acupuncture and physical therapy for spinal cord injury: Case report. *Explore (NY)*, 2023, 19(4): 613-6.
- [13] He K, Hu R, Huang Y, et al. Effects of Acupuncture on Neuropathic Pain Induced by Spinal Cord Injury: A Systematic Review and Meta-Analysis. *Evid Based Complement Alternat Med*, 2022, 2022: 6297484.
- [14] Chen Y, Wu L, Shi M, et al. Electroacupuncture Inhibits NLRP3 Activation by Regulating CMPK2 After Spinal Cord Injury. *Front Immunol*, 2022, 13: 788556.
- [15] Chen C. Searching for intellectual turning points: progressive knowledge domain visualization. *Proc Natl Acad Sci U S A*, 2004, 101 Suppl 1(Suppl 1): 5303-10.
- [16] Xiong F, Lu J, Pan H, et al. Effect of Specific Acupuncture Therapy Combined with Rehabilitation Training on Incomplete Spinal Cord Injury: A Randomized Clinical Trial. *Evid Based Complement Alternat Med*, 2021, 2021: 5671998.
- [17] Wu W T, Li Y J, Feng A Z, et al. Data mining in clinical big data: the frequently used databases, steps, and methodological models. *Mil Med Res*, 2021, 8(1): 44.
- [18] Tu M, Xiong S, Lv S, et al. Acupuncture for Major Depressive Disorder: A Data Mining-Based Literature Study. *Neuropsychiatr Dis Treat*, 2023, 19: 1069-84.
- [19] Cai F H, Li F L, Zhang Y C, et al. Research on electroacupuncture parameters for knee osteoarthritis based on data mining. *Eur J Med Res*, 2022, 27(1): 162.
- [20] Pina A, Macedo M P, Henriques R. Clustering Clinical Data in R. *Methods Mol Biol*, 2020, 2051: 309-43.
- [21] Sabe M, Pillinger T, Kaiser S, et al. Half a century of research on antipsychotics and schizophrenia: A scientometric study of hotspots, nodes, bursts, and trends. *Neurosci Biobehav Rev*, 2022, 136: 104608.
- [22] McDonald J W, Sadowsky C. Spinal-cord injury. *Lancet*, 2002, 359(9304): 417-25.
- [23] Ewan E E, Avraham O, Carlin D, et al. Ascending dorsal column sensory neurons respond to spinal cord injury and downregulate genes related to lipid metabolism. *Sci Rep*, 2021, 11(1): 374.
- [24] Hilton B J, Husch A, Schaffran B, et al. An active vesicle priming machinery suppresses axon regeneration upon adult CNS injury. *Neuron*, 2022, 110(1): 51-69.e7.
- [25] Hu J, Jin L Q, Selzer M E. Inhibition of central axon regeneration: perspective from chondroitin sulfate proteoglycans in lamprey spinal cord injury. *Neural Regen Res*, 2022, 17(9): 1955-6.
- [26] Brennan F H, Li Y, Wang C, et al. Microglia coordinate cellular interactions during spinal cord repair in mice. *Nat Commun*, 2022, 13(1): 4096.
- [27] He G H, Ruan J W, Zeng Y S, et al. Improvement in acupoint selection for acupuncture of nerves surrounding the injury site: electro-acupuncture with Governor vessel with local meridian acupoints. *Neural Regen Res*, 2015, 10(1): 128-35.
- [28] Liu Z, Ding Y, Zeng Y S. A new combined therapeutic strategy of governor vessel electro-acupuncture and adult stem cell transplantation promotes the recovery of injured spinal cord. *Curr Med Chem*, 2011, 18(33): 5165-71.
- [29] Pei W, Meng F, Deng Q, et al. Electroacupuncture promotes the survival and synaptic plasticity of hippocampal neurons and improvement of sleep deprivation-induced spatial memory impairment. *CNS Neurosci Ther*, 2021, 27(12): 1472-82.
- [30] Mo Y P, Yao H J, Lv W, et al. Effects of Electroacupuncture at Governor Vessel Acupoints on Neurotrophin-3 in Rats with Experimental Spinal Cord Injury. *Neural Plast*, 2016, 2016: 2371875.
- [31] Tran A P, Warren P M, Silver J. New insights into glial scar formation after spinal cord injury. *Cell Tissue Res*, 2022, 387(3): 319-36.
- [32] Ding Y, Zhang D, Wang S, et al. Hematogenous Macrophages: A New Therapeutic Target for Spinal Cord Injury. *Front Cell Dev Biol*, 2021, 9: 767888.
- [33] Minic Z, Wilson S, Liu F, et al. Nanoconjugate-bound adenosine A(1) receptor antagonist enhances recovery of breathing following acute cervical spinal cord injury. *Exp Neurol*, 2017, 292: 56-62.
- [34] Zhou Y, Zhang H, Zheng B, et al. Retinoic Acid Induced-Autophagic Flux Inhibits ER-Stress Dependent Apoptosis and Prevents Disruption of Blood-Spinal Cord Barrier after Spinal Cord Injury. *Int J Biol Sci*, 2016, 12(1): 87-99.
- [35] Widerström-noga E. Neuropathic Pain and Spinal Cord Injury: Management, Phenotypes, and Biomarkers. *Drugs*, 2023, 83(11): 1001-25.
- [36] Shiao R, Lee-Kubli C A. Neuropathic Pain After Spinal Cord Injury: Challenges and Research Perspectives. *Neurotherapeutics*, 2018, 15(3): 635-53.
- [37] Xiao N, Li Y, Shao M L, et al. Jiaji (EX-B2)-Based Electroacupuncture Preconditioning Attenuates Early Ischaemia Reperfusion Injury in the Rat Myocardium. *Evid Based Complement Alternat Med*, 2020, 2020: 8854033.
- [38] Wu M F, Zhang S Q, Liu J B, et al. Neuroprotective effects of electroacupuncture on early- and late-stage spinal cord injury. *Neural Regen Res*, 2015, 10(10): 1628-34.

- [39] Li K, Liu J, Song L, et al. Effect of Electroacupuncture Treatment at Dazhui (GV14) and Mingmen (GV4) Modulates the PI3K/AKT/mTOR Signaling Pathway in Rats after Spinal Cord Injury. *Neural Plast*, 2020, 2020: 5474608.
- [40] Zeng Y S, Ding Y, Xu H Y, et al. Electro-acupuncture and its combination with adult stem cell transplantation for spinal cord injury treatment: A summary of current laboratory findings and a review of literature. *CNS Neurosci Ther*, 2022, 28(5): 635-47.
- [41] Song Y Y, Ni G X. Professor NI Guang-xia's clinical experience in treatment of wei syndrome with xingshen tongyang needling technique of acupuncture. *Zhongguo Zhen Jiu*, 2020, 40(4): 411-3.
- [42] Ahn C B, Jang K J, Yoon H M, et al. Sa-Ahm Five Element acupuncture. *J Acupunct Meridian Stud*, 2010, 3(3): 203-13.
- [43] Wu S Y, Lin C H, Chang N J, et al. Combined effect of laser acupuncture and electroacupuncture in knee osteoarthritis patients: A protocol for a randomized controlled trial. *Medicine (Baltimore)*, 2020, 99(12): e19541.
- [44] KE X, WANG Y, ZHANG A, et al. Neurological protection effects of "paraplegia-triple-needling method" on rats with incomplete spinal cord injury. *Zhongguo Zhen Jiu*, 2015, 35(6): 585-9.
- [45] Yao F, Zhao Y, Jiang S, et al. The theoretical basis for chronic fatigue syndrome from bladder meridian of foot-taiyang. 2015, 35(3): 295-8.
- [46] Dai N, Huang S Q, Tang C L, et al. Electroacupuncture improves locomotor function by regulating expression of inflammation and oxidative stress-related proteins in mice with spinal cord injury. 2019, 44(11): 781-6.
- [47] Xu H, Yang Y, Deng Q W, et al. Governor Vessel Electro-Acupuncture Promotes the Intrinsic Growth Ability of Spinal Neurons through Activating Calcitonin Gene-Related Peptide/ α -Calcium/Calmodulin-Dependent Protein Kinase/Neurotrophin-3 Pathway after Spinal Cord Injury. *J Neurotrauma*, 2021, 38(6): 734-45.
- [48] Yang J H, Lv J G, Wang H, et al. Electroacupuncture promotes the recovery of motor neuron function in the anterior horn of the injured spinal cord. *Neural Regen Res*, 2015, 10(12): 2033-9.
- [49] Liu L Y, Zhang J B, Jin C Y, et al. Could Huatuo Jiaji (EX-B 2) Acupoint Be Assigned to the Governor Vessel? 2018, 43(11): 744-6.

TRANSMISSION MODEL OF INFLUENZA A WITH ASYMPTOMATIC INFECTION AND ENVIRONMENTAL TRANSMISSION

WenXuan Li

School of Mathematical Science, Chengdu University of Technology, Yibin 644000, Sichuan, China.

Corresponding Email: li_wen_xuan5@163.com

Abstract: The present study aims to investigate the impact of asymptotically infected individuals and the presence of free virus in the environment on the transmission of influenza A virus. To this end, an infectious disease model of influenza A virus with asymptomatic infection and environmental transmission is established. Initially, the nonnegativity and boundedness of the global positive solution of the model are obtained, and the fundamental regeneration number of the model R_0 , is determined by the method of the spectral radius of the next-generation operator. Utilising qualitative ordinary differential equations, stability theory and fluctuation priming, it is demonstrated that the disease-free equilibrium point is globally asymptotically stable at $R_0 < 1$. Furthermore, the consistent persistence of the disease is substantiated by constructing an auxiliary system at $R_0 > 1$. The validity of the theoretical results is substantiated by numerical simulations. The innovative aspect of this paper is the integration of asymptomatic infection and environmental transmission into a unified model. This comprehensive approach elucidates the transmission mechanism of influenza A within the population, thus offering a novel perspective through which to attain a more profound comprehension of the transmission of influenza A.

Keywords: A symptomatic infection; Multiple pathways of transmission; Basic regeneration number; Global asymptotic stabilization; Uniform persistence

1 INTRODUCTION

Influenza A, is an acute respiratory infection caused by influenza A viruses. Influenza A viruses are highly mutable and can spread rapidly among populations by droplet transmission, direct contact, and airborne aerosols[1-3]. Furthermore, the capacity of influenza A viruses to persist and propagate on environmental surfaces underscores the potential for their transmission under diverse environmental conditions, which in turn may shape their propagation within the population[4-5]. The rapid and widespread dissemination of influenza A viruses has profound consequences for public health, leading to significant morbidity and mortality, as well as substantial economic losses[6]. Historical precedent demonstrates the capacity of influenza A to spark pandemics, as evidenced by the H1N1 epidemic of 2009[7]. Consequently, the development of effective prevention and control strategies for influenza A is of paramount importance. The mutability of influenza A viruses poses a significant challenge in the implementation of traditional prevention and control measures, which often prove ineffective in fully containing their spread. This underscores the necessity for continuous exploration of novel prevention and control strategies.

Mathematical modeling has emerged as a valuable instrument in the study of infectious disease transmission, facilitating our understanding of the underlying mechanisms and enabling accurate epidemic forecasting. This, in turn, provides a robust scientific foundation for the development of effective public health policies. In recent years, with the advancement of computing capabilities and the development of mathematical theory, the field of infectious disease modeling has garnered significant attention[8]. Notably, in the context of respiratory infectious diseases, such as influenza A, the application of mathematical models has yielded noteworthy outcomes[9].

In light of the aforementioned discussion, the objective of this paper is to develop an infectious disease model of influenza A virus with asymptomatic infection and environmental transmission to study the kinetic behavior of influenza A transmission. The structure of this paper is outlined as follows: The initial section of this study is devoted to the modeling process. Subsequent sections are dedicated to the verification of two crucial properties of the global positive solution of the model: its nonnegativity and its boundedness. The third section involves the derivation of the fundamental regeneration number of the model and the demonstration of the existence and uniqueness of the disease-free equilibrium point. The fourth section focuses on the proof of the global asymptotic stability of the disease-free equilibrium point. The fifth section provides a rigorous justification for the model's consistent persistence. Ultimately, numerical simulations are implemented to validate the accuracy of the obtained results.

2 FORMULATION OF THE MODEL

The model under consideration in this paper consists of four human compartments: susceptible (S), asymptotically infected (A), symptomatically infected (I), and recovered (R), and an environmental compartment: the free virus (W) contained in the environment and released by the infected person. A diagram illustrating the model's compartmental structure is presented in Figure 1.

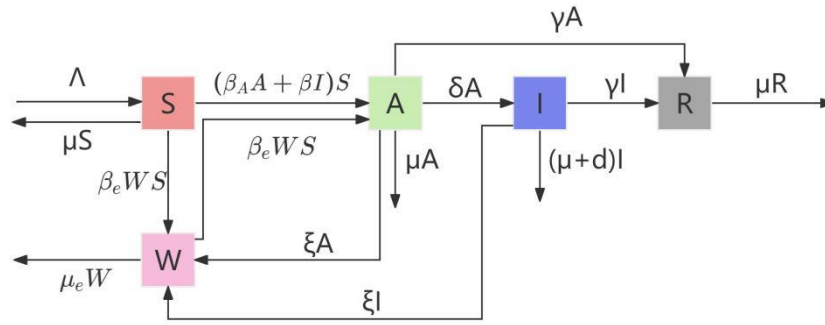


Figure 1 Diagram of the Model's Chamber

The transmission model of Influenza A is as follows:

$$\begin{cases} \frac{dS(t)}{dt} = \Lambda - \beta_A A(t)S(t) - \beta I(t)S(t) - \beta_e W(t)S(t) - \mu S(t) \\ \frac{dA(t)}{dt} = \beta_A A(t)S(t) + \beta I(t)S(t) + \beta_e W(t)S(t) - \mu A(t) - \delta A(t) - \gamma A(t) \\ \frac{dI(t)}{dt} = \delta A(t) - \gamma I(t) - \mu I(t) - dI(t) \\ \frac{dW(t)}{dt} = \xi A(t) + \xi I(t) - \mu_e W(t) \\ \frac{dR(t)}{dt} = \gamma A(t) + \gamma I(t) - \mu R(t) \end{cases} \quad (1)$$

In the model, Λ represents the birth rate of the population, μ denotes the natural death rate, d representative case fatality rate for symptomatic infections, β_A and β respectively represent the transmission rates from asymptomatic and symptomatic infected individuals to susceptible individuals. β_e indicates the transmission rate caused by environmental factors, while δ represents the transfer rate from asymptomatic to symptomatic infected individuals. Additionally, μ_e denotes the morbidity-related mortality rate of infected individuals induced by environmental factors. γ represent the recovery rates of asymptomatic and symptomatic infected individuals, ξ reflect the rate of viral shedding from asymptomatic and symptomatic infected individuals into the environment.

Given that the differential equations of $S(t), A(t), I(t), W(t)$ in the model do not include $R(t)$, $R(t)$ can be decoupled. Therefore, we consider the subsystem:

$$\begin{cases} \frac{dS(t)}{dt} = \Lambda - \beta_A A(t)S(t) - \beta I(t)S(t) - \beta_e W(t)S(t) - \mu S(t) \\ \frac{dA(t)}{dt} = \beta_A A(t)S(t) + \beta I(t)S(t) + \beta_e W(t)S(t) - \mu A(t) - \delta A(t) - \gamma A(t) \\ \frac{dI(t)}{dt} = \delta A(t) - \gamma I(t) - \mu I(t) - dI(t) \\ \frac{dW(t)}{dt} = \xi A(t) + \xi I(t) - \mu_e W(t) \end{cases} \quad (2)$$

For any solution of the system that satisfies the initial conditions $(S(0), A(0), I(0), W(0))$:

$$X(t) = (S(t), A(t), I(t), W(t)) \quad (3)$$

There exists $X(t) \in \Gamma$, among which,

$$\Gamma = \{(S, A, I, W) \in R_+^4 \mid S(t) + A(t) + I(t) + W(t) \leq \frac{\xi A}{\mu \mu_e} + \frac{\Lambda}{\mu}\} \quad (4)$$

3 THE NON-NEGATIVITY AND BOUNDEDNESS OF THE MODEL

Theorem 1: Γ is the maximal positive invariant set of the model (2).

Proof : First, we prove the non-negativity. For any solution $(S(t), A(t), I(t), W(t))$ that satisfies the initial conditions $(S(0), A(0), I(0), W(0))$. Using the contradiction method, assume there exists t_0 such that $S(t_0) = 0$ and $\frac{dS(t_0)}{dt} < 0$, Substituting into the first equation of model (2), we get $\frac{dS(t_0)}{dt} = \Lambda - \beta_A A(t_0)S(t_0) - \beta I(t_0)S(t_0) -$

$\beta_e W(t_0)S(t_0) - \mu S(t_0)$, Therefore, $\frac{dS(t_0)}{dt} = \Lambda < 0$, this contradicts $\Lambda > 0$, thus the assumption is not valid. Therefore, $\frac{dS(t)}{dt} \geq 0$.

Considering $\frac{dA(t)}{dt}$, assume that at t_0 , $A(t_0) = 0$ and $\frac{dA(t_0)}{dt} < 0$. At t_1 , we have $I(t_1) = 0$ and $\frac{dI(t_1)}{dt} < 0$. At t_2 , we have $W(t_2) = 0$ and $\frac{dW(t_2)}{dt} < 0$. Taking $t = \min\{t_0, t_1, t_2\}$, if $t = t_0$, then $I(t) \geq 0$ and $W(t) \geq 0$. Thus, $\frac{dA(t_0)}{dt} = \beta I(t_0)S(t_0) + \beta_e W(t_0)S(t_0) \geq 0$. Since $\frac{dA(t_0)}{dt} < 0$ leads to a contradiction, we conclude that $\frac{dA(t)}{dt} \geq 0$.

Similarly, for $\frac{dI(t)}{dt}$ and $\frac{dW(t)}{dt}$, the above method can be applied to demonstrate their non-negativity. In summary, all state variables in model (2) are non-negative.

Next, we verify the boundedness. Summing the first three equations in model (2), we obtain:

$$d(S + A + I) = \Lambda - \mu S - \mu A - \gamma A - \gamma I - dI - \mu I \leq \Lambda - \mu(S + A + I) \quad (5)$$

Thus,

$$S + A + I \leq \frac{\Lambda}{\mu} \quad (6)$$

Moreover, since

$$dW = \xi(A + I) - \mu_e W \leq \frac{\xi\Lambda}{\mu} \quad (7)$$

it follows that:

$$W \leq \frac{\xi\Lambda}{\mu\mu_e} \quad (8)$$

Consequently,

$$S + A + I + W \leq \frac{\xi\Lambda}{\mu\mu_e} + \frac{\Lambda}{\mu} \quad (9)$$

Clearly, we already know that $S + A + I + W \geq 0$. Therefore, the state variables in model (2) are all bounded.

In conclusion, the theorem 1 is established. That is, Γ is the maximal positive invariant set of model (2).

4 EXISTENCE OF THE BASIC REPRODUCTION NUMBER AND THE DISEASE-FREE EQUILIBRIUM POINT

In model (2), when $I = 0$, according to the second and fourth equations, it follows that $A = 0$ and $W = 0$. Substituting into the first equation yields $S = \frac{\Lambda}{\mu}$. Therefore, model (2) has a unique disease-free equilibrium point $E_0 = (\frac{\Lambda}{\mu}, 0, 0, 0)$.

Next, we will calculate the basic reproduction number using the next-generation matrix method [10].

Rewrite the equations in model (2):

$$\begin{cases} \frac{dA(t)}{dt} = \beta_A A(t)S(t) + \beta I(t)S(t) + \beta_e W(t)S(t) - \mu A(t) - \delta A(t) - \gamma A(t) \\ \frac{dI(t)}{dt} = \delta A(t) - \gamma I(t) - \mu I(t) - dI(t) \\ \frac{dW(t)}{dt} = \xi A(t) + \xi I(t) - \mu_e W(t) \end{cases} \quad (10)$$

as,

$$\frac{dA}{dt} = \mathcal{F}_1(S(t), A(t), I(t), W(t)) - \mathcal{V}_1(S(t), A(t), I(t), W(t)) \quad (11)$$

$$\frac{dI}{dt} = \mathcal{F}_2(S(t), A(t), I(t), W(t)) - \mathcal{V}_2(S(t), A(t), I(t), W(t)) \quad (12)$$

$$\frac{dW}{dt} = \mathcal{F}_3(S(t), A(t), I(t), W(t)) - \mathcal{V}_3(S(t), A(t), I(t), W(t)) \quad (13)$$

where,

$$\mathcal{F}_1(S(t), A(t), I(t), W(t)) = \beta_A A(t)S(t) + \beta I(t)S(t) + \beta_e W(t)S(t) \quad (14)$$

$$\mathcal{F}_2(S(t), A(t), I(t), W(t)) = \delta A(t) \quad (15)$$

$$\mathcal{F}_3(S(t), A(t), I(t), W(t)) = \xi A(t) + \xi I(t) \quad (16)$$

$$\mathcal{V}_1(S(t), A(t), I(t), W(t)) = \mu A(t) + \delta A(t) + \gamma A(t) \quad (17)$$

$$\mathcal{V}_2(S(t), A(t), I(t), W(t)) = \gamma I(t) + \mu I(t) + dI(t) \quad (18)$$

$$\mathcal{V}_3(S(t), A(t), I(t), W(t)) = \mu_e W(t) \quad (19)$$

leads to the matrices $\mathcal{F} = \begin{pmatrix} \mathcal{F}_1 \\ \mathcal{F}_2 \\ \mathcal{F}_3 \end{pmatrix}$ and $\mathcal{V} = \begin{pmatrix} \mathcal{V}_1 \\ \mathcal{V}_2 \\ \mathcal{V}_3 \end{pmatrix}$. The Jacobian matrices at the equilibrium point $E_0 = (\frac{\Lambda}{\mu}, 0, 0, 0)$ are

represented by

$$F = \begin{pmatrix} \frac{\partial \mathcal{F}_1}{\partial A} & \frac{\partial \mathcal{F}_1}{\partial I} & \frac{\partial \mathcal{F}_1}{\partial W} \\ \frac{\partial \mathcal{F}_2}{\partial A} & \frac{\partial \mathcal{F}_2}{\partial I} & \frac{\partial \mathcal{F}_2}{\partial W} \\ \frac{\partial \mathcal{F}_3}{\partial A} & \frac{\partial \mathcal{F}_3}{\partial I} & \frac{\partial \mathcal{F}_3}{\partial W} \end{pmatrix} = \begin{pmatrix} \beta_A & \beta & \beta_e \\ \delta & 0 & 0 \\ \xi & \xi & 0 \end{pmatrix} \tag{20}$$

and

$$V = \begin{pmatrix} \frac{\partial \mathcal{V}_1}{\partial A} & \frac{\partial \mathcal{V}_1}{\partial I} & \frac{\partial \mathcal{V}_1}{\partial W} \\ \frac{\partial \mathcal{V}_2}{\partial A} & \frac{\partial \mathcal{V}_2}{\partial I} & \frac{\partial \mathcal{V}_2}{\partial W} \\ \frac{\partial \mathcal{V}_3}{\partial A} & \frac{\partial \mathcal{V}_3}{\partial I} & \frac{\partial \mathcal{V}_3}{\partial W} \end{pmatrix} = \begin{pmatrix} \mu + \delta + \gamma & 0 & 0 \\ 0 & \gamma + \mu + d & 0 \\ 0 & 0 & \mu_e \end{pmatrix} \tag{21}$$

For the sake of computational simplicity, the matrices F and V are reformulated as:

$$F_1 = \begin{pmatrix} \beta_A & \beta & \beta_e \\ 0 & 0 & 0 \\ 0 & 0 & 0 \end{pmatrix} \quad V_1 = \begin{pmatrix} \mu + \delta + \gamma & 0 & 0 \\ -\delta & \gamma + \mu + d & 0 \\ -\xi & -\xi & \mu_e \end{pmatrix} \tag{22}$$

After computation, the results yield:

$$V_1^{-1} = \begin{pmatrix} \frac{1}{\mu + \delta + \gamma} & 0 & 0 \\ -\delta & \frac{1}{\gamma + \mu + d} & 0 \\ \frac{\delta \xi + \xi(\gamma + \mu + d)}{(\mu + \delta + \gamma)(\gamma + \mu + d)\mu_e} & \frac{\xi}{(\gamma + \mu + d)\mu_e} & \mu_e \end{pmatrix} \tag{23}$$

Define the next-generation matrix as $M = FV_1^{-1}$. Then, it follows that:

$$M = \begin{pmatrix} \frac{\beta_A(\gamma + \mu + d)\mu_e + \beta\delta\mu_e + \xi\beta_e(\gamma + \mu + d)}{(\mu + \delta + \gamma)(\gamma + \mu + d)\mu_e} & \frac{\beta\mu_e + \xi\beta_e}{(\gamma + \mu + d)\mu_e} & \frac{\beta_e}{\mu_e} \\ 0 & 0 & 0 \\ 0 & 0 & 0 \end{pmatrix} \tag{24}$$

The basic reproduction number R_0 is defined as the spectral radius of the matrix M. Thus, R_0 is given by:

$$R_0 = \frac{\beta_A\mu_e(\gamma + \mu + d) + \beta\delta\mu_e + \xi\beta_e(\gamma + \mu + d)}{(\mu + \delta + \gamma)(\gamma + \mu + d)\mu_e} \cdot \frac{\Lambda}{\mu} \tag{25}$$

5 THE STABILITY OF THE DISEASE-FREE EQUILIBRIUM POINT

Theorem 2: When $R_0 < 1$, the disease-free equilibrium point $E_0 = (\frac{\Lambda}{\mu}, 0, 0, 0)$ is locally asymptotically stable.

Proof: The Jacobian matrix at E_0 for Model (2) is given by:

$$J(E_0) = \begin{bmatrix} -\mu & \frac{\beta_A\Lambda}{\mu} & \frac{\beta\Lambda}{\mu} & \frac{\beta_e\Lambda}{\mu} \\ 0 & \frac{\beta_A\Lambda}{\mu} - \mu - \delta - \gamma & \frac{\beta\Lambda}{\mu} & \frac{\beta_e\Lambda}{\mu} \\ 0 & \delta & -\gamma - \mu - d & 0 \\ 0 & \xi & \xi & -\mu_e \end{bmatrix} \tag{26}$$

It is evident that $J(E_0)$ has one negative eigenvalue $\lambda_1 = -\mu < 0$. The remaining eigenvalues satisfy the equation:

$$\left(\lambda - \frac{\beta_A\Lambda}{\mu} + \mu + \delta + \gamma\right)\left(\lambda + \gamma + \mu + d\right)\left(\lambda + \mu_e\right) = \frac{\beta_e\Lambda\xi}{\mu}(\delta + \lambda + \gamma + \mu + d) + \frac{\beta\Lambda\xi}{\mu}(\lambda + \mu_e) \tag{27}$$

Assuming that when $R_0 < 1$, there exists an eigenvalue λ^* , and $Re(\lambda^*) \geq 0$, then we divide both sides of (26) by:

$$\left(\lambda^* - \frac{\beta_A\Lambda}{\mu} + \mu + \delta + \gamma\right)\left(\lambda^* + \gamma + \mu + d\right)\left(\lambda^* + \mu_e\right) \tag{28}$$

Taking the absolute value, we obtain:

$$1 = \left| \frac{\beta_e\Lambda\xi}{(\mu\lambda^* + \beta_A\Lambda + \mu^2 + \mu\delta + \mu\gamma)(\lambda^* + \mu_e)} + \frac{\beta\Lambda\delta}{(\mu\lambda^* + \beta_A\Lambda + \mu^2 + \mu\delta + \mu\gamma)(\lambda^* + \gamma + \mu + d)} + \frac{\beta_e\Lambda\xi\delta}{(\mu\lambda^* - \beta_A\Lambda + \mu^2 + \mu\delta + \mu\gamma)(\lambda^* + \gamma + \mu + d)(\lambda^* + \mu_e)} \right| \tag{29}$$

Let $\lambda^* = a + bi$, $a \geq 0$, then: $|\lambda + \mu_e| a + \mu_e \geq \mu_e$, $|\lambda + \gamma + \mu + d| \geq a + \gamma + \mu + d \geq \gamma + \mu + d$, $|\mu\lambda + \beta_A\Lambda + \mu^2 + \mu\delta + \mu\gamma| \geq |\mu a + \beta_A\Lambda + \mu^2 + \mu\delta + \mu\gamma| \geq |\beta_A\Lambda + \mu^2 + \mu\delta + \mu\gamma|$.

Thus,

$$1 = \left| \frac{\beta_e\Lambda\xi}{(\mu\lambda^* + \beta_A\Lambda + \mu^2 + \mu\delta + \mu\gamma)(\lambda^* + \mu_e)} + \frac{\beta\Lambda\delta}{(\mu\lambda^* + \beta_A\Lambda + \mu^2 + \mu\delta + \mu\gamma)(\lambda^* + \gamma + \mu + d)} + \frac{\beta_e\Lambda\xi\delta}{(\mu\lambda^* - \beta_A\Lambda + \mu^2 + \mu\delta + \mu\gamma)(\lambda^* + \gamma + \mu + d)(\lambda^* + \mu_e)} \right| \leq \left| \frac{\beta_e\Lambda\xi}{(\beta_A\Lambda + \mu^2 + \mu\delta + \mu\gamma)\mu_e} + \frac{\beta\Lambda\delta}{(\beta_A\Lambda + \mu^2 + \mu\delta + \mu\gamma)(\gamma + \mu + d)} + \frac{\beta_e\Lambda\xi\delta}{(\beta_A\Lambda + \mu^2 + \mu\delta + \mu\gamma)(\gamma + \mu + d)\mu_e} \right| = \frac{\beta\delta\mu_e + \xi\beta_e(\gamma + \mu + d)\delta}{(\beta_A\Lambda + \mu^2 + \mu\delta + \mu\gamma)(\gamma + \mu + d)\mu_e} \cdot \frac{\Lambda}{\mu} \tag{30}$$

Moreover, based on the result for R_0 , it can be reformulated as follows:

$$\frac{\beta\delta\mu_e + \xi\beta_e(\gamma + \mu + d)\delta}{(\mu + \delta + \gamma)(\gamma + \mu + d)\mu_e} \cdot \frac{\Lambda}{\mu} = R_0 - \frac{\beta_A\mu_e(\gamma + \mu + d)}{(\mu + \delta + \gamma)(\gamma + \mu + d)\mu_e} \cdot \frac{\Lambda}{\mu} \tag{31}$$

Consequently, we deduce that $1 \leq R_0 - \frac{\beta_A\mu_e(\gamma + \mu + d)}{(\mu + \delta + \gamma)(\gamma + \mu + d)\mu_e} \cdot \frac{\Lambda}{\mu}$ is in direct contradiction with $R_0 < 1$, thereby demonstrating that the initial assumption is invalid.

Therefore, when $R_0 < 1$, all the eigenvalues of $J(E_0)$ exhibit negative real parts, implying that the disease-free equilibrium point of model (2) is locally asymptotically stable.

Lemma 1[11]: Let B be bounded and continuously differentiable. Then there exist two sequences $\{s_n\}$ and $\{t_n\}$ such that $s_n \rightarrow \infty, t_n \rightarrow \infty, B(s_n) \rightarrow B_\infty, B'(s_n) \rightarrow 0, B(t_n) \rightarrow B^\infty$ and $B'(t_n) \rightarrow 0$ as $n \rightarrow \infty$.

Theorem 3: When $R_0 < 1$, the disease-free equilibrium point $E_0 = \left(\frac{\Lambda}{\mu}, 0, 0, 0\right)$ is globally asymptotically stable.

Proof: For the model (10):

$$\begin{cases} \frac{dA(t)}{dt} = \beta_A A(t)S(t) + \beta I(t)S(t) + \beta_e W(t)S(t) - \mu A(t) - \delta A(t) - \gamma A(t) \\ \frac{dI(t)}{dt} = \delta A(t) - \gamma I(t) - \mu I(t) - dI(t) \\ \frac{dW(t)}{dt} = \xi A(t) + \zeta I(t) - \mu_e W(t) \end{cases} \quad (10)$$

Let the sequence $\{t_n\}$, substituting this into the model yields:

$$\begin{cases} \frac{dA(t_n)}{dt} = \beta_A A(t_n)S(t_n) + \beta I(t_n)S(t_n) + \beta_e W(t_n)S(t_n) - \mu A(t_n) - \delta A(t_n) - \gamma A(t_n) \\ \frac{dI(t_n)}{dt} = \delta A(t_n) - \gamma I(t_n) - \mu I(t_n) - dI(t_n) \\ \frac{dW(t_n)}{dt} = \xi A(t_n) + \zeta I(t_n) - \mu_e W(t_n) \end{cases} \quad (32)$$

From Lemma 1, it can be concluded that when $t_n \rightarrow \infty, A(t_n) \rightarrow A^\infty, I(t_n) \rightarrow I^\infty$ and $W(t_n) \rightarrow 0$. Therefore, it can be derived from the second equation of the system of equations (32) that:

$$\frac{dI(t_n)}{t_n} \leq \delta A^\infty - (\gamma + \mu + d)I^\infty, 0 \leq \delta A^\infty - (\gamma + \mu + d)I^\infty \quad (33)$$

$$I^\infty \leq \frac{\delta}{\gamma + \mu + d} A^\infty \quad (34)$$

Similarly, it can be inferred from the third equation of the system of equations (4) that $W^\infty \leq \frac{\xi}{\mu_e} + \frac{\xi \delta}{\mu_e(\gamma + \mu + d)} A^\infty$. For the first equation of the system of equations (4): $\frac{dA(t_n)}{dt} \leq \beta_A A^\infty S^\infty + \beta I^\infty S^\infty + \beta_e W^\infty S^\infty - (\mu + \delta + \gamma)A^\infty$, it can be readily deduced that: $S^\infty \leq \frac{\Lambda}{\mu}$. By substituting the values, it can be derived that: $0 \leq \left[\beta_A \frac{\Lambda}{\mu} + \beta \frac{\Lambda}{\mu} \frac{\delta}{\gamma + \mu + d} + \beta_e \frac{\Lambda}{\mu} \left(\frac{\xi}{\mu_e} + \frac{\xi \delta}{\mu_e(\gamma + \mu + d)} \right) - (\mu + \delta + \gamma) \right] A^\infty$, it can be concluded that: $A^\infty \leq R_0 A^\infty$. Additionally, given that $R_0 < 1$, it can be inferred that $A^\infty = 0$, which subsequently leads to the conclusion that $I^\infty = 0$ and $W^\infty = 0$. From this, it can be deduced that $A \rightarrow 0, I \rightarrow 0, W \rightarrow 0$.

Let us further define a sequence $\{s_n\}$. Substituting this sequence into the first equation of Model (2) results in the following expression:

$$\frac{dS(s_n)}{ds_n} = \Lambda - \beta_A A(s_n)S(s_n) - \beta I(s_n)S(s_n) - \beta_e W(s_n)S(s_n) - \mu S(s_n) \quad (35)$$

From Lemma 1, it can be concluded that when $s_n \rightarrow \infty, \frac{dS(s_n)}{ds_n} \rightarrow 0, A(t_n) \rightarrow A^\infty = 0, I(t_n) \rightarrow I^\infty = 0$ and $W(t_n) \rightarrow W^\infty = 0$. Therefore, $0 = \Lambda - \mu S_\infty, S_\infty = \frac{\Lambda}{\mu}$, then $S_\infty = S^\infty = \frac{\Lambda}{\mu}$. Thus, the disease-free equilibrium point E_0 is globally attractive. Furthermore, according to Theorem 2, the disease-free equilibrium point E_0 is locally asymptotically stable, thus indicating that E_0 is globally asymptotically stable.

6 UNIFORM PERSISTENCE OF THE MODEL

Theorem 4: When $R_0 > 1$, the model (2) demonstrated uniform persistence behavior. That is, there exists $\varepsilon > 0$ such that:

$$\liminf_{t \rightarrow \infty} (A(t), I(t), W(t)) \geq (\varepsilon, \varepsilon, \varepsilon)$$

Proof: Define $x = \{S(t), A(t), I(t), W(t) | S + A + I + W \leq \frac{\xi \Lambda}{\mu \mu_e} + \frac{\Lambda}{\mu}\}$, where

$x_0 = \{(S, A, I, W) \in x | S, A, I, W > 0\}$, let $\partial x_0 = x \setminus x_0$. From model (2), we obtain:

$$A(t) \geq A(t_0) e^{-(\mu + \delta + \gamma)(t - t_0)} \geq 0 \quad (36)$$

$$I(t) \geq I(t_0) e^{-(\mu + d + \gamma)(t - t_0)} \geq 0 \quad (37)$$

$$W(t) \geq W(t_0) e^{-\mu_e(t - t_0)} \geq 0 \quad (38)$$

Thus, x and x_0 are positively invariant sets, and ∂x_0 is relative closed set of x let:

$$M_\partial = \{S(0), A(0), I(0), W(0) | S(t), A(t), I(t), W(t) \in \partial x_0, \forall t \geq 0\}$$

It is demonstrated that $M_\partial = \{S(0), 0, 0, 0 | S(t) \geq 0\}$ holds true, clearly, $\{S(0), 0, 0, 0 | S(t) \geq 0\} \subseteq M_\partial$ and to prove $M_\partial \subseteq \{S(0), 0, 0, 0 | S(t) \geq 0\}$. Let $(S(0), A(0), I(0), W(0)) \in M_\partial$. It is essential to establish that for all $\forall t \geq 0, A(t) =$

$0, I(t) = 0, W(t) = 0$. This argument employs proof by contradiction, assuming otherwise, there exists a $\exists t_0 \geq 0$ such that:

- (i) $A(t_0) > 0$
- (ii) $I(t_0) > 0$
- (iii) $W(t_0) > 0$

For (ii), solving for (37) yields: For all $t > t_0$, there exists $I(t) > 0$, substituting into model (2) yields $A(t) > 0, W(t) > 0$, thus $(S(t), A(t), I(t), W(t)) \notin \partial x_0$. This contradicts the assumption. A contradiction can be derived in a similar manner for (iii). For (i), when $t > t_0$, it can be inferred that $I(t) = I(t_0)e^{(\gamma+\mu+d)t} + \int_{t_0}^t k\delta A(t)e^{(\mu+\delta+\gamma)t} dt$. Clearly, when $A(t) > 0$, we have $I(t) > 0$. Similarly, it follows that $W(t) > 0$.

In summary, $(S(t), A(t), I(t), W(t)) \notin \partial x_0$ contradicts the hypothesis. Thus, it is proven $M_\partial = \{S(0), 0, 0, 0 | S(t) \geq 0\}$. The disease-free equilibrium point E_0 of model (2) is globally asymptotically stable, and there is only one equilibrium point E_0 in M_∂ .

We will next demonstrate that E_0 exhibits weak exclusion with respect to the set x_0 , which requires showing that $\limsup_{t \rightarrow \infty} (\Phi(t), E_0) > 0$. It suffices to prove that $W_{(E_0)}^S \cap x_0 = \emptyset$. Using a proof by contradiction, we assume that this conclusion is not valid. Therefore, there exists a positive solution $(S(t), A(t), I(t), W(t))$ for model (2), such that $\lim_{t \rightarrow \infty} (S(t), A(t), I(t), W(t)) = (S^0, 0, 0, 0)$.

Define $M = F - V$, given that $R_0 > 1$, it follows that $S(M) > 0$, For sufficiently small $\varepsilon > 0$, there exists $S(M - M_\varepsilon) > 0$. In this context,

$$M_\varepsilon = \begin{pmatrix} \beta_A \varepsilon & \beta \varepsilon & \beta_e \varepsilon \\ 0 & 0 & 0 \\ 0 & 0 & 0 \end{pmatrix} \tag{39}$$

There exists $T > 0$ such that $\forall t > T$, there holds $S^0 - \varepsilon < S(t) < S^0 + \varepsilon$, leading to the derivation of the differential inequality:

$$\begin{cases} \frac{dA}{dt} \geq \beta_A(S^0 - \varepsilon)A + \beta(S^0 - \varepsilon)I + \beta_e(S^0 - \varepsilon)W - (\mu + \delta + \gamma)A \\ \frac{dI}{dt} = \delta A - (\gamma + \mu + d)I \\ \frac{dW}{dt} = \xi A + \xi I - \mu_e W \end{cases} \tag{40}$$

Consider the auxiliary system:

$$\begin{cases} \frac{dA}{dt} = \beta_A(S^0 - \varepsilon)A + \beta(S^0 - \varepsilon)I + \beta_e(S^0 - \varepsilon)W - (\mu + \delta + \gamma)A \\ \frac{dI}{dt} = \delta A - (\gamma + \mu + d)I \\ \frac{dW}{dt} = \xi A + \xi I - \mu_e W \end{cases} \tag{41}$$

Because $S(M - M_\varepsilon) > 0$, as $t \rightarrow \infty$, it follows that $A(t) \rightarrow \infty, I(t) \rightarrow \infty, W(t) \rightarrow \infty$. This contradicts the assumption that $A(t) \rightarrow 0, I(t) \rightarrow 0, W(t) \rightarrow 0$ when $t \rightarrow \infty$ [12], thus, it is proven: $W_{(E_0)}^S \cap x_0 = \emptyset$.

In summary, it can be obtained that when $R_0 > 1$, the model (2) concerning $(x_0, \partial x_0)$ persists consistently.

7 NUMERICAL SIMULATION

Assuming:

$\Lambda = 1.4, \beta_A = 0.0001, \beta = 0.0001, \beta_e = 0.003, \mu = 0.01, \gamma = 0.05, \mu_e = 0.01, d = 0.006, \xi = 0.001, \delta = 0.02$, the calculation yields $R_0 = 0.912, R_0 < 1$. According to Theorem 4, the model (2) has a globally asymptotically stable disease-free equilibrium point, and its numerical simulation is shown in Figure 2.

Assuming:

$\Lambda = 1.4, \beta_A = 0.0001, \beta = 0.0001, \beta_e = 0.01, \mu = 0.007, \gamma = 0.05, \mu_e = 0.01, d = 0.006, \xi = 0.001, \delta = 0.02$, the calculation yields $R_0 = 3.764, R_0 > 1$. According to Theorem 5, the model (2) is uniformly persistent, and its numerical simulation is shown in Figure 3.

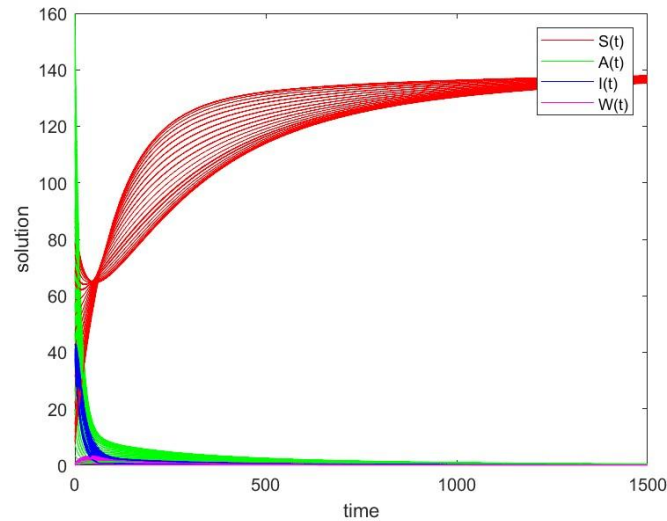


Figure 2 $R_0 < 1$

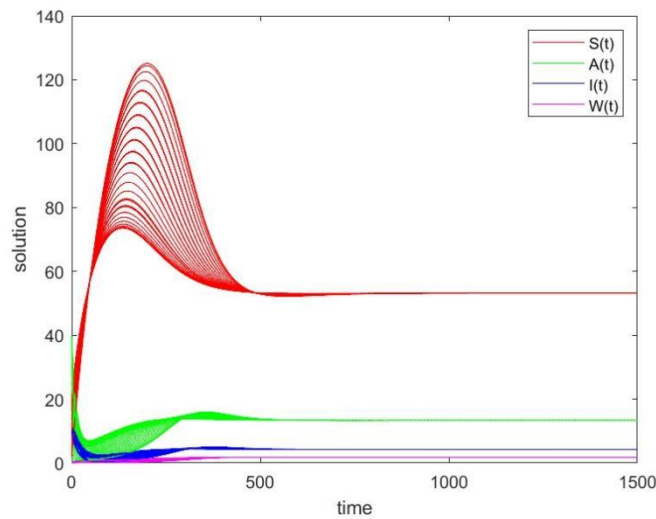


Figure 3 $R_0 > 1$

8 CONCLUSION

This study establishes a comprehensive dynamical model for the transmission of H1N1 influenza virus, considering asymptomatic infection mechanisms and environmental transmission pathways.(SAIWR model). In-depth analysis of the dual roles of asymptomatic carriers and environmental virus transmission mechanisms on the dynamics of epidemic evolution. Firstly, the study rigorously demonstrates the non-negativity and boundedness of the model, thereby ensuring a robust mathematical foundation for epidemiological research. Subsequently, utilizing the next-generation matrix method, this study derives an analytical expression for the basic reproduction number R_0 , thereby establishing threshold criteria for disease transmission dynamics. The theoretical results are validated through numerical simulations, providing a quantitative assessment tool and a theoretical basis for formulating strategies for epidemic prevention and control. Subsequent studies will prioritize the incorporation of more authentic parameters, the formulation of models such as age structure, and the investigation of the impact of vaccination and antiviral treatment on enhancing the predictive accuracy and public health applicability of these models.

COMPETING INTERESTS

The authors have no relevant financial or non-financial interests to disclose.

REFERENCES

- [1] Xu L, Yue L, Yang X, et al. Research of a Reference Material of Inactivated Influenza A (H1N1) Virus. *Acta Metrologica Sinica*, 2024, 45(2): 294-299.
- [2] He F, Yu H, Liu L, et al. Antigenicity and genetic properties of an Eurasian avian-like H1N1 swine influenza virus in Jiangsu Province, China. *Biosafety and Health*, 2024, 6(6): 319-326.

- [3] KAWANO H, HARUYAMA T, HAYASHI Y, et al. Genetic Analysis and Phylogenetic Characterization of Pandemic (H1N1) 2009 Influenza Viruses that Found in Nagasaki, Japan. *Japanese journal of infectious diseases*, 2011, 64(3): 195-203.
- [4] EDWARD A. PARTLOW, ANNA JAEGGI-WONG, STEVEN D. PLANITZER, et al. Influenza A virus rapidly adapts particle shape to environmental pressures. *Nature Microbiology*, 2025, 10(3): 784-794.
- [5] Zhang Yijie, Meng Fei, Yang Huanliang, et al. Genetic Evolution Analysis of a Strain of H1N1 Subtype Swine Influenza Virus and Evaluation of Its Replication and Droplet Transmission in Ferrets. *Chinese Journal of Preventive Veterinary Medicine*, 2023, 45(10): 987-993.
- [6] Xiao D, Liu J, Jiang T, et al. Transmission restriction and genomic evolution co-shape the genetic diversity patterns of influenza A virus. *Chinese Journal of Virology*, 2024, 39(4): 525-536.
- [7] MALTEZOU HC. Novel (pandemic) influenza A H1N1 in healthcare facilities: implications for prevention and control. *Scandinavian Journal of Infectious Diseases*, 2010, 42(6/7): 412-420.
- [8] SHUAI Z, VAN DEN DRIESSCHE P. Global stability of infectious disease models using lyapunov functions. *SIAM Journal on Applied Mathematics*, 2013, 73(4): 1513-1532.
- [9] Liu T, Zhao Z, Yao M, et al. Establishment and realization of the SEIAR infectious disease dynamics model. *Disease Surveillance*, 2020, 35(10): 934-938.
- [10] VAN DEN DRIESSCHE P, WATMOUGH J. Reproduction numbers and sub-threshold endemic equilibria for compartmental models of disease transmission. *Mathematical Biosciences: An International Journal*, 2002, 180(special issue si): 29-48.
- [11] WANG XIA, CHEN YUMING, SONG XINYU. Global dynamics of a cholera model with age structures and multiple transmission modes. *International journal of biomathematics*, 2019, 12(5).
- [12] ZHANG F, ZHAO XQ. A periodic epidemic model in a patchy environment. *Journal of Mathematical Analysis and Applications*, 2007, 325(1): 496-516.

ANALYSIS OF THE EFFICACY OF TRANSUMBILICAL SINGLE-SITE LAPAROSCOPIC TOTAL EXTRAPERITONEAL TESTICULAR DESCENT FIXATION IN THE TREATMENT OF INGUINAL CRYPTORCHIDISM IN CHILDREN

ZhiFeng Mo^{1#}, Fei Yu^{1#}, BaiYu Zhu¹, MaoLin Liu¹, HanZhong He^{2*}

¹Department of Emergency and Disaster Medical Center, The Seventh Affiliated Hospital, Sun Yat-sen University, Shenzhen 518000, Guangdong, China.

²Children's Medical Center Affiliated to Guangzhou Medical University/Guangzhou Women and Children's Medical Center, Guangzhou 510000, Guangdong, China.

[#]ZhiFeng Mo and Fei Yu contributed equally to this work and they are both first authors.

Corresponding Author: HanZhong He, Email: 13826452429@139.com

Abstract: Objective: To explore the safety and feasibility of transumbilical single-site laparoscopic completely extraperitoneal approach for testicular descent in the treatment of inguinal cryptorchidism in children. Methods: A total of 63 cases of pediatric cryptorchidism treated with transumbilical single-site laparoscopic completely extraperitoneal approach testicular descent fixation (extraperitoneal approach group) from April 2023 to April 2025 were retrospectively analyzed, as well as traditional transumbilical single site surgery during the same period. Site: Clinical data of a total of 64 children who underwent laparoscopic descending testicular fixation (abdominal approach group). The general condition of the children, operation time, intraoperative blood loss, hospitalization time, postoperative complications and other indicators were collected. Results: The surgical procedures of both groups of patients were smooth. There were no surgery-related complications such as testicular retraction, testicular atrophy, or incision infection. One case in the abdominal approach group suffered from choking on milk while eating after surgery, but recovered well after treatment. The average operating time of the extraperitoneal approach group was 62.5 minutes, which was not significantly different from that of the intraperitoneal approach group (the average operating time of the intraperitoneal approach group was 62.75 minutes, $P=0.91$). There was no significant difference in intraoperative blood loss between the two groups ($P=1$). During the postoperative follow-up of 2 to 7 months, no case in the two groups required secondary surgery, and there were no recent postoperative complications. Conclusion: Transumbilical single-site laparoscopic total extraperitoneal approach for the treatment of children with inguinal cryptorchidism by descending testicular fixation has less trauma, less interference with abdominal organs, faster recovery, lower incidence of postoperative complications, and the therapeutic effect is comparable to that of traditional laparoscopic surgery. The effect is equivalent, the efficacy is reliable, and it is worthy of clinical application.

Keywords: Cryptorchidism; Single-port laparoscopy; Extraperitoneal approach; Orchiopexy

1 INTRODUCTION

Cryptorchidism is one of the common congenital genitourinary malformations in pediatric urology. Refers to testes not reaching the scrotum from the abdomen according to normal developmental procedures[1]. Most cryptorchidism declines spontaneously within 3 months of birth, with a significantly reduced chance of decline after 6 months[2]. Clinically, approximately 80% of cryptorchid testes are palpable[3]. Surgery is the gold standard for the treatment of cryptorchidism[1]. With the popularization of minimally invasive techniques in pediatric surgery, the number of laparoscopic orchiopexy procedures has gradually increased, minimally invasive surgery evolved from three ports to a single port, and transumbilical single-port laparoscopic techniques have become increasingly mature[4]. Total extraperitoneal approach is mostly used for adult inguinal hernia repair and other operations, which is characterized by direct access to the preperitoneal space without entering the abdominal cavity for operation to reduce intraoperative injury and the occurrence of postoperative abdominal adhesions[5]. The authors combined the two and first performed transumbilical single-site laparoscopic total extraperitoneal orchiopexy for cryptorchidism. The clinical data of 63 cases of cryptorchidism in children treated with single-port endoscopic orchiopexy via total extraperitoneal approach (extraperitoneal approach group) from April 2023 to April 2025 in our hospital were analyzed and compared with 64 cases treated with laparoscopic surgery via abdominal approach. Reported below.

2 MATERIALS AND METHODS

2.1 General Information

From April 2023 to April 2025, 127 children with unilateral inguinal cryptorchidism were treated in our department, of which 63 underwent transumbilical single-site laparoscopic total extraperitoneal orchiopexy, which was set as the extraperitoneal approach group. Sixty-four patients underwent traditional transumbilical single-site laparoscopic

laparoscopic orchiopexy and were set as the abdominal approach group.

Inclusion criteria:

- (1) Unilateral cryptorchidism;
- (2) Preoperative examination showed empty scrotum;
- (3) Scrotal ultrasound confirmed the presence of the testis and its location above the external ring of the inguinal canal.

Exclusion Criteria:

- (1) Secondary surgery;
- (2) Combined hypospadias, hermaphroditism and other genitourinary system related diseases;
- (3) Ectopic testis, abdominal type testis, retracted testis or sliding testis;

2.2 Surgical Method

Extraperitoneal approach group: A 2-cm arcuate incision was made on the left or right side of the umbilical ring, and the subcutaneous tissue and rectus abdominis muscle were incised to expose the posterior rectus sheath. The space between the posterior rectus sheath and peritoneum was divided to establish the preperitoneal space (Figure 1 single port laparoscopic device was placed connecting the laparoscopic system). Continue dissection down to expose the inferior epigastric artery with the processus vaginalis laterally and the spermatic vessels and vas deferens posteriorly. Ligate and cut the processus vaginalis and free it simultaneously free spermatic vessels and vas deferens (Figure 2-3). The testis was explored and pulled into the preperitoneal space, the spermatic vessels were freed to a sufficient length, and the gubernaculum was cut off (Figure 4-5). A transverse incision of about 1.5 cm was made in the middle of the ipsilateral scrotum, and the skin and flesh membrane were incised to dilate the flesh membrane to form a pocket. Endoscopic dissection forceps separate directly into the scrotal incision from Hy 's triangle in the direction of the scrotum to form a tunnel. The testes were pulled down the tunnel into the scrotal incision and fixed (Figure 6), ensuring no torsion. End procedure.

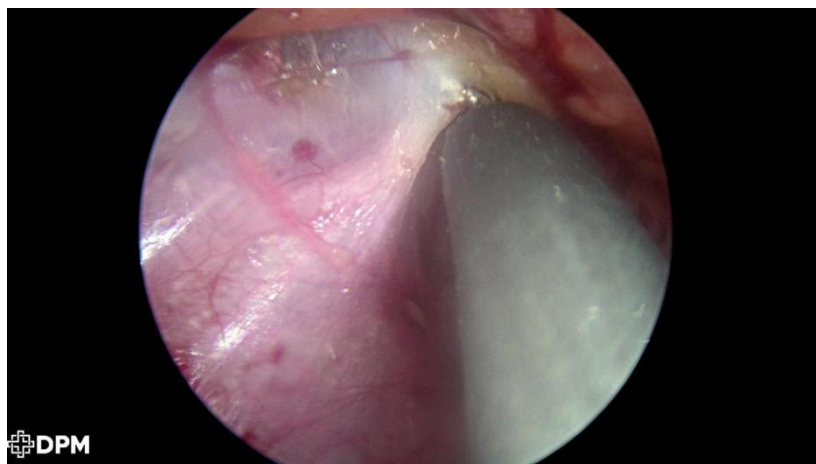


Figure 1 Establishment of the Extraperitoneal Space

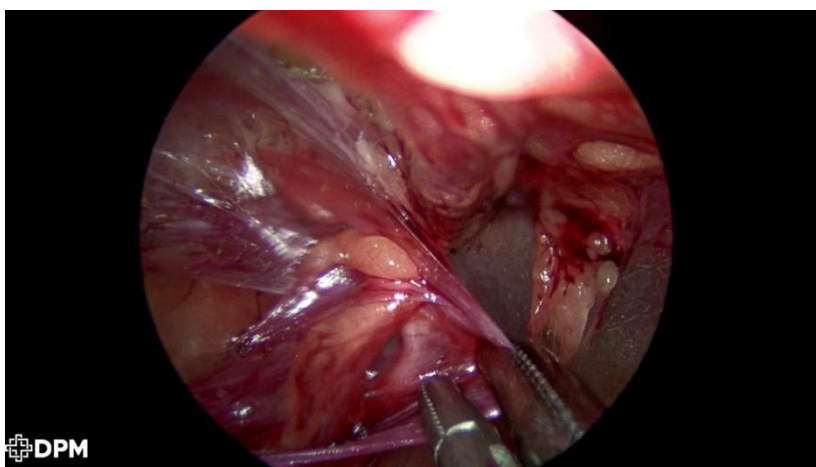


Figure 2 Dissection of the Spermatic Cord Vessels, Vas Deferens and Processus Vaginalis

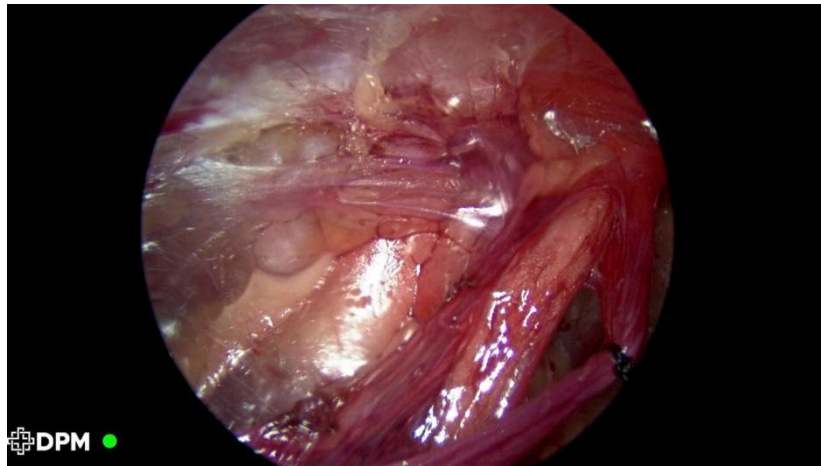


Figure 3 Ligation of the Processus Vaginalis

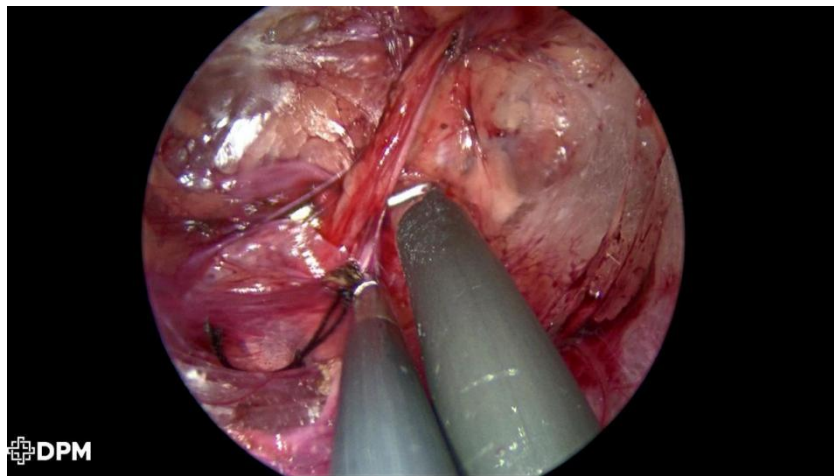


Figure 4 Dissection of the Spermatic Cord Vessels

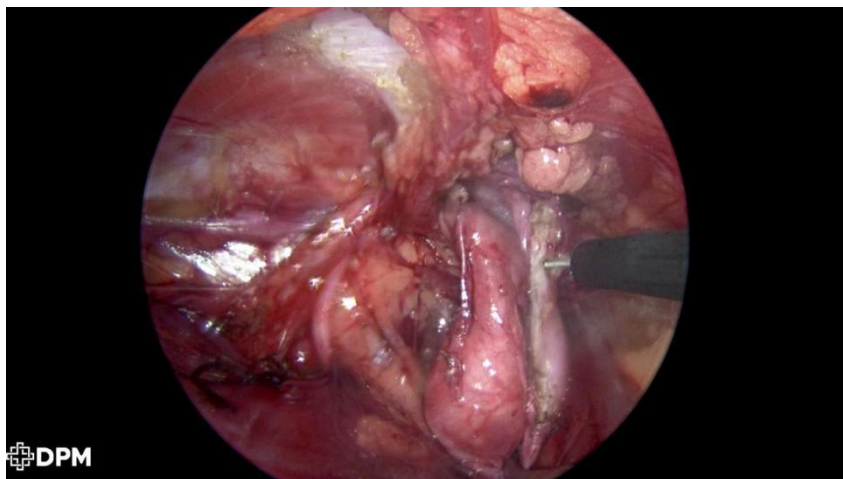


Figure 5 Transection of the Gubernaculum

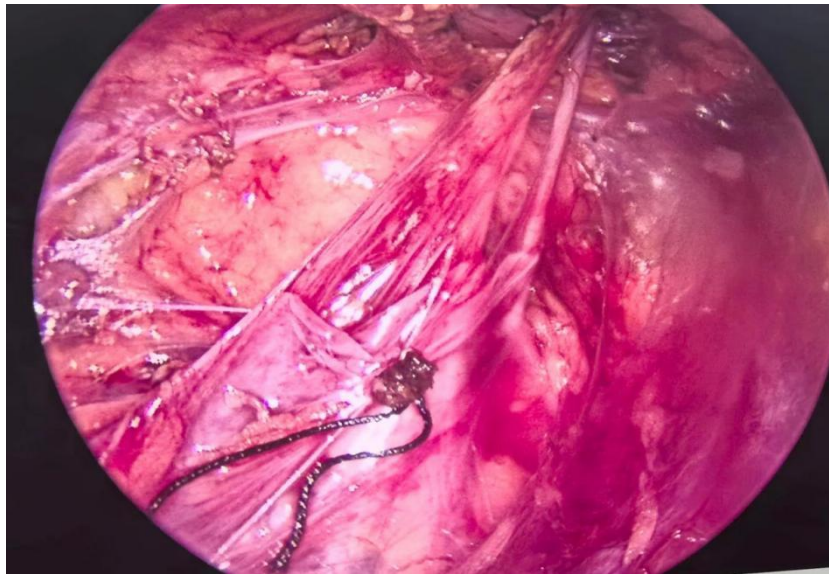


Figure 6 Orchiopexy for Testicular Descent and Fixation

Abdominal approach group: Establish pneumoperitoneum, free processus vaginalis, spermatic vessels and vas deferens, and tunnel orchiopexy through Hy's triangle to scrotal incision.

2.3 Statistical Processing

SPSS 26.0 software was used to process the data. Measurement data ($\bar{x} \pm s$) were analyzed by t test and enumeration data (%) were analyzed by χ^2 test. $P < 0.05$ was considered statistically significant.

3 RESULTS

Both extraperitoneal approach group and abdominal approach group successfully completed the operation, and there was no conversion to open surgery. The mean operation time was 62.5 min in the extraperitoneal approach group and 62.75 min in the abdominal approach group ($P = 0.91$). In the abdominal approach group, there was 1 case of choking milk asphyxia during postoperative feeding, which recovered well after treatment. The patients were followed up for 2-7 months, and none had surgery-related complications like testicular retraction, testicular atrophy or incision infection in the two groups. There were no macroscopically visible surgical scars on the body surface after surgery in either group (Table 1).

The operation was successful in both groups. None had surgery-related complications such as testicular retraction, testicular atrophy, or incision infection. The average operation time of extraperitoneal approach group was 62.5 min, which was not significantly different from that of abdominal approach group (the average operation time of abdominal approach group was 62.75 min, $P = 0.91$). There was no significant difference in intraoperative blood loss between the two groups ($P = 1$).

Table 1 Comparison of the Operation Time between the Two Groups of Patients

Group	Number of subjects (n)	Operative Time (min)
Extraperitoneal group	63	62.50
Abdominal group	64	62.75
T value		0.10
P value		0.92

4 CONCLUSION AND DISCUSSION

Cryptorchidism is one of the most common germline malformations in children and refers to the fact that the testis does not descend to the scrotum after birth and stays on the way to normal descent, that is, stays in the abdominal cavity, inguinal canal, or above the scrotum[6]. The treatment age is recommended to start at 6 months (corrected for gestational age)[7], preferably before 12 months and at least before 18 months[2, 8-9]. Failure to actively lower the

testis to the normal position of the scrotum by surgery can increase the risk of malignant transformation of the testis, infertility, torsion, trauma, and even affect the psychological health of children. About 20% of cryptorchidism is not palpable on the body surface before surgery, but true intra-abdominal cryptorchidism is only 6%, and the rest are located in the groin or scrotum[10]. Commonly used surgical methods for cryptorchidism include inguinal incision orchiopexy, transscrotal incision orchiopexy, and laparoscopic orchiopexy. Simple scrotal incision surgery, the incision is concealed, do not dissect the inguinal canal, but the appropriate syndrome is narrow, need to strictly grasp the indications. Laparoscopic orchiopexy is the best surgical approach for abdominal cryptorchidism[11]. Cortesi first reported that the application of laparoscopic technique in the diagnosis of cryptorchidism[12], with the development of laparoscopic technique, has the advantages of small trauma, beautiful incision, sufficient spermatic cord mobilization, and rapid recovery, and has gradually become the main means of cryptorchidism treatment, especially in the diagnosis and treatment of abdominal or high inguinal cryptorchidism. Because laparoscopic surgery can more thoroughly free the spermatic cord and reduce the probability of fractional surgery, it has become the preferred surgical method for orchiopexy in children. Single-port laparoscopic surgery is increasingly popular because only one incision is at the umbilicus and postoperative scars are more concealed. However, because in single-port laparoscopic surgery, the lens, curved forceps, and coagulating hook all pass through an operating port, the operating space is narrow. And because the devices are blocked from each other, the operator needs a relatively long adaptation time. In the early stages of single-port laparoscopic surgery, the operation time will be longer than that of the traditional three-port method[13]. At present, laparoscopic surgery is used through the abdominal approach, inevitably interfering with the abdominal organs, with the risk of intestinal obstruction and abdominal pain caused by the formation of postoperative adhesions. Laparoscopic total extraperitoneal approach is mostly used for the treatment of adult inguinal hernia, prostate and other diseases, without entering the abdominal cavity, directly entering the preperitoneal space for operation, effectively avoiding abdominal surgery-related complications[5]. In the control intraperitoneal group, there was one case of choking milk asphyxia after surgery, while there were no postoperative complications in the extraperitoneal group. There was no difference with the intraperitoneal approach in terms of mobilization of the spermatic vessels and vas deferens. Moreover, ligation and transection of the processus vaginalis via an extraperitoneal approach reduces the risk of postoperative complications of indirect inguinal hernia or hydrocele.

In single-port endoscopic orchiopexy for extraperitoneal approach, the experience of this procedure in practice is as follows: (1) The real operating space in the total extraperitoneal approach surgical approach is not between the deep and superficial layers of the transversalis fascia, but between the superficial layer of the transversalis fascia and the peritoneum, the deep layer of the transversalis fascia needs to be incised to enter the preperitoneal space. (2) Gentle operation and careful identification, the space between the posterior rectus sheath and the peritoneum is small at the initial stage and the operating space can be increased by blunt dissection of the fingers, directly to the semilunar line. (3) When freeing the processus vaginalis, more delicate procedures should be performed to avoid perforating the peritoneum. Otherwise, air enters the abdominal cavity, which greatly reduces the extraperitoneal space. Access to the abdominal cavity may be changed if necessary.

In conclusion, totally extraperitoneal single-port endoscopic orchiopexy, as a new surgical method, has definite effect, has the significant advantages of reducing abdominal trauma, reducing abdominal organ harassment, cosmetic appearance of the surgical incision, and can achieve the same surgical effect as traditional laparoscopy, which is worthy of clinical promotion. However, this study still has shortcomings such as short duration of development, small number of cases, and lack of long-term follow-up results, which still need to be further improved.

COMPETING INTERESTS

The authors have no relevant financial or non-financial interests to disclose.

REFERENCE

- [1] Urology Group. Society of Pediatric Surgery, Chinese Medical Association. Expert Consensus on the Diagnosis and Treatment of Cryptorchidism. Chinese Journal of Pediatric Surgery, 2018, 39(07): 484-487. DOI: 10.3760/cma.j.issn.0253-3006.2018.07.002.
- [2] Kolon T F, Herndon C D, Baker L A, et al. Evaluation and treatment of cryptorchidism: AUA guideline. The Journal of Urology, 2014, 192(2): 337-345. DOI: 10.1016/j.juro.2014.05.005.
- [3] Niu Zhishang, Hao Chunsheng, Bai Dongsheng, et al. Efficacy Observation of Transumbilical Single-site Multichannel Laparoscopic Fowler-Stephens Staged Surgery for High Cryptorchidism in Children. Chinese Journal of Pediatric Surgery, 2021, 42(11): 999-1003. DOI: 10.3760/cma.j.cn421158-20200518-00348.
- [4] Markar S R, Karthikesalingam A, Thrumurthy S, et al. Single-incision laparoscopic surgery (SILS) vs. conventional multiport cholecystectomy: systematic review and meta-analysis. Surg Endosc, 2012, 26(5): 1205-1213. DOI: 10.1007/s00464-011-2051-0.
- [5] Zhang Chenbo, Li Jianwen. Operating Techniques of Laparoscopic Totally Extraperitoneal Inguinal Hernia Repair. International Journal of Surgery, 2013, 40(09): 641-643, F0004. DOI: 10.3760/cma.j.issn.1673-4203.2013.09.023.
- [6] Wang C Y, Wang Y, Chen X H, et al. Efficacy of single-stage and two-stage Fowler-Stephens laparoscopic orchidopexy in the treatment of intraabdominal high testis. Asian journal of surgery, 2017, 40(6): 490-494. DOI: 10.1016/j.asjsur.2016.11.008.

- [7] Wei Y, Wu S D, Wang Y C, et al. A 22-year retrospective study: educational update and new referral pattern of age at orchidopexy. *BJU international*, 2016, 118(6): 987-993. DOI:10.1111/bju.13588.
- [8] Radmayr C, Dogan H S, Hoebcke P, et al. Management of undescended testes: European Association of Urology/European Society for Paediatric Urology Guidelines. *Journal of pediatric urology*, 2016, 12(6): 335-343. DOI: 10.1016/j.jpuro.2016.07.014.
- [9] Braga L H, Lorenzo A J, Romao R L P. Canadian Urological Association-Pediatric Urologists of Canada (CUA-PUC) guideline for the diagnosis, management, and followup of cryptorchidism. *Canadian Urological Association journal = Journal de l'Association des urologues du Canada*, 2017, 11(7): E251-e260. DOI: 10.5489/cuaj.4585.
- [10] Barthold J S, González R. The epidemiology of congenital cryptorchidism, testicular ascent and orchiopexy. *The Journal of urology*, 2003, 170(6 Pt 1): 2396-2401. doi:10.1097/01.ju.0000095793.04232.d8
- [11] Bao Qiao, Li Ning, Zhou Xuefeng, et al. Experience in the Selection of Different Surgical Approaches for Orchiopexy. *Chinese Journal of Endoscopic Urology (Electronic Edition)*, 2017, 11(03): 166-169. DOI: 10.3877/cma.j.issn.1674-3253.2017.03.006
- [12] Cortesi N, Ferrari P, Zambarda E, et al. Diagnosis of bilateral abdominal cryptorchidism by laparoscopy. *Endoscopy*, 1976, 8(1): 33-34. DOI: 10.1055/s-0028-1098372.
- [13] Wang Li, Li Guibin, Song Lianjie, et al. Efficacy Analysis of Transumbilical Single-site Laparoscopic Treatment of Cryptorchidism in Children. *Chinese Journal of Pediatric Surgery*, 2016, 37(12): 928-931. DOI: 10.3760/cma.j.issn.0253-3006.2016.12.011.

CIGARETTE SMOKE EXTRACT PROMOTES APOPTOSIS OF HUMAN PULMONARY ARTERIAL ENDOTHELIAL CELLS VIA THE ER STRESS CHOP SIGNALING PATHWAY

Mo Liang^{1#}, LiLe Wang^{1#}, Mo Xiao², Bo Chen¹, Jie Li¹, RuiCheng Hu^{1*}

¹Hunan Provincial People's Hospital (The First Affiliated Hospital of Hunan Normal University), Changsha 410005, Hunan, China.

²Ningxiang People's Hospital, Ningxiang 410600, Hunan, China.

[#]Mo Liang and LiLe Wang are co-first authors.

Corresponding Author: RuiCheng Hu, Email: huruicheng@hotmail.com

Abstract: Objective: To determine whether cigarette smoke promotes apoptosis of human pulmonary artery endothelial cells (HPAECs) via the CCAAT/enhancer-binding protein homologous protein (CHOP) signaling pathway, and whether 4-phenylbutyric acid (4-PBA) has an inhibitory effect on this apoptosis. **Methods:** CHOP gene expression in HPAECs was silenced by lentiviral transfection of recombinant RNA. Both wild-type and CHOP-silenced HPAECs were divided into four groups: control group (Col group), cigarette smoke extract group (CSE group, with 10% CSE added to the medium), PBA group (PBA group, with 5 mmol/L PBA added to the medium), and CSE + PBA group (with both 10% CSE and 5 mmol/L PBA added to the medium). Cells were treated for 6, 12, and 24 hours. Endoplasmic reticulum morphology was observed by transmission electron microscopy, and cell apoptosis was analyzed by flow cytometry. CHOP protein and mRNA expression levels were detected by Western blot and real-time PCR, respectively. **Results:** CSE induced apoptosis in HPAECs, and the mechanism was associated with the CHOP-mediated apoptosis signaling pathway. 4-PBA reduced CSE-induced apoptosis in HPAECs. **Conclusion:** Cigarette smoke extract can induce apoptosis in HPAECs through the CHOP signaling pathway, and 4-PBA can attenuate this effect.

Keywords: Human pulmonary artery endothelial cells; Endoplasmic reticulum stress; ER stress-induced apoptosis; CCAAT/enhancer-binding protein homologous protein; 4-phenylbutyric acid

INTRODUCTION

Chronic obstructive pulmonary disease (COPD) is a common and frequently occurring disease that can ultimately lead to loss of working capacity and death. Cigarette smoke (CS) can induce apoptosis of pulmonary vascular endothelial cells and alveolar epithelial cells through endoplasmic reticulum stress (ERS) [1], thereby promoting the development and progression of COPD [2]. The CCAAT/enhancer-binding protein homologous protein (CHOP) is upregulated during ERS [3] and serves as a marker protein of ERS [4]. 4-Phenylbutyric acid (4-PBA), an ERS inhibitor [5], can reduce ERS activation [6] and pulmonary vascular remodeling [7], and prevent pulmonary hypertension [5]. Therefore, we hypothesize that 4-PBA may affect apoptosis of pulmonary vascular endothelial cells by modulating CHOP expression. In this study, we established an in vitro lentiviral CHOP-silenced human pulmonary artery endothelial cell (HPAEC) model. We observed the changes in endoplasmic reticulum morphology, apoptosis ratio, and expression levels of CHOP protein and mRNA in both wild-type HPAECs and CHOP-silenced HPAECs (HPAECs-CHOP) after exposure to CSE for different durations. The aim was to determine whether CSE promotes HPAEC apoptosis through the CHOP signaling pathway and whether 4-PBA has an inhibitory effect on this process, providing new insights for the treatment of COPD.

1 MATERIALS AND METHODS

1.1 Materials

HPAECs were purchased from ScienCell Research Laboratories (USA). Furong-brand cigarettes (12 mg tar/cigarette, 1.0 mg nicotine/cigarette) were produced by Hunan China Tobacco Industry Co., Ltd. The cell apoptosis detection kit was obtained from Shanghai Yisheng Biotechnology Co., Ltd. Lentiviruses were purchased from Shanghai GeneChem Co., Ltd. 4-Phenylbutyric acid (4-PBA) was obtained from Sigma (USA). The transmission electron microscope was produced by Tianmei Scientific Instrument Co., Ltd. (China). The BCA protein assay kit, Trizol reagent, reverse transcription kits, and miRNA reverse transcription kits were purchased from Kangwei Century Biotechnology Co., Ltd. (Beijing, China). Mouse anti-, rabbit anti-, normal goat serum, mouse monoclonal anti-CD31 antibody, horse anti-mouse, and goat anti-rabbit secondary antibodies were all obtained from Proteintech (USA). Primers were synthesized by Sangon Biotech (Shanghai). The upstream primer sequence for β -actin was 5'-ACCCTGAAGTACCCCATCGAG-3', and the downstream primer was 5'-AGCACAGCCTGGATAGCAAC-3'. The upstream primer for CHOP was 5'-ATTGCCTTTCTCCTTCGGGACA-3', and the downstream primer was 5'-CTCCTCAGTCAGCCAAGCC-3'.

1.2 Preparation of Cigarette Smoke Extract

The preparation of cigarette smoke extract (CSE) was conducted following the methods described in studies [8, 9]. Unfiltered cigarettes were connected to a three-way tube, which was linked on one end to a sealed flask containing 5 mL of phosphate-buffered saline (PBS), and on the other end to a 50 mL syringe. Cigarette smoke was drawn into the flask at a rate of 35 mL per 2 seconds per draw, with 1-minute intervals between each draw, for a total of 10 draws. The flask was shaken to ensure full dissolution of the smoke, resulting in a 100% CSE suspension. The suspension was adjusted to pH 7.4 using 1 mol/L NaOH, sterilized by filtration through a 0.22 μ m pore-size filter, and then diluted with serum-free 1640 medium to a final concentration of 10% CSE. The prepared CSE was used in experiments within 30 minutes.

1.3 Cell Culture and Identification

(1) HPAECs were cultured in complete medium at 37 °C in a humidified incubator with 5% CO₂ until the cells reached approximately 80% confluency. Cells were then digested with trypsin and passaged at a 1:2 ratio.

(2) Immunohistochemical identification of HPAECs: Coverslips were prepared using logarithmic-phase HPAECs. When the cells on the coverslips reached about 80% confluency, they were rinsed three times with PBS and fixed with acetone for 15 minutes. Non-specific antigens were blocked with 5% goat serum. Primary antibodies were incubated overnight at 4 °C: mouse monoclonal anti-CD31 antibody (1:100) and rabbit anti-human von Willebrand factor (vWF) antibody (1:600). After three PBS washes, biotin-labeled secondary antibodies (horse anti-mouse and goat anti-rabbit, 1:200) were added and incubated at room temperature for 1 hour. DAB (0.05%) was used for color development. The cells were observed and photographed under an inverted microscope.

1.4 Lentiviral Transfection

HPAECs were incubated in complete culture medium for 24 hours. Once the cells adhered and entered the logarithmic growth phase, the medium was discarded and the cells were rinsed twice with sterile PBS. Cells were then infected with the virus for 8 hours. After infection, the medium was replaced with fresh complete medium, and the cells were cultured for an additional 72 hours before being harvested. CHOP protein expression levels were assessed by Western blot. The cells with the highest transfection efficiency were selected for subsequent experiments.

1.5 Transmission Electron Microscopy Observation of Endoplasmic Reticulum Morphology

Treated HPAECs and HPAECs-CHOP were fixed in 2.5% glutaraldehyde solution for 10 hours. After discarding the fixative, the cells were placed in PBS buffer for 3 hours, followed by post-fixation in 1% osmium tetroxide for 1 hour. The cells were then dehydrated sequentially in 30% ethanol, 50% ethanol, 70% ethanol containing uranyl acetate, 80% ethanol, 95% ethanol, and 100% ethanol for 10 minutes, 15 minutes, 2 hours, 10 minutes, 15 minutes, and 45 minutes, respectively. Samples were embedded in pure epoxy resin and polymerized at 40 °C and 60 °C for 24 hours each. Ultrathin sections of 70 nm were cut, mounted on copper grids, and stained. Endoplasmic reticulum morphology was observed under a Hitachi HT7700 transmission electron microscope at 5000 \times magnification.

1.6 Flow Cytometry Analysis of Cell Apoptosis

Cells from each group were collected by centrifugation to obtain cell suspensions. Cells were washed twice with PBS, centrifuging at 2000 rpm for 5 minutes each time to remove PBS. The cells were then fixed in pre-cooled 70% ethanol at 4 °C for 1 hour. After centrifugation to discard the fixative, 3 mL of PBS was added to resuspend the cells for 5 minutes. The suspension was filtered once through a 400-mesh sieve, followed by centrifugation at 500–1000 rpm for 5 minutes. PBS was removed, and approximately $1-5 \times 10^5$ cells were collected. The cells were then sequentially resuspended in 500 μ L of binding buffer and mixed with 5 μ L of Annexin V-FITC. Next, 5 μ L of propidium iodide (PI) was added and mixed thoroughly. The samples were incubated in the dark for 15 minutes and analyzed by flow cytometry within 1 hour to detect fluorescence expression in cells.

1.7 Western Blot Detection of CHOP Protein Expression

Proteins were extracted using a total protein extraction kit according to the manufacturer's instructions. Protein concentrations were determined using a BCA protein assay kit following the provided protocol. Western blotting was performed strictly according to standard procedures. Primary antibodies were diluted as follows: CHOP antibody at 1:200 and incubated at room temperature for 90 minutes. Secondary antibodies were diluted at 1:5000 for mouse antibodies and 1:6000 for rabbit antibodies, with incubation at room temperature for 80 minutes. After incubation with ECL chemiluminescent substrate, the membranes were sealed with plastic wrap, exposed, developed, and washed.

1.8 Statistical Analysis

Data analysis was performed using GraphPad Prism 8.0 software. Data are presented as mean \pm standard deviation

($\bar{X} \pm SD$). Comparisons between groups were conducted using independent samples t-test or one-way analysis of variance (ANOVA). A p-value of less than 0.05 was considered statistically significant.

2 RESULTS

2.1 Identification of Human Pulmonary Arterial Endothelial Cells

Under the inverted phase-contrast microscope, the cells appeared polygonal or spindle-shaped with clear boundaries. The nuclei were round or oval, with visible nucleoli. The cytoplasm was abundant and contained small granules. The cells grew as a confluent monolayer arranged in a cobblestone-like pattern. Immunohistochemical staining for CD31 and vWF showed nuclei stained blue, while positive signals appeared as varying shades of brown. Over 90% of the cells were positive, confirming that the cultured cells were human pulmonary artery endothelial cells.

2.2 Verification of Lentiviral CHOP Silencing

The infection efficiency of HPAECs was observed under a fluorescence microscope. Cells successfully infected by the lentivirus emitted green fluorescence. Infection efficiency was calculated as the ratio of green fluorescent cells to total cells multiplied by 100%. The results showed an infection efficiency greater than 90%, indicating successful lentiviral transfection.

2.3 Measurement of CHOP Protein Expression in Human Pulmonary Arterial Endothelial Cells after CHOP Silencing

Western blot was used to detect CHOP protein expression levels in different groups of HPAECs after successful lentiviral transfection. The Chop-shRNA#3 group showed significantly lower CHOP protein levels compared to the Chop-shRNA#1 and Chop-shRNA#2 groups ($P < 0.05$), therefore Chop-shRNA#3 was selected for subsequent experiments (Figure 1).

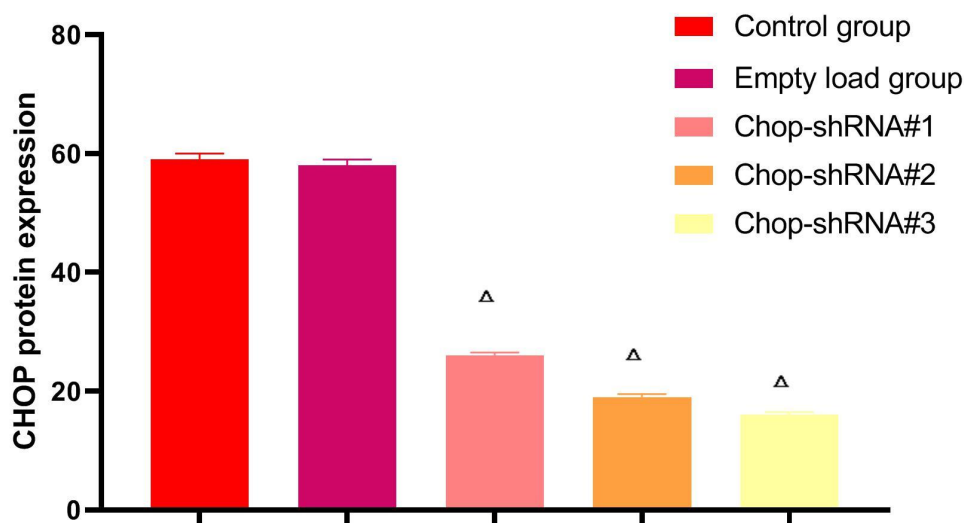


Figure 1 CHOP Protein Expression Levels in Each Group of HPAECs after Lentiviral Interference

Note: Δ $P < 0.01$ vs. Control group; \blacktriangle $P < 0.05$ vs. Chop-shRNA#3

2.4 Transmission Electron Microscopy Observation of Endoplasmic Reticulum Morphology

After 24 hours of treatment under different conditions: In wild-type HPAECs, the control (Col) group and the PBA group showed normal morphology. The CSE group exhibited obvious endoplasmic reticulum (ER) swelling, characterized mainly by enlarged volume and flattened, lighter folds. In the CSE + PBA group, ER swelling was alleviated compared to the CSE group. In HPAECs-CHOP, the Col, PBA, and CSE + PBA groups displayed basically normal morphology. The CSE group showed increased electron density of the ER membrane without significant swelling and retained normal folded structures.

2.5 Western Blot Analysis of CHOP Protein Expression Levels

At the same treatment time, there was no significant difference between the PBA group and the Col group in both wild-type HPAECs and HPAECs-CHOP groups. The CSE group showed higher levels than both the Col group and the

CSE+PBA group, while the CSE+PBA group was higher than the Col group. Comparing different treatment times within wild-type HPAECs groups, results at 24 hours were higher than those at 12 hours, and results at 12 hours were higher than those at 6 hours. No significant differences were observed among the HPAECs-CHOP groups. Under the same treatment conditions, the apoptosis rate and CHOP protein expression levels in wild-type HPAECs were higher than those in HPAECs-CHOP. The increase in measured parameters in the wild-type HPAECs CSE group compared to the HPAECs-CHOP CSE+PBA group was more pronounced, exceeding the increase seen between the wild-type HPAECs CSE group and the HPAECs-CHOP CSE group, and also greater than the difference between the wild-type HPAECs CSE group and the wild-type HPAECs CSE+PBA group (Figures 2–7).

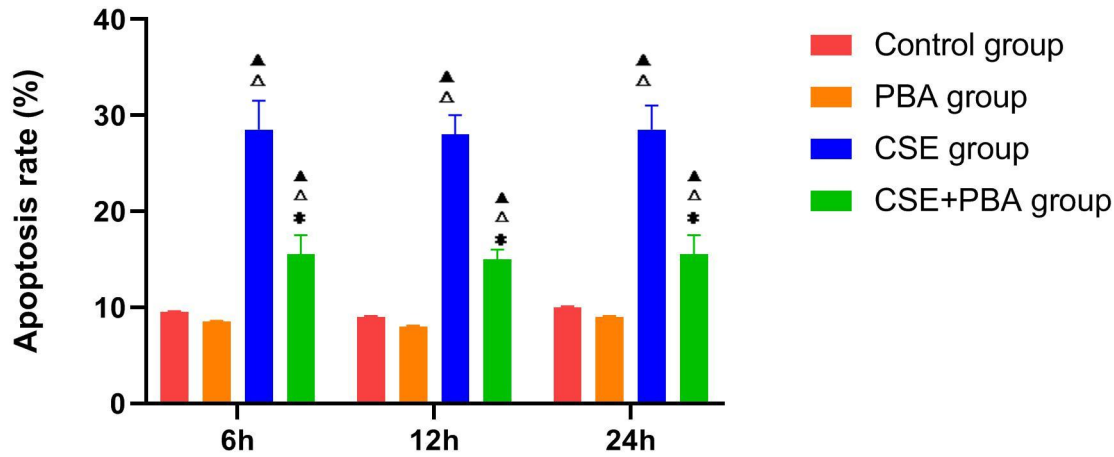


Figure 2 Apoptosis Rates of Wild-type HPAECs at Different Time Points under Various Treatments

Note: ▲P < 0.05 vs. Col group; △P < 0.05 vs. PBA group; *P < 0.05 vs. CSE group

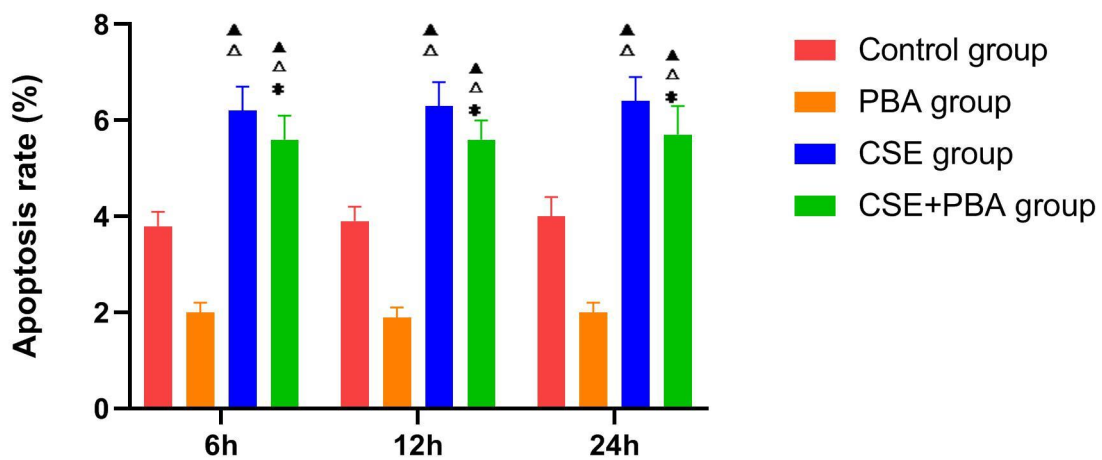


Figure 3 Apoptosis Rates of HPAECs-CHOP at Different Time Points under Various Treatments

Note: ▲P < 0.05 vs. Col group; △P < 0.05 vs. PBA group; *P < 0.05 vs. CSE group

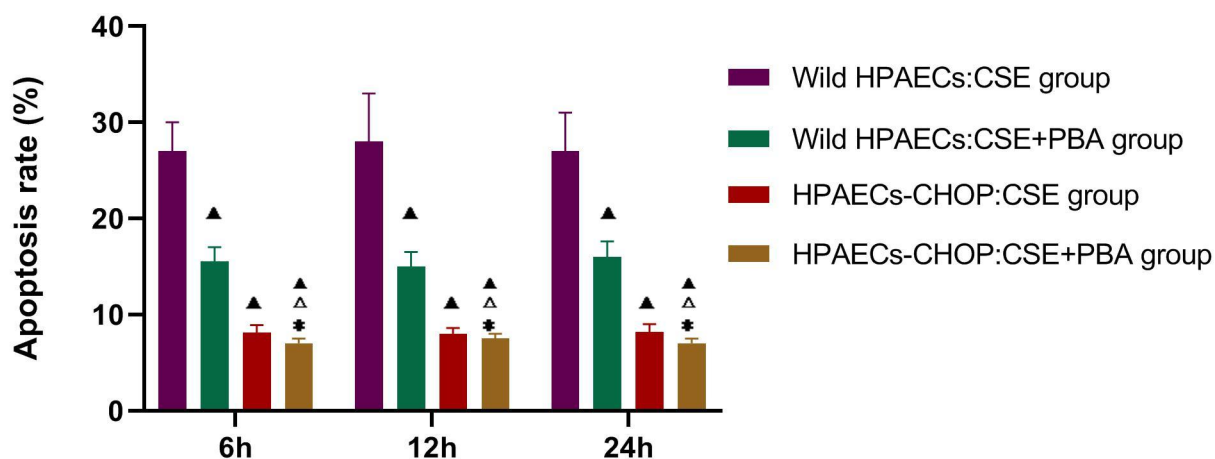


Figure 4 Apoptosis Rates of Wild-type HPAECs and HPAECs-CHOP at Different Time Points under Various Treatments

Note: ▲P < 0.05 vs. Wild-type CSE group; △P < 0.05 vs. Wild-type CSE+PBA group; *P < 0.05 vs. HPAECs-CHOP CSE group

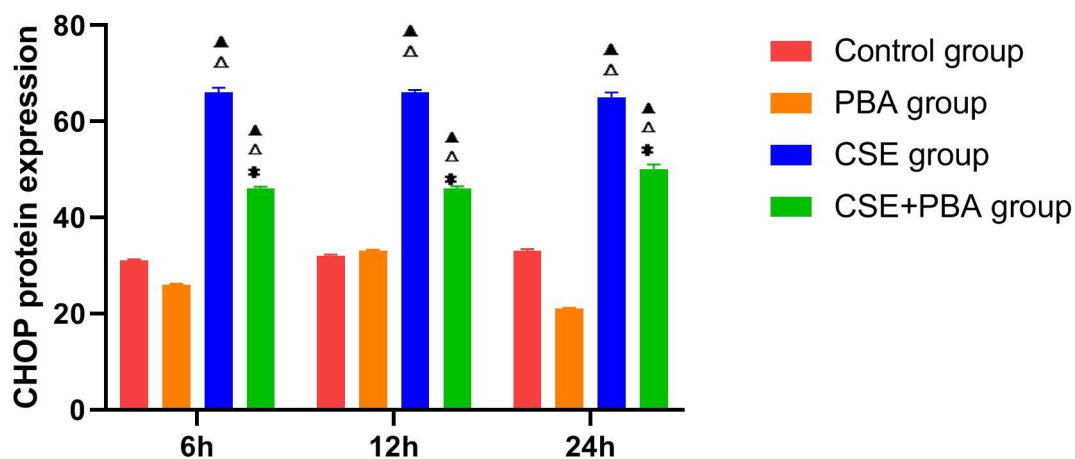


Figure 5 CHOP Protein Expression Levels in Wild-type HPAECs at Different Time Points under Various Treatments

Note: ▲P < 0.05 vs. Col group; △P < 0.05 vs. PBA group; *P < 0.05 vs. CSE group

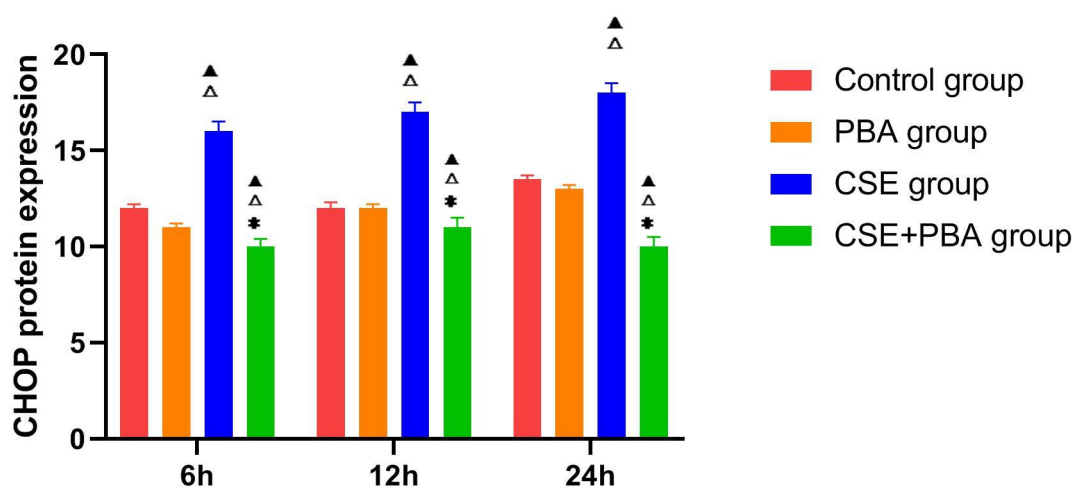


Figure 6 CHOP Protein Expression Levels in HPAECs-CHOP at Different Time Points under Various Treatments

Note: ▲P < 0.05 vs. Col group; △P < 0.05 vs. PBA group; *P < 0.05 vs. CSE group

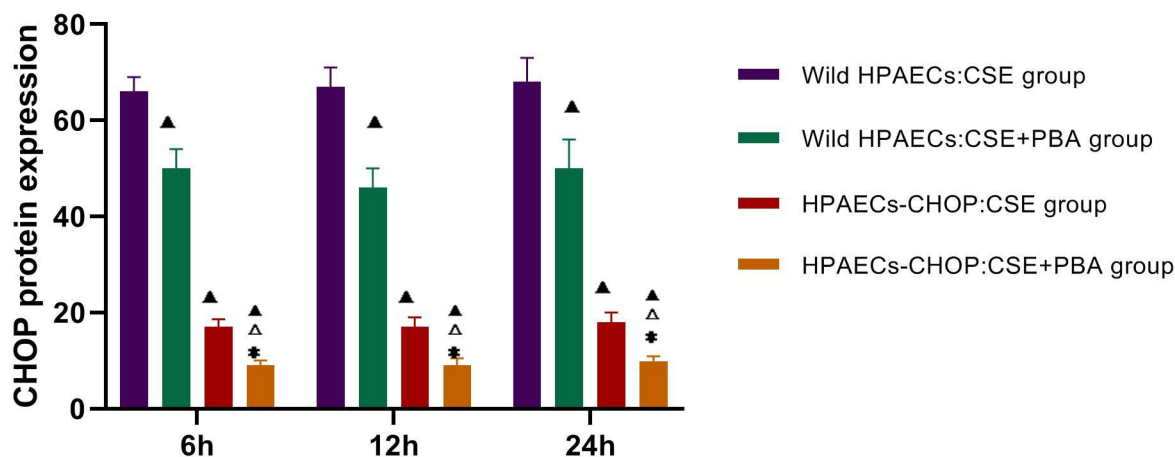


Figure 7 CHOP Protein Expression Levels in Wild-type HPAECs and HPAECs-CHOP at Different Time Points under Various Treatments

Note: ▲P < 0.05 vs. Wild-type CSE group; △P < 0.05 vs. Wild-type CSE+PBA group; *P < 0.05 vs. HPAECs-CHOP CSE group

3 DISCUSSION

Chronic obstructive pulmonary disease (COPD) is a common disease, and smoking is an important risk factor. Cigarette smoke (CS) induces endoplasmic reticulum stress (ERS) in vascular endothelial cells and smooth muscle cells, leading to dysfunction, which may be the initiating factor in the pathological changes of COPD complicated by pulmonary arterial hypertension [10, 11].

Endoplasmic reticulum stress (ERS) is a cellular response mechanism to various pathological and physiological stimuli. Under different stress conditions, the degradation of misfolded and unfolded proteins in the endoplasmic reticulum increases. However, if the stimulus is too intense or prolonged, the endoplasmic reticulum fails to restore normal function, and the cell initiates apoptosis, leading to ERS-induced cell apoptosis [12, 13]. In an in vitro model of HPAECs with lentiviral-mediated CHOP silencing, ultrastructural damage was observed in wild-type HPAECs treated with CSE. The cytoplasm and endoplasmic reticulum were significantly swollen, characterized mainly by increased volume, decreased density, increased rough endoplasmic reticulum, and flattened, lighter ER folding structures. These findings indicate that CSE induces ERS in HPAECs. In contrast, the endoplasmic reticulum morphology in HPAECs-CHOP groups was basically normal. Although the ER membrane electron density increased in the HPAECs-CHOP CSE group, the ER maintained normal folded structures. This suggests that silencing CHOP alleviates CSE-induced ER stress and prevents apoptosis in HPAECs.

A large body of evidence indicates that ERS-induced apoptosis primarily occurs through the following pathways: the apoptosis signal-regulating kinase 1 (ASK1)-JNK signaling pathway, the caspase-12 signaling pathway, and the CHOP signaling pathway [14, 15]. CHOP is a downstream target of ERS [16], with very low expression under physiological conditions, but it is significantly upregulated during ERS and participates in regulating the expression of apoptosis-related genes [17]. In this study, exposure of wild-type HPAECs to CSE resulted in increased apoptosis rates and elevated CHOP mRNA and protein expression levels in a time-dependent manner, suggesting that CSE may promote HPAEC apoptosis by upregulating CHOP expression. Under the same treatment conditions, HPAECs-CHOP exhibited lower apoptosis rates than wild-type cells, indicating that CHOP silencing can alleviate ERS severity in HPAECs and thereby reduce apoptosis.

4-Phenylbutyric acid (4-PBA), a molecular chaperone, is an inhibitor of endoplasmic reticulum stress (ERS) [18]. It can alleviate the severity of ERS by promoting proper protein folding and other mechanisms. In this study, HPAECs treated with 4-PBA showed basically normal endoplasmic reticulum morphology, and the rates of apoptosis as well as CHOP mRNA and protein expression levels were lower compared to cells treated with CSE alone. These results suggest that 4-PBA can prevent apoptosis in HPAECs by mitigating the severity of CSE-induced ERS, consistent with previous reports that 4-PBA protects various cells from apoptosis by reducing ERS [19, 20]. Moreover, this also indicates that 4-PBA may reduce CHOP expression levels [21], thereby decreasing ERS-induced apoptosis in HPAECs.

This study demonstrated at the cellular level that cigarette smoke extract (CSE) promotes apoptosis of human pulmonary arterial endothelial cells (HPAECs) through the CHOP signaling pathway, and that 4-phenylbutyric acid (4-PBA) exerts an anti-apoptotic effect. Moreover, silencing CHOP expression and 4-PBA intervention have a synergistic effect in alleviating endoplasmic reticulum stress (ERS) and reducing cell apoptosis. However, a limitation of this study is that other protein expression levels involved in ERS-induced apoptotic signaling pathways were not examined in the isolated cell experiments, making it impossible to fully assess changes in other relevant factors in the ERS-induced apoptotic pathways of wild-type HPAECs and HPAECs-CHOP under CSE exposure.

4 CONCLUSION

Cigarette smoke extract (CSE) can induce apoptosis in human pulmonary arterial endothelial cells (HPAECs), and this mechanism is related to the CHOP signaling pathway; 4-phenylbutyric acid (4-PBA) can reduce CSE-induced apoptosis in HPAECs.

COMPETING INTERESTS

The authors have no relevant financial or non-financial interests to disclose.

FUNDING

This study was funded by the Hunan Provincial Clinical Medical Technology Innovation Project (2021SK50905).

REFERENCES

- [1] Xue H, Xie B, Xu N, et al. Etanercept protected against cigarette smoke extract-induced inflammation and apoptosis of human pulmonary artery endothelial cells via regulating TNFR1. *International Journal of Chronic Obstructive Pulmonary Disease*, 2021, 16: 1329–1345.
- [2] Sakhatskyy P, Gabino Miranda GA, Newton J, et al. Cigarette smoke-induced lung endothelial apoptosis and emphysema are associated with impairment of FAK and eIF2 α . *Microvascular Research*, 2014, 94: 80–89.
- [3] Tian Y, Wang L, Qiu Z, et al. Autophagy triggers endoplasmic reticulum stress and C/EBP homologous protein-mediated apoptosis in OGD/R-treated neurons in a caspase-12-independent manner. *Journal of Neurophysiology*, 2021, 126(5): 1740–1750.
- [4] Bahar E, Kim H, Yoon H. ER stress-mediated signaling: Action potential and Ca(2+) as key players. *International Journal of Molecular Sciences*, 2016, 17(9): 1558.
- [5] Koyama M, Furuhashi M, Ishimura S, et al. Reduction of endoplasmic reticulum stress by 4-phenylbutyric acid prevents the development of hypoxia-induced pulmonary arterial hypertension. *American Journal of Physiology - Heart and Circulatory Physiology*, 2014, 306(9): H1314–H1323.
- [6] Delmotte P, Yap JQ, Dasgupta D, et al. Chemical chaperone 4-PBA mitigates tumor necrosis factor alpha-induced endoplasmic reticulum stress in human airway smooth muscle. *International Journal of Molecular Sciences*, 2023, 24(21): 15816.
- [7] Wu Y, Adi D, Long M, et al. 4-Phenylbutyric acid induces protection against pulmonary arterial hypertension in rats. *PLoS One*, 2016, 11(6): e0157538.
- [8] Meng S, Liu K, Li X, et al. Melatonin ameliorates PM2.5-induced airway inflammation and apoptosis by PERK/eIF2 α /ATF4/CHOP in chronic obstructive pulmonary disease mice. *Toxicology and Applied Pharmacology*, 2025, 499: 117314.
- [9] Zhang S, Duan H, Yan J. Identifying biomarkers of endoplasmic reticulum stress and analyzing immune cell infiltration in chronic obstructive pulmonary disease using machine learning. *Frontiers in Medicine*, 2024, 11: 1462868.
- [10] Weissmann N, Langbein L, Pichl A, et al. Stimulation of soluble guanylate cyclase prevents cigarette smoke-induced pulmonary hypertension and emphysema. *American Journal of Respiratory and Critical Care Medicine*, 2014, 189(11): 1359–1373.
- [11] Wang J, Chen Y, Lin C, et al. Effects of chronic exposure to cigarette smoke on canonical transient receptor potential expression in rat pulmonary arterial smooth muscle. *American Journal of Physiology - Cell Physiology*, 2014, 306(4): C364–C373.
- [12] Iurlaro R, Muñoz-Pinedo C. Cell death induced by endoplasmic reticulum stress. *FEBS Journal*, 2016, 283(14): 2640–2652.
- [13] Manni S, Brancalion A, Tubi LQ, et al. Protein kinase CK2 protects multiple myeloma cells from ER stress-induced apoptosis and from the cytotoxic effect of HSP90 inhibition through regulation of the unfolded protein response. *Clinical Cancer Research*, 2012, 18(7): 1888–1900.
- [14] Qian Z, Zhu L, Li Y, et al. Icarrin prevents cardiomyocyte apoptosis in spontaneously hypertensive rats by inhibiting endoplasmic reticulum stress pathways. *Journal of Pharmacy and Pharmacology*, 2021, 73(8): 1023–1032.
- [15] Hang L, Peng Y, Xiang R, et al. Ox-LDL causes endothelial cell injury through ASK1/NLRP3-mediated inflammasome activation via endoplasmic reticulum stress. *Drug Design, Development and Therapy*, 2020, 14: 731–744.
- [16] Hu H, Tian M, Ding C, et al. The C/EBP homologous protein (CHOP) transcription factor functions in endoplasmic reticulum stress-induced apoptosis and microbial infection. *Frontiers in Immunology*, 2018, 9: 3083.
- [17] Yang Z, Wu S, Zhao J, et al. Emulsified isoflurane protects beta cells against high glucose-induced apoptosis via inhibiting endoplasmic reticulum stress. *Annals of Palliative Medicine*, 2020, 9(1): 90–97.
- [18] Pao HP, Liao WI, Tang SE, et al. Suppression of endoplasmic reticulum stress by 4-PBA protects against hyperoxia-induced acute lung injury via up-regulating claudin-4 expression. *Frontiers in Immunology*, 2021, 12: 674316.
- [19] Li J, Yang K, Du S, et al. ER stress mediated by GRP-78/PERK/CHOP signaling is involved in fluoride-induced ameloblast apoptosis. *Biological Trace Element Research*, 2024, 202(3): 1103–1114.

- [20] Xu W, Shen Y. Curcumin affects apoptosis of colorectal cancer cells through ATF6-mediated endoplasmic reticulum stress. *Chemistry and Biodiversity - Drug Design*, 2024, 103(1): e14433.
- [21] Zhu M, Jiang Y, Wu H, et al. Gambogic acid shows anti-proliferative effects on non-small cell lung cancer (NSCLC) cells by activating reactive oxygen species (ROS)-induced endoplasmic reticulum (ER) stress-mediated apoptosis. *Medical Science Monitor*, 2019, 25: 3983–3988.

COMMON SOIL-BORNE PATHOGENIC DISEASES IN AMERICAN GINSENG (*PANAX QUINQUEFOLIUS*) CULTIVATION AND INTEGRATED CONTROL APPROACHES

Dan Luo, XianEn Li*

Institute of Medicinal Plant Development, Chinese Academy of Medical Sciences & Peking Union Medical College, Beijing 100193, China.

Corresponding Author: XianEn Li, Email: xeli@implad.ac.cn

Abstract: American ginseng (*Panax quinquefolius* L.), a high-value medicinal crop, faces persistent threats from soil-borne diseases (e.g., root rot, rusty root). Conventional chemical controls risk disrupting soil microecology and inducing pathogen resistance. This study advocates ecological regulation-centered strategies, emphasizing intercropping (e.g., maize, onion) and soil amendments (e.g., biochar) to reshape rhizosphere microbiomes and suppress pathogens. Maize secretes phenolic acids to reduce *Fusarium* abundance, while biochar enriches beneficial microbes (e.g., *Burkholderia*) and enhances soil health and ginsenoside content. These approaches synergize disease control, carbon sequestration, and economic benefits but require avoiding crop competition and improper biochar application. Future research should prioritize the application of intercropping and biochar in American ginseng cultivation, investigate the synergistic disease resistance mechanisms between plants and microbes, and drive the sustainable transition of the American ginseng industry.

Keywords: American ginseng; Intercropping; Biochar; Rhizosphere microbiome; Sustainable agriculture

1 INTRODUCTION

American ginseng (*P. quinquefolius* L.), also known as Huaqishen or Western ginseng, is the dried root of a perennial plant belonging to the Araliaceae family, *Panax* genus. Native to North America, it was introduced to China in the 1980s and is now widely cultivated in northern and northeastern regions. With a cool nature and sweet-bitter taste, it is traditionally used to replenish qi, nourish yin, and clear heat, particularly for treating fatigue, thirst, and respiratory disorders. Modern research reveals that its bioactive compounds (e.g., saponins, polysaccharides, amino acids) exhibit antioxidant [1], anti-fatigue [2,3], hypoglycemic [4], and immunomodulatory effects [5]. Despite its high market demand, American ginseng faces severe disease challenges during cultivation, sharing susceptibility to pathogens with related species (e.g., *Panax ginseng*, *Panax notoginseng*). Soil-borne diseases such as root rot (33%-41% incidence in Shandong Wendeng, 2016-2019) [6] and anthracnose (>20% yield loss in Jilin Fusong, 2021) [7] critically threaten yield and quality, underscoring the urgency of disease management for sustainable production.

2 COMMON DISEASES IN THE CULTIVATION OF AMERICAN GINSENG

American ginseng (*Panax quinquefolius*) cultivation is threatened by two categories of infectious diseases: soil-borne diseases and airborne diseases. Soil-borne pathogens (e.g., *Fusarium* spp., *Cylindrocarpon* spp.) invade root systems through contaminated soil, causing rot, wilting, and plant death. These pathogens exhibit dual ecological strategies—parasitic adaptation and saprophytic survival—with their virulence modulated by soil properties, organic matter content, and microbial community dynamics [8]. Airborne diseases, transmitted via wind or rain splash, target aerial plant parts (e.g., *Alternaria panax*-induced leaf spots, *Botrytis cinerea*-mediated gray mold), impairing photosynthesis and growth. Notably, soil-borne diseases dominate the threat profile in American ginseng cultivation (Table 1). For instance, root rot (caused by *Ilyonectria mors-panacis* and *Fusarium* spp.) exhibits a 33%-41% incidence in Shandong Province [6], while anthracnose (*Colletotrichum panacicola*) caused > 20% yield loss in Jilin Province [7]. Integrated management of both disease types is critical for sustainable production.

Table 1 Common Diseases of American Ginseng Corresponding Pathogenic Fungi and Disease Occurrence Periods

Disease	Pathogen(s)	Symptoms	Occurrence Period
Root Rot	<i>Ilyonectria mors-panacis</i> [9], <i>Fusarium oxysporum</i> , <i>Fusarium redolens</i> , <i>Fusarium solani</i> [10]	Root decay, chlorosis and yellowing of leaves, wilting of aerial parts	Year-round occurrence, peaks in April-June and September-October; thrives in high temperature and humidity
Fusarium Wilt	<i>F. oxysporum</i> [11]	Leaf yellowing, wilting, and root rot	Predominantly in June-August under high-temperature conditions

Sclerotinia Rot	<i>Sclerotinia sclerotiorum</i> [12]	Root and stem rot with formation of rodent feces-shaped sclerotia, leading to plant death	Severe in spring and autumn under moderate temperatures and high humidity
Rusty Root	<i>Cylindrocarpon destructans</i> [13], <i>C. panicola</i> , <i>I. mors-panacis</i> , <i>I. robusta</i> , <i>I. vredehoekensis</i> , and <i>I. communis</i> [14]	Rusty brown lesions on roots, stems, and buds; tissue disintegration and epidermal rupture	Prevalent during late spring to summer in warm and humid environments
Phytophthora Blight	<i>Phytophthora cactorum</i> [11]	Leaf and root rot, plant wilting, and mortality in severe cases	Frequent in early spring
Anthraxnose	<i>Colletotrichum panacicola</i>	Necrotic lesions on leaves, stems, and fruits with black conidial pustules in later stages	Common during spring-summer and summer-autumn transitions under hot and rainy conditions
Damping-off	<i>Pythium debaryanum</i>	Water-soaked lesions at the base of seedlings, leading to lodging and death	Primarily occurs in April-June during seedling stage
Black Spot	<i>Alternaria panax</i> [9,15]	Circular dark brown leaf spots, desiccation of expanded lesions, stem lodging, and growth retardation	Year-round occurrence, exacerbated in humid and rainy seasons
Gray Mold	<i>Botrytis cinerea</i>	Tissue maceration, plant collapse, and gray-green sporulation on infected fruits	Initial onset in April-May, incidence increases with rising temperatures

3 PREVENTION AND CONTROL OF SOIL-BORNE DISEASES

The prevention and control of soil-borne diseases in American ginseng (*Panax quinquefolius*) require a synergistic approach targeting pathogen invasion pathways, environmental factors, and host resistance, establishing an ecology-centered integrated strategy. Optimizing planting patterns (e.g., rational intercropping and crop rotation), improving soil physicochemical properties, and breeding disease-resistant cultivars can effectively disrupt pathogen transmission chains and reduce disease risks.

3.1 Intercropping

As a representative agroecological practice, intercropping suppresses soil-borne pathogen proliferation and enhances soil microenvironments through allelopathic interactions and rhizosphere microbial modulation. For instance, maize/onion intercropping systems inhibit *Fusarium* activity via root exudates such as phenolic acids in maize [16] and sulfur compounds in onions [17], while maize/pepper intercropping reduces viral disease incidence by 56.9% [18]. Post-cucumber monoculture soils rotated with onions exhibit significant declines in *Fusarium* abundance [19]. Deep tillage combined with intercropping accelerates organic matter decomposition, promoting beneficial microbial colonization (e.g., Actinobacteria) and reshaping rhizosphere community structures [20]. Companion plant selection should prioritize growth promotion or pathogen suppression over yield objectives [21].

Proper intercropping enhances nutrient uptake and secondary metabolite synthesis: *P. notoginseng*/taro intercropping increases leaf area and seedling vigor by 19.67% and 28.13%, respectively, while elevating soil available phosphorus and potassium [22]; maize/*Cynanchum auriculatum* intercropping reduces downy mildew and brown spot incidence by 14.2–15.6% and enhances flavonoid/polyphenol accumulation [23]. Maize intercropped with lilies or *Atractylodes macrocephala* modulates rhizosphere microbiomes (e.g., suppressing *Fusarium* while enriching *Streptomyces* and *Rhizobia* [24, 25]), improving stress resistance and medicinal compound biosynthesis. However, improper combinations may yield negative effects, such as inhibited biomass accumulation in *Angelica sinensis*/oat systems [26] or reduced microbial diversity in grape/crepis intercropping. Thus, intercropping design must avoid same-family rotations and prioritize plants with validated antimicrobial activity. For American ginseng, ryegrass (*Secale cereale* L) or red clover (*Trifolium pratense* L) intercropping significantly enriches beneficial rhizobacteria (e.g., Acidobacteria, Chloroflexi), stimulates ginsenosidesynthesis, and suppresses pathogens [27], providing empirical support for ecological disease management.

3.2 Breed Disease-Resistant Varieties

Breeding disease-resistant cultivars serves as the genetic foundation for pathogen control, providing intrinsic resistance. Genetic modification or screening of American ginseng enables the development of cultivars adapted to specific environmental conditions to enhance overall stress tolerance. Systematic breeding efforts have yielded successful examples, such as the *Salvia miltiorrhiza* cultivar ‘Dankang 1,’ which exhibits high levels of bioactive compounds and resistance to root rot and root-knot nematode disease [28], and the hybrid cultivar ‘Longliangyou 1019’ with a comprehensive blast resistance index of 2.7 [29]. However, prolonged development cycles, genetic uniformity risks, and pathogen-specific efficacy limit the practical application of such cultivars, necessitating multi-year trials. Currently, no widely adopted disease-resistant cultivars of American ginseng are commercially available.

3.3 Scientific Fertilization

Scientific fertilization effectively mitigates disease occurrence by optimizing organic or composite microbial fertilizer applications to restructure soil microbial communities and suppress pathogen proliferation. Studies have demonstrated that rational application of organic compound fertilizers and biogas slurry significantly enhances *P. ginseng* growth and resistance to rust rot disease [30]. Field trials confirmed that bio-organic fertilizer application in continuous *P. ginseng* cropping soils improves rhizosphere microenvironments, elevates microbial diversity, adjusts soil pH, and increases organic matter content, boosting yield by 10%–30%. Wang et al. [8] reported that high-dose calcium oxide (4.5 g/kg) reduces root rot incidence caused by *F. solani* and *I. mors-panacis* in American ginseng, whereas 0.5 g/kg exacerbates symptoms. However, fertilization strategies face challenges including high costs, delayed efficacy requiring long-term commitment, and technical precision. Improper practices may aggravate diseases, as exemplified by nitrogen-sensitive American ginseng trials showing excessive nitrogen fertilization induces soil acidification, facilitating pathogen invasion and intensifying soil-borne epidemics [31].

3.4 Soil Disinfection

Soil disinfection serves as a critical measure to block pathogen reinfestation, offering direct and efficient pathogen eradication with rapid short-term efficacy. Common methods include physical approaches (solarization, steam sterilization, hot water irrigation), chemical treatments (fumigants, drenching agents), biological strategies (microbial inoculants, plant-derived disinfectants), and emerging technologies (flame disinfection, ozone treatment, electro-chemical techniques). Chemical disinfection remains the most prevalent: Li et al. [32] demonstrated that 98% dazomet granule application in 5-year-old *P. ginseng* soils significantly reduced pathogenic fungi (*Fusarium*, *Cylindrocarpon*) via dilution plate assays, while Han et al. [33] reported chloropicrin fumigation (25–35 kg/667 m²) suppressed *P. ginseng* rust rot by 54.78–70.07%. However, prolonged use of chemical agents (e.g., carbendazim, fenaminosulf) risks microbial diversity loss and drug resistance development [34]. In contrast, reductive soil disinfestation (RSD) exhibits dual functionality—inactivating pathogens while reshaping soil microecology to favor antagonistic microbial colonization [35]. Notably, chemical residues (e.g., formaldehyde) may persist, impairing subsequent crop growth and environmental safety, and excessive application disrupts beneficial microbial equilibria, exacerbating pathogen resilience.

3.5 Soil Improvement

Soil amendments establish trinity ecological regulation mechanisms by modulating soil physical structure, chemical properties, and microbial community functions, thereby suppressing soil-borne pathogens and enhancing crop resistance. Common amendments include organic compost, biochar, humic acid, lime, and water-retaining agents, with biochar—a porous carbonaceous material derived from pyrolyzed agricultural residues (e.g., straw, wood chips)—emerging as a research focus due to its high surface area and pore structure. These characteristics improve soil water/nutrient retention, adsorb pathogen-derived toxins and salts via surface functional groups, and provide microhabitats for antagonistic microbes (e.g., *Burkholderia* spp.) and arbuscular mycorrhizal fungi (*Glomeromycota*), inhibiting pathogens like *Fusarium* spp. and *Phytophthora* spp. Biochar enhances systemic disease resistance by regulating soil pH, releasing bioactive organic compounds, and activating soil enzymes (e.g., urease, phosphatase). For instance, tomato fields amended with biochar exhibited 61–78% control efficiency against *Ralstonia solanacearum* [35], while long-term application promotes soil aggregate formation and microbial-driven carbon/nutrient cycling [36]. Biochar enhances plant development and suppresses soil-borne diseases by improving soil nutrient conversion efficiency and enzymatic activity. In field trials comparing three biochar types (manure-derived (PB), wood-derived (WB), and corn stover-derived (MB)) with traditional compost (MC) on continuous *P. ginseng* cropping, MB and WB significantly increased survival rates (21% and 14%, respectively) and root quality (56% improvement with MB), while PB only enhanced root biomass. Biochar reduced total rhizosphere phenolic acids (35–56% reduction) and modulated microbial communities: enriching beneficial taxa like arbuscular mycorrhizal fungi (*Glomeromycota*) while suppressing pathogens (e.g., *Fusarium* spp.). MB notably increased total fungal and bacterial abundance (200% and 38%, respectively) and amplified fungal network complexity. These results demonstrate that corn stover biochar suppresses soil-borne diseases primarily by reconstructing rhizosphere microbial interaction networks and enhancing plant immunity rather than solely improving soil fertility [37]. MB and WB also outperformed MC in soil health restoration, increasing soil fertility by 39% and 23%, root biomass by 27% and 25%, and root quality by 18% and 6% after two-year application. Pathogenic fungi (e.g., *Fusarium*) declined by 19–35%, while beneficial bacteria (e.g., *Burkholderia*) and mycorrhizal fungi proliferated, with MB elevating total fungal abundance by 384% and network complexity. Biochar synergistically improved ginseng quality (e.g., ginsenosides) and soil ecological functions through microbial optimization and pathogen suppression [38]. However, sustained efficacy requires long-term application with dosage adjustments tailored to soil conditions to mitigate potential risks.

4 CONCLUSION AND PROSPECT

American ginseng, a high-value medicinal crop, faces persistent threats from soil-borne diseases such as root rot and rust rot, which severely compromise yield and quality through soil-transmitted pathogens. This review systematically outlines the etiological characteristics, epidemiological patterns, and integrated management strategies for major soil-borne diseases in American ginseng cultivation, with emphasis on the potential of intercropping systems and soil amendments. While conventional chemical control offers short-term efficacy, it risks destabilizing soil microbiomes and inducing pathogen resistance. In contrast, ecology-driven approaches—including optimized intercropping (e.g., maize/onion systems) and biochar application—synergistically suppress pathogen proliferation and enhance soil health by reshaping rhizosphere microbial communities. For instance, maize intercropping reduces *Fusarium* abundance through phenolic acid exudation, whereas biochar adsorbs toxins and enriches beneficial bacteria, significantly lowering disease incidence while boosting ginsenoside content and soil carbon sequestration. These eco-friendly strategies reduce chemical inputs and demonstrate dual ecological-economic benefits.

Current disease management should transition toward an "ecology-centered, multi-technology integration" framework. Interventions like intercropping and soil amendments fundamentally reinforce plant-microbe-soil interactions to restore agroecosystem self-regulation. Although more sustainable than chemical reliance, their efficacy depends on regional conditions, crop combinations, and application techniques. For example, intercropping species must avoid intra-family competition, and biochar feedstock/pyrolysis temperatures require soil-specific optimization to prevent adverse effects. Further research is needed to refine their implementation in American ginseng systems. By integrating technological innovation with ecological principles, this approach can drive the industry toward green, high-quality transformation.

COMPETING INTERESTS

The authors have no relevant financial or non-financial interests to disclose.

REFERENCES

- [1] Kitts D D, Wijewickreme A N, Hu C. Antioxidant properties of a north American ginseng extract. *Molecular and Cellular Biochemistry*, 2000, 203(1-2): 1-10. DOI: 10.1023/A:1007078414639.
- [2] Lin M, Hu S, Zeng Q, et al. Screening anti-fatigue components of American ginseng saponin by analyzing spectrum-effect relationship coupled with UPLC-Q-TOF-MS. *Asian Biomedicine*, 2023, 17(4): 163-172. DOI: 10.2478/abm-2023-0057.
- [3] Qi B, Liu L, Zhang H, et al. Anti-fatigue effects of proteins isolated from *Panax quinquefolium*. *Journal of Ethnopharmacology*, 2014, 153(2): 430-434. DOI: 10.1023/A:1007078414639.
- [4] Xie J T, Mehendale S R, Wang A, et al. American ginseng leaf: ginsenoside analysis and hypoglycemic activity. *Pharmacological Research*, 2004, 49(2): 113-117. DOI: 10.1016/j.phrs.2003.07.015.
- [5] Lemmon H R, Sham J, Chau L A, et al. High molecular weight polysaccharides are key immunomodulators in North American ginseng extracts: characterization of the ginseng genetic signature in primary human immune cells. *Journal of Ethnopharmacology*, 2012, 142(1): 1-13. DOI: 10.1016/j.jep.2012.04.004.
- [6] Guan Y M, Zhang L L, Ma Y Y, et al. First Report of Anthracnose of American Ginseng caused by *Colletotrichum sojae* in Northeast China. *The American Phytopathological Society*, 2021. DOI: 10.1094/PDIS-11-20-2440-PDN.
- [7] Lianju Wu, Yiming Guan, Shifeng Pang, et al. Research Progress on Biological Control of Soil-borne Diseases in Ginseng and American Ginseng by Anti-microorganism. *Journal of Anhui Agricultural Sciences*, 2010, 38(28): 15630-15631. DOI: 10.3969/j.issn.0517-6611.2010.28.072.
- [8] Wang Yi. Effect and preliminary mechanism of exogenous calcium on root rot, gray mold and black spot of American ginseng. *Peking Union Medical college*, 2023. DOI: 10.27648/d.cnki.gzxhu.2023.000774.
- [9] Goodwin PH, Zaro G. Appearance and persistence of activity in soil extracts increasing root rot of American Ginseng (*Panax quinquefolius*) by *Ilyonectria mors-panacis*. *Soil Systems*. 2024; 8(4): 133. DOI: 10.3390/soilsystems8040133.
- [10] Bi Y, Zhang X, Jiao X, et al. The relationship between shifts in the rhizosphere microbial community and root rot disease in a continuous cropping American ginseng system. *Frontiers in Microbiology*, 2023, 14. DOI: 10.3389/fmicb.2023.1097742.
- [11] Jun Wang, Shi Feng, Baohui Lu, et al. *Fusarium oxysporum* f. sp. ginseng, a new forma specialis causing *Fusarium* root rot of *Panax ginseng*. *Phytopathologia Mediterranea*, 2022, 61(3): 417-429. DOI: 10.36253/phyto-13723.
- [12] He Guixiang, Miao Xinyue, Zhan Yu, et al. Screening and identification of three strains of *Bacillus* and their biocontrol effects on ginseng rust rot disease. *Journal of Jilin Agricultural University*, 2024(1): 1-12. DOI: 10.13327/j.jjlau.2024.20388.
- [13] Shao Huihui, Zhang Ximei, Liu Ziqi, et al. Biological characteristics and fungicide sensitivity of four *Ilyonectria* species causing root rot on American ginseng. *Acta Phytopathologica Sinica*, 2022, 52(02): 215-222. DOI: 10.13926/j.cnki.apps.000746.
- [14] Ji Li. Study on soil microbial mechanisms and biocontrol applications in the outbreak of diseases in American ginseng. *University of Chinese Academy of Sciences (Northeast Institute of Geography and Agroecology, Chinese Academy of Sciences)*, 2020. DOI: 10.27536/d.cnki.gccdy.2023.000018.

- [15] Wang Yun. Identification and mechanism of antifungal substances in maize root exudates against *Fusarium* spp.. Anhui Agricultural University, 2023. DOI: 10.26919/d.cnki.gannu.2023.000401.
- [16] Guo Jianing, Li Nannan, Li Kun. Research progress in alleviating continuous cropping obstacles by *Allium* L.Plants. Journal of Henan Agricultural Sciences, 2024, 53(08): 11-20. DOI: 10.15933/j.cnki.1004-3268.2024.08.002.
- [17] Zhai Xiaowei, Zhao Chunying. The influence of different fertilization levels and methods on the yield and benefit of strip intercropping of soybeans and corn. Agriculture of Henan, 2025, (09): 66-67. DOI: 10.15904/j.cnki.hnny.2025.09.038.
- [18] Hussein M Y, Samad N A. Intercropping chilli with maize or brinjal to suppress populations of *Aphis gossypii* Glov. and transmission of chilli viruses. Pans Pest Articles & News Summaries, 1993, 39(2): 216-222. DOI:10.1080/09670879309371794..
- [19] Nishioka T, Marian M, Kobayashi I, et al. Microbial basis of *Fusarium* wilt suppression by *Allium* cultivation. Scientific Reports, 2019, 9(1). DOI:10.1038/s41598-018-37559-7.
- [20] Wang Lei, Lu Baoli, Liu Ruiwei, et al. Breeding and efficient cultivation techniques of the new variety of *Salvia miltiorrhiza*, Dan Kang No.1 . Bulletin of Agricultural Science and Technology, 2024(5): 196-198+201.
- [21] Zhou X, Zhang J, Khashi U R M, et al. Interspecific plant interaction via root exudates structures the disease suppressiveness of rhizosphere microbiomes. Molecular Plant, 2023, 16(5): 849-864. DOI: 10.1016/j.molp.2023.03.009.
- [22] Wang Jiawei, Wang Hualei, Lin Jie, et al. Effects of intercropping on the growth of *Panax notoginseng* and the nutrients and microorganisms in rhizosphere soil. Special Wild Economic Animal and Plant Research, 2024, 46(05): 24-29. DOI: 10.16720/j.cnki.tcyj.2023.104.
- [23] Shen Mingchen, Chen Lei, Li Chunyang, et al. Effects of intercropping maize and *Cynanchum bungeion* their disease resistance, contents of active components, and yield. Barley and Cereal Sciences, 2021, 38(05): 52-56. DOI: 10.14069/j.cnki.32-1769/s.2021.05.011.
- [24] Zhou L, Wang Y, Xie Z, et al. Effects of lily/maize intercropping on rhizosphere microbial community and yield of *Lilium davidii* var. *unicolor*. Journal of Basic Microbiology, 2018, 58(10): 892-901. DOI: 10.1002/jobm.201800163.
- [25] Peng Z, Guo X, Xiang Z, et al. Maize intercropping enriches plant growth-promoting rhizobacteria and promotes both the growth and volatile oil concentration of *Atractylodes lancea*. Frontiers in Plant Science, 2022, 13: 1029722. DOI: 10.3389/fpls.2022.1029722.
- [26] Zhu Shaokun, Sun Lingjun, Gao Shenghua, et al. Effects of intercropping on growth and rhizosphere environment of replanted grapevines. Sino-Overseas Grapevine & Wine, 2023, (2): 10-15. DOI: 10.13414/j.cnki.zwpp.2023.02.002
- [27] Duan W, Chen X, Ding Y, et al. Intricate microbe-plant-metabolic remodeling mediated by intercropping enhances the quality of *Panax quinquefolius* L. Physiologia Plantarum, 2024, 176(5). DOI: 10.1111/ppl.14499.
- [28] Zeng Yun, Astrology, Guo Jinyou, et al. Breeding, cultivation and seed production techniques of the high-quality, high-yield and disease-resistant hybrid mid-rice variety Longliangyou 1019. Bulletin of Agricultural Science and Technology, 2025(03): 157-160.
- [29] Zhang Dangsheng Analysis of the causes of rust and rot disease of American ginseng in Liuba, Shaanxi Province. Jiangsu Agricultural Sciences, 2012, 40(7): 119-121.
- [30] Guo Chunjing, Guan Zhaohong, Li Yuwen, et al. Research on the impact of bio-organic fertilizers on the soil micro-ecological environment of ginseng continuous cropping fields . Biotechnology, 2004, 14(3): 55-56. DOI: 10.16519/j.cnki.1004-311x.2004.03.030.
- [31] Zhang Y, Ye C, Su Y, et al. Soil acidification caused by excessive application of nitrogen fertilizer aggravates soil-borne diseases: Evidence from literature review and field trials. Agriculture, Ecosystems & Environment, 2022, 340(000): 10. DOI: 10.1016/j.agee.2022.108176.
- [32] Han Runting, Zhang Jinhua, Ren Jinping, et al. Test on control effect of liquid chloropicrin on ginseng rust. Journal of Northeast Agricultural Sciences, 2008, 33(4): 32-33, 42. DOI: 10.16423/j.cnki.1003-8701.2008.04.008.
- [33] Chen Bingwei, Li Yong, Wang Rong, et al. Resistance of ginseng *Botrytis cinerea* isolates to three chemical fungicides in china. Modern Chinese Medicine, 2021, 23(12): 2115-2119. DOI: 10.13313/j.issn.1673-4890.20201218003.
- [34] Liu Liangliang. Study on the effect of strongly reducing soil disinfection in controlling soil-borne diseases and its microbiological mechanism. Nanjing Normal University, 2019. DOI: 10.27245/d.cnki.gnjsu.2019.000394.
- [35] Ji Hui T, Shuang R, Yang G, et al. Wheat straw biochar amendment suppresses tomato bacterial wilt caused by *Ralstonia solanacearum*: Potential effects of rhizosphere organic acids and amino acids. Journal of Integrative Agriculture, 2021, 20(9): 2450-2462. DOI:10.1016/S2095-3119(20)63455-4.
- [36] Zhang C, Zhao X, Liang A, et al. Insight into the soil aggregate-mediated restoration mechanism of degraded black soil via biochar addition: Emphasizing the driving role of core microbial communities and nutrient cycling. Environmental Research, 2023, 228: 115895. DOI: 10.1016/j.envres.2023.115895.
- [37] Liu C, Xia R, Tang M, et al. Improved ginseng production under continuous cropping through soil health reinforcement and rhizosphere microbial manipulation with biochar: a field study of *Panax ginseng* from Northeast China. Horticulture Research, 2023, 9(1): 1957-1972. DOI: 10.1093/hr/uhac108.

- [38] Liu C, Xia R, Tang M, et al. More microbial manipulation and plant defense than soil fertility for biochar in food production: A field experiment of replanted ginseng with different biochars. *Frontiers in Microbiology*, 2022, 13: 1065313. DOI: 10.3389/fmicb.2022.1065313.

ANALYSIS OF THE EFFECT OF ARTIFICIAL INTELLIGENCE-ASSISTED MINIMALLY INVASIVE TREATMENT FOR URINARY CALCULI

LinFeng Li

The First Clinical College, Guangzhou Medical University, Guangzhou 511436, Guangdong, China.
Corresponding Email: 2022111127@stu.gzhmu.edu.cn

Abstract: Urinary calculi, a prevalent urinary system disorder, significantly impairs patients' quality of life and exhibits an escalating incidence. While minimally invasive surgery offers clinical advantages, it is challenged by complications, high costs, and inconsistent standards. This study explores the role of artificial intelligence (AI) in enhancing minimally invasive treatment for urinary calculi, addressing unmet needs in precision and efficacy. Using a systematic analysis, the research examines AI applications across the treatment continuum: preoperatively, AI predicts stone composition, evaluates size/location, and optimizes surgical strategies through data-driven models; intraoperatively, it enhances procedural safety and outcomes via real-time decision support; postoperatively, AI aids risk assessment for recurrence and guides personalized follow-up to reduce complications. Findings reveal that AI integration improves treatment customization and precision by synthesizing multi-dimensional clinical data, yet challenges persist, including model accuracy limitations, standardization gaps, variable physician proficiency, and economic barriers. Innovatively, this study highlights AI's potential to transform holistic management of urinary calculi while identifying critical implementation hurdles. It underscores the need for technological refinement, standardized protocols, clinician training, and cost-containment measures to facilitate widespread adoption. By bridging AI capabilities with clinical practice, this analysis provides a practical framework for advancing minimally invasive therapies, ultimately aiming to enhance patient care through evidence-based, AI-driven solutions.

Keywords: Urinary calculi; Minimally invasive surgery; Artificial intelligence; Assisted treatment

1 INTRODUCTION

Urinary calculi are one of the most common urinary system disorders, not only significantly affecting the quality of life of patients, but also causing a series of complications, including urinary tract obstruction, pain, nausea, vomiting, and sepsis. The common causes are urinary retention, infection, the presence of foreign bodies, dehydration, diet, and inactivity [1]. Therefore, timely and effective treatment of urinary calculi has become an important task in clinical medicine.

Traditional treatments for urinary calculi include drug therapy and non-drug therapy. Non-drug therapy, such as surgical treatment, has obvious advantages over drug treatment. Surgical treatment of urinary calculi has the advantages of higher treatment efficiency, rapid symptom relief, and reduced risk of recurrence when dealing with large and complex calculi. Surgical treatments include pyelotomy or renal sinus lithotomy, partial nephrectomy, and ureterotomy. Each of these methods has its advantages and disadvantages, and the therapeutic effect varies depending on the size and location of the stone and the overall health of the patient. With the continuous advancement of technology, minimally invasive surgery is receiving increasing attention in the treatment of urinary calculi, including extracorporeal shock wave lithotripsy (ESWL), percutaneous nephrolithotripsy (PCNL), and cystoscopic lithotripsy. Replacing open surgery with minimally invasive techniques for treating renal calculi has significantly reduced morbidity and mortality, as well as hospitalization and recovery periods for patients. If extracorporeal shock wave lithotripsy does not require anesthesia and almost no analgesia, it can be treated in the outpatient department, and there are no wounds to heal. Percutaneous endoscopic lithotomy requires only a small puncture site and has few complications with the advent of prophylactic antibiotics [2].

Artificial intelligence (AI), as a cutting-edge technology, deeply simulates human intelligence. Through algorithms and models, machines are endowed with the ability to learn knowledge independently, solve logical problems, and make precise decisions. It is highly effective in many fields such as healthcare, transportation, and finance. Its rapid development has provided new solutions for the diagnosis and treatment of urinary calculi. Through big data analysis and machine learning algorithms, AI can help doctors identify stones more accurately in imaging examinations, assess the nature of stones, and predict postoperative outcomes for patients.

Although minimally invasive techniques have made significant progress in recent years, they have been continuously improved, such as the development of more advanced endoscopes and lithotripsy equipment, which have enhanced the efficiency and safety of stone removal, such as using AI to predict the size, location, and future development of stones. Although minimally invasive surgery is generally minimally invasive, there is still a risk of postoperative complications such as bleeding, infection, and damage to surrounding organs, which can affect the recovery of patients and the promotion of the surgery. The persistence, development, or recurrence of complications such as recurrent urinary tract infection (UTI), urinary retention, stones, hematuria, and urinary incontinence may also indicate the failure of

minimally invasive treatment [3]. Lower stone clearance rate and higher re-treatment rate of shock wave lithotripsy (SWL) when dealing with larger stones. At the same time, minimally invasive surgery may require higher equipment investment and maintenance costs compared to traditional surgery, making it difficult to fully promote economically. There is also a lack of unified clinical application guidelines and standards for what types of stones are suitable for minimally invasive surgery, which may lead to a less reasonable choice of treatment options. There is a lack of research on minimally invasive surgery in the long-term effect evaluation, and more clinical data are needed to support its efficacy and safety.

This study will conduct a systematic analysis of urinary calculi treatment methods based on AI-assisted minimally invasive techniques, aiming to provide references for clinical practice and identify the limitations, directions, and prospects of AI development, and this will provide some assistance and guidance for the clinical treatment of urinary calculi.

2 PREOPERATIVE DIAGNOSTIC ANALYSIS

2.1 Prediction of Stone Composition

Accurate determination of the composition of urinary calculi is of great significance for formulating personalized treatment plans. Traditional stone composition analysis is usually carried out after the stones are removed, and the process is rather cumbersome. AI technology, through in-depth analysis of multi-dimensional data such as patients' clinical data and imaging features, can predict the composition of stones before surgery, including computed tomography (CT) images, endoscopic images, direct images, X-rays, and smartphone micrographs [4]. A variety of AI models can be used, such as artificial neural network (ANN), convolutional neural network (CNN), deep learning models, machine learning, and SVM. It was found that the average accuracy rate of the 35 AI models used in the 14 original studies was 88.2%. Compared with traditional stone composition analysis, AI-assisted stone composition analysis is more accurate and convenient, and different models have their own advantages for different data, all contributing to the precise prediction of stone composition. This indicates that AI can provide clinicians with valuable preoperative information, providing a basis for them to choose more appropriate treatment methods.

2.2 Analysis of Stone Size and Location

Precisely determining the size and location of urinary calculi is crucial for formulating the surgical plan. AI technology has shown high accuracy and efficiency in this regard. In determining stone volume, Yenikekaluva et al. conducted a retrospective study of non-enhanced CT (NCCT) -KUB scan data from 494 patients over 18 years old and used AI-driven UrologiQ software to calculate stone volume [5]. Compared with radiologists' measurements, patients' personal information was removed during data processing, and some of the data were manually split by ITK-SNAP software to calculate volume for cross-validation. The results showed an intra-group correlation coefficient of 0.999 between AI and human validators, and a Dice score of 0.936, indicating high consistency between the two. In addition, the trends of AI and radiologists in evaluating the Hounsfield unit (HU) value of stones were similar, and the correlation between the volume measured by AI and the results calculated by both human validators and radiologists was strong (p values were all less than 0.001). This indicates that AI measurement of kidney stone volume is more accurate, efficient, and consistent than manual calculation by radiologists, which can improve diagnostic accuracy and surgical planning and help promote the standardized application of volume measurement in clinical practice. In the future, it can be combined with advanced imaging equipment to further optimize diagnosis and treatment processes.

2.3 Screening of Treatment Strategies

AI is also very important for the analysis of treatment strategies in the preoperative planning of urinary calculi. With the help of deep learning algorithms, AI can precisely interpret patients' CT, magnetic resonance imaging (MRI), and other imaging data, identify the location, size, shape, and quantity of stones, and analyze the anatomical relationship between stones and surrounding tissues. Alexander et al. analyzed the treatment outcomes of 625 patients with kidney stones, created registers containing more than 50 parameters for each patient, and used them as the basis for training neural network evaluation techniques [6]. To assess the potential of the neural network algorithm in choosing surgical treatments for urinary calculi, the results showed that the technique helped urologists select the best treatment for each patient, thereby minimizing the risk of early postoperative complications.

3 AI-ASSISTED MINIMALLY INVASIVE SURGERY

3.1 Shock Wave Lithotripsy (SWL)

SWL is one of the most widely used stone treatment techniques. With the continuous development of technology and the continuous improvement of equipment, its therapeutic effect and safety have been further enhanced, and its application scope has been expanded, occupying an indispensable position in the comprehensive treatment system for urinary calculi. The assistance of AI is an indispensable part of its development.

Nakamae et al. used a nonlinear support vector machine (SVM) algorithm in their study, using preoperative non-enhanced computed tomography (NCCT) data from 171 patients with ureteral calculi, including three non-automatic measurement factors: patient age, distance from skin to calculi, and thickness of the ureteral wall [7]. AI predicts the outcome of SWL by analyzing these multi-dimensional data, including 12 automatic measurement factors such as stone volume, seven CT value statistical parameters, and four gradient concentration factors, assisting doctors in judging the SWL treatment effect on patients before treatment. After five-fold cross-validation, the average area under the receiver operating characteristic curve (AUC) for the predictive performance of the AI model was 0.742, and the mean sensitivity to the stone-free state (SF) was 0.692 when the specificity was 0.733. Its advantages lie in its robustness to data diversity, its ability to effectively avoid errors caused by manual measurement factors, and its use of multi-factor prediction, which is more systematic than single-factor prediction and applicable in a variety of clinical scenarios, providing a valuable reference for the selection of clinical treatment plans.

In ESWL, precise focusing of stones is the core to improve the effect of lithotripsy. AI technology can automatically adjust the direction and energy of shock wave emission by monitoring the location of the stone and the patient's breathing movement in real time, achieving precise lithotripsy. The U - Net neural network can be used in two - dimensional ultrasound image analysis of ESWL [8]. The algorithm can determine whether kidney stones are in the focused area (FZ), enabling the lithotripsy machine to precisely emit shock waves, increase hit rate, reduce error rate, and make ESWL treatment more accurate and safer.

In terms of efficacy, the median hit rate of the standard ESWL was 55.2% (95% confidence interval 43.2 - 67.3%), which increased to 75.3% under the control of the U - Net algorithm, and the overall error rate decreased by 67.1%. In terms of classification performance indicators, the U - Net algorithm had an accuracy rate of 63.9%, a sensitivity of 56.0%, and a specificity of 74.7%. It performed well in the classification of "stones not in the focus area" and could accurately track stones, outperforming random guessing.

In terms of treatment time and hit counts, the treatment time of ESWL controlled by U - Net was 1.94 times that controlled by the operator, and the hit counts were 23 and 45 per minute, respectively. Due to the algorithm's ability to reduce errors and theoretically to increase the frequency of shock wave emissions, the actual treatment time could be shortened.

The study data were taken from 11 patients treated with ESWL. Two - dimensional ultrasound videos were collected using a video collector, and 5 - minute sequences were randomly selected and labeled. One observer annotated 23,212 frames to determine if the stones were in the FZ, and another generated binary masks of kidneys and stones for 57 images. 11 models (9 trained, 1 validated) were created through patient - cross - validation, and 8 models were tested on 23,212 frames of images from 8 patients to reduce the risk of overfitting. The study was licensed by the regional ethics committee to ensure data compliance, and it also conducted a comprehensive statistical analysis of the data and calculated multiple assessment metrics.

In summary, AI (U - Net neural network) - assisted ESWL improved treatment outcomes. Although there is room for improvement in performance metrics, it made treatment more precise and safer overall.

AI model integrates multiple algorithms and data, extracts 100 radiomics features with the PyRadiomics tool, and extracts 256 autoencoder features with 3D autoencoders [9]. The model was trained using machine learning algorithms such as Support Vector Machine (SVM), Random Forest (RF), XGBoost (XGB), and CatBoost (CB). The data were derived from 317 patients with ureteral calculi collected from October 2023 to March 2024, including basic patient information, CT image data, and the patients were followed up with KUB X-ray examination for 4 weeks after surgery to evaluate the stone clearance. In terms of assisting ESWL, the AI model automatically identified and segmented the regions of ureteral calculi through the analysis of CT images and extracted relevant features to predict the therapeutic effect of ESWL, that is, to determine whether the calculi were cleared or whether the residual fragments were ≤ 2 mm. In terms of performance, the semantic segmentation model achieved an average Dice coefficient of 0.88 ± 0.08 on the external test set. On the internal validation set, the AUROC values of the ESWL classifiers constructed by SVM, RF, XB, and CB were 0.78, 0.84, 0.85, and 0.90, respectively, and on the external test set were 0.68, 0.79, 0.80, and 0.83, respectively, with the CB algorithm performing the best. The advantages of this AI model lie in its innovative integration of advanced imaging analysis techniques, multi-center validation for enhanced robustness and generalization ability of the model, evaluation of multiple machine learning algorithms to determine the optimal algorithm, and enhanced interpretability of model decisions by calculating SHAP values, which can provide reliable decision support for clinical practice. It helps improve treatment outcomes for patients.

3.2 Percutaneous Nephrolithotomy (PCNL)

PCNL is an important surgical method for treating urinary calculi, especially kidney calculi, and plays a key role in the surgical treatment of urinary calculi. Up to now, AI has been used to predict the outcome of PCNL. Aminsharifi et al. included all adult patients who received PCNL at the hospital during the study, recorded preoperative and postoperative variables, and evaluated the perioperative stone-free status by computed tomography [10]. The network was designed and trained with a feedforward backpropagation error adjustment scheme. The preoperative and postoperative data of 200 patients were used as the training set to analyze the influence and relative correlation of preoperative values on postoperative parameters. The trained and validated ANN system was used to predict the postoperative results of 254 adult patients (test set), and the predicted values were compared with the actual results to evaluate the accuracy of the system in predicting each postoperative variable. The test set included 254 patients, 61% of whom were male, with an

average stone load of $6702.86 \pm 381.6 \text{ mm}^3$, an overall stone-free rate of 76.4%, and 21.3% of patients requiring assisted surgery. The accuracy and sensitivity of the ANN system in predicting different postoperative variables ranged from 81.0% to 98.2%. It demonstrated the system's significant role in predicting postoperative outcomes for PCNL.

Anastasiadis et al. also summarized in the article that PCNL was assisted in multiple aspects such as puncture guidance, surgical planning, postoperative outcome prediction, and intraoperative tissue monitoring, which improved the accuracy, safety, and therapeutic effect of the surgery [11]. Robot-assisted fluoroscopic-guided puncture, for example, not only has a high success rate but also shortens the puncture time and the total duration of the operation. A method of guided PCNL puncture based on AI and optical coherence tomography (OCT) can be developed. By constructing and training the DL algorithm, the OCT patterns of the renal cortex, medulla, and calyces can be identified with high precision, effectively guiding the puncture needle and identifying the type of anterior tissue.

Gauhar et al. explored the application of AI and robotics in PCNL [12]. In terms of algorithms and data, the specific algorithms used by the AI models were not specified in the paper, and the data came from 12 in vivo studies covering patients with different types of nephrolithiasis and related surgical information. In terms of assisting surgery, the 3D reconstruction model uses CT image data for processing to assist in determining the puncture point and designing the puncture path. Robot-assisted systems such as ANT-X use AI to detect marker balls to calculate puncture trajectories. In terms of effectiveness, multiple studies have shown that the use of related technologies can reduce operation time, decrease the number of punctures, increase the success rate of the first puncture and stone clearance, and reduce intraoperative blood loss and complication rates. The advantage lies in enhancing doctors' spatial understanding of the anatomy of the kidneys and improving the precision of preoperative planning and intraoperative operations. 3D printing, virtual, and mixed reality technologies provide doctors with a better training experience and help shorten the learning curve. Robot-assisted techniques can improve puncture accuracy, reduce radiation exposure, and have the potential for remote operation, promising better outcomes for complex and challenging surgeries.

3.3 Ureteroscopic Lithotripsy (URL) And Ureteroscopic Lithotripsy (URS)

URL and URS are essential techniques in the field of endovascular urology. They represent the trend of urological surgery towards minimally invasive and precision, providing doctors with an efficient and safe way to treat stones, as well as patients with better treatment outcomes and less trauma, and promoting the advancement of urological stone treatment techniques. The addition of AI has further promoted this development.

Nedbal et al. employed 16 machine learning algorithms in their study, including logistic regression, quadratic discriminant analysis, and extreme gradient boosting (XGBoost) [13]. The data used were from a cohort of adult patients who underwent ureteroscopic laser lithotripsy (URSL) for urolithiasis between March 2012 and December 2018, covering eight core parameters including preoperative age, gender, and urine culture results. AI-assisted URSL is reflected in the automatic prediction of postoperative outcomes based on preoperative features, such as the use of ureteral access sheath (UAS), postoperative stent insertion, complications, and stone-free status (SFS), through trained models. In predicting SFS, the integrated ML model achieved an accuracy of 93% and a precision of 87%. It also had high accuracy in predicting complications. Its advantage lies in being able to handle complex and multi-faceted datasets, generating personalized risk assessments by integrating patients' demographic and preoperative characteristics, helping clinicians identify high-risk patients, develop preoperative plans, adjust postoperative care programs, and optimize resource allocation, assisting doctors in making wiser decisions and improving patient safety.

In flexible ureteroscopic lithotripsy (fURL) for ureteral calculi, the AI model combined the LASSO algorithm and the deep neural network (DNN) model [14]. The model was constructed based on preoperative non-enhanced CT scan data and related clinical information (such as age, gender and BMI) of 847 patients with unilateral, isolated proximal ureteral calculi, and externally validated with data from 40 patients. Data dimension reduction and feature selection were performed using the LASSO algorithm to determine 26 key predictors and construct radiomics models. The DNN model, based on the extracted features, further improves the prediction accuracy by learning complex relationships through multiple layers of nonlinear activation functions. AI-assisted surgery is reflected in predicting the risk of sepsis after fURL or PCNL before surgery, helping doctors identify high-risk patients and take preventive and monitoring measures in advance. In terms of effectiveness, the LASSO model had an AUC of 0.881 (internal validation) and 0.783 (external validation) for predicting sepsis, while the DNN model had an AUC of 0.920 for internal validation and 0.874 for external validation, demonstrating good predictive capabilities. The advantage of this AI model lies in its ability to make more effective use of information on the characteristics of stones in vivo compared to traditional clinical variables and laboratory tests. DNN models are more predictive than LASSO models and can capture higher-order interactions among variables. It can also facilitate the stratification of sepsis risk in patients and provide strong support for clinical decision-making, though the study has limitations, such as a limited sample size and not including some clinical factors. AI also plays a key role in stone detection and localization. Through deep learning training on medical imaging data such as CT, MRI, and ultrasound of a large number of patients, AI models such as convolutional neural networks (CNNs) can precisely identify the location, size, shape, and quantity of stones. When processing CT images, the AI algorithm can quickly analyze the features of pixels in the images, distinguish the stones from the surrounding tissues, automatically mark the location of the stones, greatly improve the efficiency and accuracy of detection, reduce the risk of human error, avoid missed diagnosis of stones due to subjective factors of doctors, and help doctors develop a more complete URS surgical plan before surgery.

During URS surgery, the intelligent robot-assisted system uses AI to achieve precise control of instrument operation. The robotic arm was able to move and position the surgical instrument precisely based on the stone location and surrounding tissue information generated by AI analysis of the images. Compared with traditional manual operation, robotic assistance can control operation accuracy to the millimeter level, reduce damage to surrounding tissues such as the ureteral wall, and lower the risk of complications such as intraoperative bleeding and ureteral perforation, especially when dealing with stones in complex locations.

In addition, another major contribution of AI in URS is the realization of real-time assessment and decision support for surgical risks. By integrating multiple sources of information, such as real-time vital sign data of patients, intraoperative images, and instrument operation data, the AI model can dynamically assess surgical risks. In the event of risks such as excessive pressure in the renal pelvis and increased bleeding tendency, the system quickly analyzes and provides response suggestions for the doctor, such as adjusting the flow rate of perfusion fluid, suspending the operation for hemostasis treatment, helping the doctor to optimize the operation plan in time during the operation, ensuring the smooth progress of the operation and improving the overall safety and quality of the operation.

In URS and URL, AI plays a key role with multiple algorithms. When predicting the risk of sepsis, the LASSO algorithm selects key features and works with the DNN model to estimate the risk of sepsis after FURL or PCNL based on preoperative non-enhanced CT and clinical information. The DNN model can capture complex variable relationships to support clinical decisions. In terms of medical imaging, CNNs deeply learn CT, MRI, and ultrasound images to accurately identify the location and size of stones, avoid missed diagnoses, and assist in planning URS surgical pathways. During the operation, AI integrates the patient's vital signs, intraoperative images, and instrument operation data to monitor risks in real time and provide response strategies in case of excessive stress or bleeding risks. At the same time, AI controls the intelligent robot-assisted system to precisely operate the robotic arm, reduce tissue damage, and improve the safety and quality of the surgery.

4 THE ROLE OF AI IN PREVENTION

AI plays a crucial role in the prevention of urinary calculi and helps doctors develop personalized prevention plans for people at high risk, such as reminding them to increase water intake, adjust their diet, and increase physical activity. AI can monitor health data in real time through smart devices or health management platforms, issue risk warnings promptly, and encourage people to actively adjust their lifestyles, thereby effectively reducing the incidence of urinary tract stones and improving public health.

For instance, the AI model developed by Sánchez et al., which uses a variety of machine learning algorithms and has a wide range of data sources that have been strictly screened, has played a key role in predicting the risk of urinary calculi and achieved relatively significant results [15]. They designed questionnaires covering various aspects such as demographics, nutrition, exercise, and medical history, and after pre-trials, they distributed them widely through social media, ultimately collecting 976 valid questionnaires to provide data for the model construction. A variety of classifiers, including logistic regression, decision tree, random forest, and extreme random tree, were used to build the model. Python was programmed in the local computing environment to detect complex patterns that distinguish kidney stone patients from non-patients through pattern recognition and classification, and the classification accuracy was verified based on independent datasets. Statistical methods were used to calculate odds ratios, confidence intervals, and P-values to improve the interpretability of the model, and key variables such as gender, physical activity, and thirst level were selected to refine the model.

The role of AI is mainly to predict the risk of urinary calculi, helping patients and doctors understand the likelihood of getting the disease in advance and then take targeted preventive measures. The AI Model achieved an accuracy rate of 88% in predicting the risk of urinary calculi, demonstrating good discrimination ability, effectively identifying the risk of illness, providing a basis for personalized medical intervention, and promoting the development of precision medicine.

5 THE ROLE OF AI IN POSTOPERATIVE MANAGEMENT AND FOLLOW-UP

In the postoperative management and follow-up stage of urinary calculi surgery, AI is demonstrating unique and crucial value. In terms of complication prediction, AI can integrate multi-source data such as surgical details, postoperative vital signs, and test indicators of patients to build precise prediction models. By learning from a large amount of case data, AI can keenly capture the subtle features associated with complications and detect potential risks in advance. In terms of postoperative assessment and rehabilitation guidance, Hameed et al. mentioned that AI can assess postoperative patients and predict the risk of stone residue and recurrence [16]. By analyzing postoperative images and clinical data, it can be determined whether the stones have been completely removed. Combining the patient's lifestyle and genetic factors, doctors can predict the possibility of stone recurrence, develop personalized rehabilitation plans, and preventive measures for the patient to improve the patient's quality of life and reduce the recurrence rate. In follow-up management, AI uses natural language processing technology to efficiently analyze patient feedback, accurately identify potential problems, and promptly notify doctors to handle them. Through in-depth mining of patients' historical data, AI can predict the risk of stone recurrence and provide targeted preventive measures for patients, such as adjusting lifestyle and regular follow-up suggestions. The use of AI-assisted follow-up management can significantly increase the

early detection rate of stone recurrence, improve patient prognosis, enhance patient satisfaction with follow-up, and optimize the overall quality of medical services.

6 DISCUSSION AND PROSPECTS ON AI-ASSISTED MINIMALLY INVASIVE SURGERY FOR URINARY CALCULI

AI-assisted minimally invasive surgery for urinary calculi shows significant advantages in many aspects. In preoperative diagnosis, AI can precisely predict the composition of stones, which is more convenient and accurate than traditional methods, providing a key basis for personalized treatment. When assessing the size and location of stones, AI measurements are more precise and efficient than manual ones, improving diagnostic accuracy and surgical planning. In terms of analyzing treatment strategies, AI uses deep learning to interpret images to help doctors choose the best options and reduce the risk of postoperative complications.

During the procedure, AI plays a significant role in various minimally invasive surgical approaches. In SWL, AI can predict treatment outcomes, precisely focus on stones, and improve the effectiveness and safety of lithotripsy. In PCNL, AI can predict postoperative outcomes, assist in puncture guidance and surgical planning, and improve surgical accuracy and safety. In URL and URS, AI can not only predict postoperative conditions and assess the risk of sepsis, but also precisely detect and locate stones, control robot-assisted operations, and assess surgical risks in real time, improving surgical quality in all aspects. In addition, AI performs well in prevention, postoperative management, and follow-up, predicting stone risk, developing personalized prevention plans, predicting complications and stone recurrence, and optimizing medical services. The commonly used models for AI-assisted minimally invasive surgery in the treatment of urinary tract stones are as follows (Figure 1).

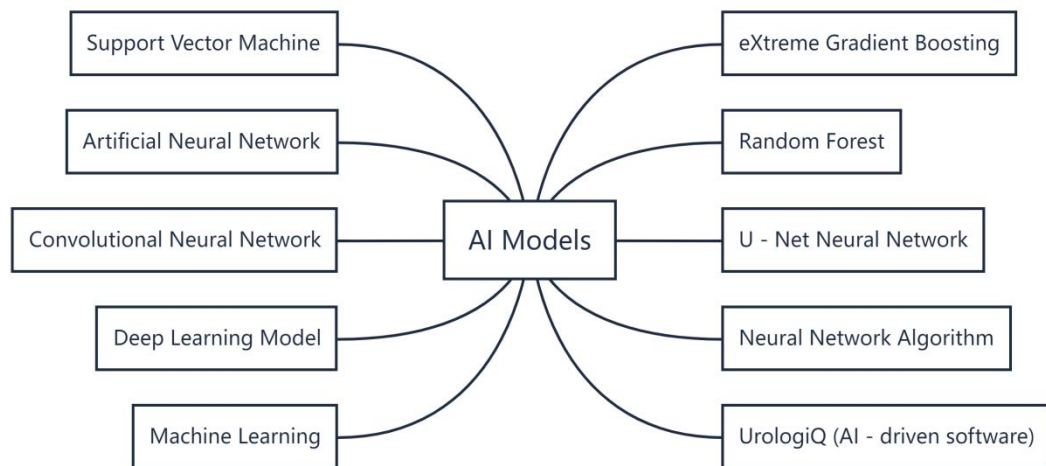


Figure 1 AI Models

However, AI-assisted minimally invasive surgery for urinary calculi also faces many challenges and shortcomings. Technically, the accuracy and stability of some AI models still need to be improved, and different algorithms and data processing methods can affect the prediction and diagnosis results. The quality of the data is uneven, and problems such as incomplete data and inaccurate annotations limit the improvement of model performance. In terms of clinical application, the lack of unified standards and norms for the clinical application of AI technology has led to significant differences in the AI systems used by different medical institutions, making it difficult to popularize them. Doctors have varying levels of familiarity and mastery of AI technology, and some doctors are overly dependent on or reluctant to use AI, which affects the effective application of the technology. At the same time, the high cost of AI technology is also an obstacle to its promotion, including research and development, equipment purchases, and maintenance costs, which increase the financial burden on patients.

For the future, AI-assisted minimally invasive surgery for urinary calculi has great potential. In terms of technology development, algorithms should be further optimized and multimodal data integrated to improve the accuracy, stability, and generalization ability of the model. Strengthen data governance and build high-quality medical imaging and clinical databases to provide reliable data for AI training. In terms of clinical application, unified industry standards and norms need to be established as soon as possible to ensure the safety and effectiveness of AI systems. Strengthen the training of doctors to enhance their ability to apply AI technology and promote the deep integration of AI with clinical practice. From the perspective of cost control, we can reduce costs through technological innovation and large-scale application to improve the cost-effectiveness of AI technology. In addition, enhance international cooperation and exchanges to jointly promote the development of AI-assisted minimally invasive surgery for urinary calculi, provide more efficient and safe treatment options for patients worldwide, and enable AI technology to play a greater role in the field of urinary calculi treatment.

7 CONCLUSIONS

To sum up, AI has shown great potential and value in minimally invasive treatment of urinary calculi. From preoperative diagnosis, surgical procedure, prevention to postoperative management and follow-up, AI technology has played a significant role in all aspects, bringing new ideas and methods to the treatment of urinary calculi. By precisely predicting the composition, size, location, and treatment strategy of the stones, AI helps doctors develop more targeted and personalized treatment plans, improving treatment outcomes and reducing the risk of postoperative complications. During the procedure, the application of AI makes minimally invasive surgeries such as shock wave lithotripsy, percutaneous nephrolithotripsy, ureteroscopy lithotripsy, and ureteroscopy lithotripsy more precise and safer. In the prevention stage, AI helps to develop personalized prevention plans for high-risk groups and reduce the risk of urinary calculi. In postoperative management and follow-up, AI can effectively predict complications and the risk of stone recurrence, provide personalized rehabilitation plans and preventive measures for patients, and improve the overall quality of medical services. Although AI-assisted minimally invasive surgery for urinary calculi still faces challenges in terms of technology and clinical application, these problems are expected to be gradually addressed with the continuous development and improvement of the technology. Through measures such as further optimizing algorithms, strengthening data governance, establishing unified industry standards, enhancing doctors' ability to apply AI technology, and reducing costs, AI-assisted minimally invasive surgery for urinary calculi will be more widely applied in clinical practice, bringing better treatment experience and prognosis to patients with urinary calculi worldwide. To drive continuous progress in the field of urinary calculi treatment.

COMPETING INTERESTS

The author has no relevant financial or non-financial interests to disclose.

REFERENCES

- [1] Steggall M J. Urinary tract stones: causes, complications and treatment. *Br J Nurs*, 2001, 10(22): 1452-1456.
- [2] Wickham J E. Treatment of urinary tract stones. *BMJ*, 1993, 307(6916): 1414-1417.
- [3] Te A E, Cho A, Chughtai B I. How I Handle Retreatment of LUTS Following a Failed MIST. *Curr Urol Rep*, 2021, 22(8): 40.
- [4] Altunhan A, Soy Turk S, Guldibi F, et al. Artificial intelligence in urolithiasis: a systematic review of utilization and effectiveness. *World J Urol*, 2024, 42(1): 579.
- [5] Yenikekaluva A, Agrawal M S, Ramanathan J M, et al. Evaluating the effectiveness of AI-powered UrologiQs in accurately measuring kidney stone volume in urolithiasis patients. *Urolithiasis*, 2024, 52(1): 158.
- [6] Alexander I N, Boris A N, Artem V E, et al. The use of intelligent analysis (IA) in determining the tactics of treating patients with nephrolithiasis. *Urologia*, 2023, 90(4): 663-669.
- [7] Nakamae Y, Deguchi R, Nemoto M, et al. AI prediction of extracorporeal shock wave lithotripsy outcomes for ureteral stones by machine learning-based analysis with a variety of stone and patient characteristics. *Urolithiasis*, 2023, 52(1): 9.
- [8] Muller S, Abildsnes H, Østvik A, et al. Can a Dinosaur Think? Implementation of Artificial Intelligence in Extracorporeal Shock Wave Lithotripsy. *Eur Urol Open Sci*, 2021, 27: 33-42.
- [9] Yang H, Wu X, Liu W, et al. CT-based AI model for predicting therapeutic outcomes in ureteral stones after single extracorporeal shock wave lithotripsy through a cohort study. *Int J Surg*, 2024, 110(10): 6601-6609.
- [10] Aminsharifi A, Irani D, Pooyesh S, et al. Artificial Neural Network System to Predict the Postoperative Outcome of Percutaneous Nephrolithotomy. *J Endourol*, 2017, 31(5): 461-467.
- [11] Anastasiadis A, Koudonas A, Langas G, et al. Transforming urinary stone disease management by artificial intelligence-based methods: A comprehensive review. *Asian J Urol*, 2023, 10(3): 258-274.
- [12] Gauhar V, Giulioni C, Gadzhiev N, et al. An Update of In Vivo Application of Artificial Intelligence and Robotics for Percutaneous Nephrolithotripsy: Results from a Systematic Review. *Curr Urol Rep*, 2023, 24(6): 271-280.
- [13] Nedbal C, Adithya S, Naik N, et al. Can Machine Learning Correctly Predict Outcomes of Flexible Ureteroscopy with Laser Lithotripsy for Kidney Stone Disease? Results from a Large Endourology University Centre. *Eur Urol Open Sci*, 2024, 64: 30-37.
- [14] Chen M, Yang J, Lu J, et al. Ureteral calculi lithotripsy for single ureteral calculi: can DNN-assisted model help preoperatively predict risk factors for sepsis? *Eur Radiol*, 2022, 32(12): 8540-8549.
- [15] Sánchez C, Larenas F, Arroyave J S, et al. Artificial Intelligence in Urology: Application of a Machine Learning Model to Predict the Risk of Urolithiasis in a General Population. *J Endourol*, 2024, 38(8): 712-718.
- [16] Hameed B, Shah M, Naik N, et al. The Ascent of Artificial Intelligence in Endourology: A Systematic Review Over the Last 2 Decades. *Curr Urol Rep*, 2021, 22(10): 53.

